Hydrological and hydrodynamic processes and their impact on spatial characteristics of Terminos Lagoon, Mexico

Cover photo: Laguna de Términos, Mexico (NASA earth observatory) [21]

Hydrological and hydrodynamic processes and their impact on spatial characteristics of Terminos Lagoon, Mexico

by

F.J. Dijkstra	4231112	Geo-science and Remote Sensing
M.Q.T. Groenewegen	4274695	Hydraulic Engineering
L.M.A. Jordans	4293703	Hydraulic Engineering
C.E. Mekel	4295544	Water Management
F.G.H. Steijlen	4282337	Geo-Engineering

CIE4061-09 Multidisciplinary Project
Group 265
Project Terminos Lagoon

TUDelft

UNAM
Instituto de Ciencias
del Mar y Limnología

Disclaimer

The following report is written by five students in their pursuit of a Master degree in Civil Engineering or Applied Earth Sciences. The aim of the project is to get hands-on experience in a new and unfamiliar environment, to enhance teamwork capabilities, to work using a multidisciplinary approach and to use the skills accumulated over the years. To this end, a research is conducted with regard to dynamics, processes and characteristics of Terminos Lagoon. Statements made are not fact-checked, nor should the report be considered as a source to base policy on. Thus, while containing scientifically based approaches, any results and findings presented here reflect the current opinion of five students.

Preface

Dear reader,

At this moment you are looking at the report "Hydrological and hydrodynamic processes and their impact on spatial characteristics of Terminos Lagoon, Mexico." It is written by five students from the Delft University of Technology (TU Delft) as part of the curriculum to become Masters in Civil Engineering or Applied Earth Sciences. In this study master programs of 'Geo-Engineering', 'Geoscience and Remote sensing', 'Hydraulic Engineering', and 'Water Management' are involved. The research is performed in Ciudad del Carmen, near Terminos Lagoon, Campeche, Mexico, during September and October 2018.

The research is conducted in conjunction with the Instituto de Ciencias del Mar y Limnología (ICML), part of the Universidad Nacional Autónoma de México (UNAM). The project is done in collaboration with Oswaldo Morales Napoles, main supervisor of the TU Delft and José-Gilberto Cardoso Mohdano, local supervisor of ICML-UNAM. Our thanks go to Gilberto and to the Instituto de Ciencias del Mar y Limnología, which gave us permission to use their data sets, Delft3D-FLOW model and accommodation. Besides Oswaldo Morales Napoles, we would like to thank the TU Delft supervisors, Julia Gebert, Jan van Overeem and Willem Luxemburg for their feedback and help with track related problems. Furthermore, we would like to thank Marc Schleiss for his advise on use of remote-sensed data in the report.

Moreover our thanks go to the students at ICML and 'El Statión', especially to Eduardo Canek Gómez, who gave answer to all our questions and guided us through Mexico. Thanks to Álvarez Guillén Hernán, Gómez Ponce Mario Alejandro, Reda Deara José Andrés for the sample collection and logistic support of the fieldwork campaigns.

Fokke Dijkstra
Maurits Groenewegen
Luuk Jordans
Charlotte Mekel
Florentine Steijlen
Delft, November 2018

Abstract

Terminos Lagoon is the biggest and ecologically most important fluvial-lagoon system of the southern Gulf of Mexico. Rivers, sea and meteorology all influence the lagoon, variable over the year, resulting in a complex situation. To protect this area, it is crucial to know how different hydrological processes, hydrodynamic processes and spatial characteristics influence each other in this context. Using a multidisciplinary approach, this research focused on the question: *What is the influence of hydrological and hydrodynamic processes on spatial characteristics of Terminos Lagoon, now and in the future?* The study has shown that evaporation has a larger part in the water balance during dry season, where during other seasons the water balance is similar to the annual mean. It is found that the western part of Terminos Lagoon shows different characteristics than the eastern part, as river discharge plays a larger role in the western part of the lagoon. Secchi depth, temperature, dissolved oxygen, sediments and salinity are all different here compared to the eastern part of the lagoon. Salinity and river discharge, as well as air and water temperatures, show to be highly correlated. A tidal watershed divides the lagoon in two approximately equal areas, following the mentioned separation of east and west. Residual currents flow along the boundaries of the lagoon from east to west. A circular residual current in the lagoon is observed near the Puerto Real inlet in created temperature and Secchi depth maps. Nortes season shows highest salinity and lowest Secchi depths, where dry season shows lowest salinity. Both inlets are expected to sedimentate and sediments outside the lagoon move westward. Climatological influences are uncertain, though likely effects are increased water temperature, salinity, flushing time and a decrease in residual current. Mentioned effects are likely most noticeable in the eastern part of the lagoon. Further research is necessary to achieve ecological goals in the region.

Contents

List of Figures

List of Tables

1

Introduction

In this chapter, first of all, the background of the project area and the current situation are given. Afterwards the problems are defined. With these problems in mind, the objective of this report is given with its corresponding main and sub-research questions. The scope, describes the boundaries of the project. Finally, the report outline and structure are explained.

1.1. Background

The lagoon is the biggest fluvial-lagoon estuary system of the southern Gulf of Mexico [38]. It is a shallow tropical coastal lagoon connected to the Gulf of Mexico in Yucatan Peninsula. The total surface area of the main basin is 1690 km^2 (appendix A) and the mean depth is 2.6 m (subsection 2.4). The lagoon is mainly influenced by tides, winds, heat fluxes, and freshwater inputs. It is also shaped by tidal inlet morphology.

Terminos Lagoon is a subject of many studies [47], as it is of regional importance in multiple ways. First, the lagoon provides a variety of habitats to different species. Located in a sub-tropical, humid climate and with access to both fresh and salt water through river and sea, Terminos Lagoon hosts a highly varied biodiversity, yielding its protected status since 1994 [47]. It is a Ramsar site, which is a wetland site of international importance given by Ramsar Convention [26]. The wetlands and its mangroves are the biggest in Latin America. The mangroves provide a nursery to migratory birds. Furthermore, it is a frequent host to bottlenose dolphins. Therefore, the lagoon is not only important to regional ecology, but also to ecosystems spanning a wider area. Next, Terminos Lagoon is of economic importance for the fish and shrimp industries [46]. The area is seen as crucial spawning grounds for Campeche Sound, an important fishing habitat in the Gulf of Mexico. The lagoon plays thus a critical role in the food supply and ecological stability of the region. However, there is a great industrial and coastal development in the lagoon and the adjacent areas [47]. The main urban area nearby Terminos Lagoon is Ciudad del Carmen, with over 200.000 inhabitants [1]. The city is economically reliant on the oil and gas exploration in the nearby Gulf of Mexico. This industry is considered crucial to the Mexican economy and one of the main focuses of the new president [7].

1.2. Problem description

As outlined above, Terminos Lagoon has a high environmental value. However, the water properties of the lagoon system are changing. Both environmental, such as climate change, and human loads pose a threat to the balance between wildlife, humans, water quality and water availability [26]. The mangroves, nursing grounds for the local fish and shrimp populations [12], are retreating [59]. Over the years, lower productivity of species has been visible within the lagoon and loss of species would change the ecosystem [9]. A pollution threat to the ecosystem is the oil exploration in the Gulf of Mexico, which can pose a major pollution threat to the lagoon. This was demonstrated with the Ixtoc-1 oil spill in 1979 [58]. Moreover, globally, storms get more intense, temperatures rises, as well as the sea level which are effects of climate change [33]. All of these factors have an influence on the ecology, water quality and morphology of the lagoon. In order to protect the area, now and in the future, the current state of Terminos Lagoon needs to be known.

Research in hydrological and hydrodynamic processes and their influences on water parameters of the lagoon is required to have a proper view of Terminos Lagoon. Hydrological processes relate to the in- and outflows of

the lagoon, which are linked to the flushing time and thereby also with the water quality and water parameters. Hydrodynamic processes like tides, currents and waves, cause differences in water parameters over time and space.

1.3. Objective

To get insight in Terminos Lagoon, investigations and measurement campaigns are performed by the Instituto de Ciencias del Mar y Limnología (ICML), part of the Universidad Nacional Autónoma de México (UNAM). The goal of this multidisciplinary project is to contribute to the research of ICML in the field of hydrological and hydrodynamic processes. Different from previous studies about Terminos Lagoon, here the processes will be coupled with the spatial characteristics of figure 1.1. The research question of the project is formulated as follows:

> *What is the influence of hydrological and hydrodynamic processes on spatial characteristics of Terminos Lagoon, now and in the future?*

In figure 1.1 the research question is visualised and the considered hydrological and hydrodynamic processes are mentioned, as well as the spatial characteristics. Hydrological processes are all processes of the water cycle. Hydrodynamic processes are forces and motions of fluid.
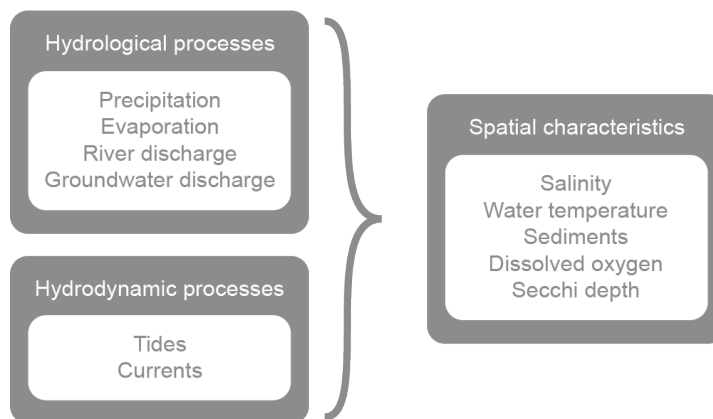
Figure 1.1: Visualization of the report objective.

To answer this research question sub-questions are determined (figure 1.1):

1. What is the water balance and what is the influence of the seasons on it?

2. How are the spatial characteristics of Terminos Lagoon distributed?

3. How can the hydrodynamic processes be recognised in the distribution of the spatial characteristics?

4. How do seasonal variations impact the spatial characteristics of Terminos Lagoon?

5. To what extent are the hydrological processes correlated with the spatial characteristics?

6. What will the consequences of future developments on hydrological processes and spatial characteristics be?

1.4. Scope

The boundaries of the project are described in this section. First, the spatial scope is explained, secondly the time scope of the research is determined.

1.4.1. Area

The Carmen inlet and the Puerto Real inlet are two main tidal inlets (figure 2.1). The Sabuncuy inlet is a shallow and narrow channel. The influence of Sabuncuy inlet is not taken into account in this study, because the net flow is relatively small in comparison with the principal inlets [23].

The Palizada river enters Terminos Lagoon. The two other discharging rivers that are taken into account are the Chumpan river and the Candelaria-Manantel river. The rest is assumed to have a negligible influence on Terminos Lagoon, because of their relatively small discharge [47].

1.4.2. Time
The research of this report focuses on the current state of the lagoon, as it stands in 2018. The most recent available data are used. To determine climate parameters as temperature, humidity, rainfall and wind, a period of 30 years is considered. Predictions of future developments of Terminos Lagoon will be made by determining impact of changes through climate change, morphodynamic changes and increasing oil exploitation.

1.5. Outline
The report continues in the parts: Study area, Data collection, Data analysis and theory, Results and discussion of the spatial distribution, Future developments, Conclusion and Recommendations. Afterwards, the Bibliography and appendices are given. appendices are used to extend the main report. The following chapters include:

- Chapter 2: **Study area**
  A general description of the study area is given, with its topography, seasons, geology and bathymetry.

- Chapter 3: **Data collection**
  The available data collections and the relevance to the project are described.

- Chapter 4:**Data analysis and theory**
  The data are processed in this chapter. A description of the hydrological and hydrodynamic processes is given, as well as the spatial characteristics and the statistical dependence. The data required to come to the results are gathered or edited.

- Chapter 5: **Results and discussion - Spatial distribution**
  In this chapter the results of the spatial distribution of the spatial variables and their seasonal variations are given and discussed.

- Chapter 6: **Results and discussion - Future developments**
  Possible future developments are discussed in this chapter. Correlations are used to predict the future situations.

- Chapter 7: **Conclusion**
  The sub-questions and the main research question are answered.

- Chapter 8: **Recommendations**
  Possibilities for further research are described.

2

Study area

The study area is described in this chapter and divided into the topography, seasons, geology and bathymetry.

Figure 2.1: Overview of the region in and around Terminos Lagoon based on NASA Earth Observatory [21].

2.1. Topography
Terminos Lagoon (18° 26'-18° 48 'N, 91° 14'- 91° 53 'W) is a shallow tropical coastal lagoon connected to the Gulf of Mexico in Yucatan Peninsula in Mexico, see figure 2.1. The total surface area is 1690 km^2 (appendix A) with a mean depth of 2.6 m (section 2.4). Two sand barrier islands named Isla del Carmen, on which Ciudad del Carmen is located, and Isla Aguada separate the lagoon from the adjacent continental shelf. The length of Isla del Carmen is circa 36 km and the width varies between 800 m and 5.5 km. Isla Aguada has a length of 41 km and a width varying between 500 m and 3 km.

There are two principal coastal tidal inlets: the Carmen inlet, located southwestern of Isla del Carmen, with a width of 3.3 km, and Puerto Real inlet located between Isla del Carmen and Isla Aguada, with a width of 3.0 km. The last and third inlet is Sabuncuy inlet, which is located 43 km northeast of Puerto Real. As described in Section 1.4, the Sabuncuy inlet is not taken into account in this study, because of the relatively small net

flow in comparison with the principal inlets [23]. The marine waters predominantly enter the lagoon through the eastern inlet and exit the lagoon through the western inlet [20]. However, some researchers argue the opposite direction [23].

The western boundary of the lagoon is formed by the Usumacinta delta, which is the main sediment source of the lagoon [16]. The Palizada river is a tributary of the Usumacinta river, which is the largest river of the Terminos Lagoon discharging rivers. Two other main discharging rivers are the Chumpan river and the Candelaria-Mamantel rivers. Additionally Terminos Lagoon receives water from the Muerto, Palancare and the Sabancuy River, the Colax, Lagartero, Chivoj Chico and Chivoj Grande streams [25]. These last seven rivers are not taken into account in this report for reasons described in section 1.4.

2.2. Seasons

Literature research about the different seasons of Terminos Lagoon has been carried out. Yáñez-Arancibia and Day (1982) give a description of the seasons of Terminos Lagoon which is cited by 100 referred journal articles:

> *There are three "seasons" in this region. From June until the end of September, there are almost daily afternoon and evening showers. From October into March is the season of "Nortes" or winter storms. These storms are generally strongest and associated with rains during November, December and January. February through May is the dry season.* [71]

Some researchers claim that May is a transition season that should not be considered as a part of the dry season [26]. However, in this report the seasons are considered to be the same as the research by Yáñez-Arancibia and Day (1982):

- dry season, February - May;
- rainy season, June - September;
- Nortes season, October - March.

There is an overlap between the dry season and Nortes season in February and March, because Nortes is defined by the dominant wind direction.

2.3. Geology

Figure 2.2 shows the surface geology near Terminos Lagoon. The total list of soil types in the region of Yucatan Peninsula, of which Terminos Lagoon is part, is given in appendix B with a short description. The numbers corresponding to the area of Terminos Lagoon are given in table 2.1 [13]. The geomorphic landscapes are indicated by numbers. There is an undulating plain in the northeast of the lagoon, which is a plain with a wavy surface. The other geomorphic landscapes are plains, which have a gentle slope. Table 2.1 shows that there are fluvial paludal environments, with river deposits and swamp deposits and coastal environments with deposits from the sea. The present deposits in the area of Terminos lagoon are mixes of leptosols, cambisols, gleysols, solonchak, regosols and arenosols, see appendix B.

There are no open source boring tests of the area. However, from the stratigraphic columns of Chicxulub crater research, which lays 300 km north-east, can be found that the first 300 m consists of limestone and marl [63]. Boring tests need to be performed to determine the exact aquifers and aquitards of the study area, at least one boring in every geomorphic landscape, as listed in table 2.1.
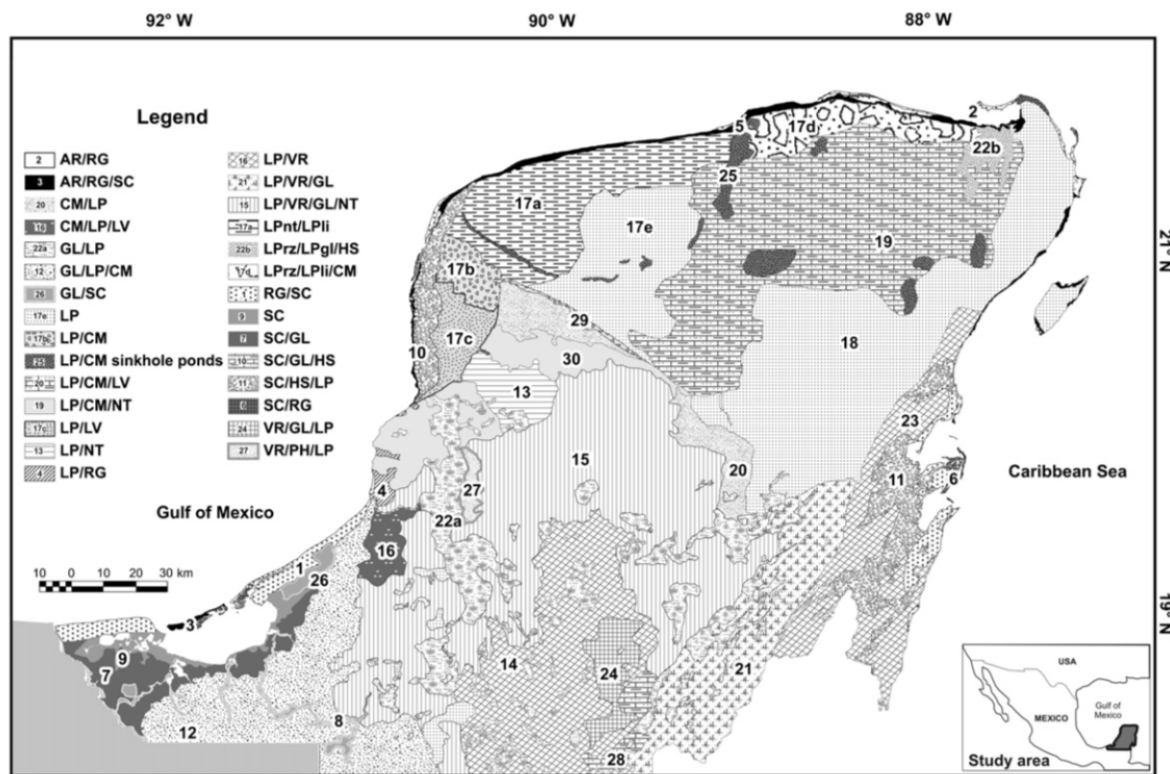
Figure 2.2: Surface geology map of Yucatan Peninsula with Terminos Lagoon in the left bottom corner and with: LP=Leptosols, CM=Cambisols, VR=Vertisols, GL=Gleysols, SC=Solonchak, RG=Regosols, AR=Arenosols, NT=Nitisols, PH=Pheozems, HS=Histosols, nt=Nudilithic, li=lithic, rz=Rendzic, and gl=gleyic [13]

Table 2.1: Geomorphic landscapes of Terminos Lagoon with LP=Leptosols, CM=Cambisols, GL=Gleysols, SC=Solonchak, RG=Regosols and AR=Arenosols

Nr.	Environment	Geomorphic landscape	Altitude [m.a.s.l.]	Slope [%]	Rock type	Surface [ha]
1	Coastal	Undulating plain	0-4	0-2	RG/SC	233.593
3	Coastal	Plain	0-4	0-2	AR/RG/SC	20,204
7	Fluvial-paludal	Plain	0-35	0-5	SC/GL	227,685
9	Fluvial-paludal	Plain	0-35	0-5	SC	88,529
12	Fluvial-paludal	Plain	0-35	0-5	GL/LP/CM	885,307
26	Fluvial-paludal	Plain	2-20	0-5	GL/SC	38,450

One of the geohazards of areas with calcareous rocks is karst, which is a common geohazard in Yucatan Peninsula as well. This area is characterised by landforms of dissolution such as sinkholes, also known as cenotes. Figure 2.3 shows the development of karst in Yucatan Peninsula. The development of karst in Terminos Lagoon is relatively small in comparison with other areas in Yucatan Peninsula. At the north-east site of Terminos Lagoon, development of karst is relatively high. Figure 2.4 shows the locations of fractures in Yucatan Peninsula. The map shows that there are no fractures in the area of Terminos Lagoon.
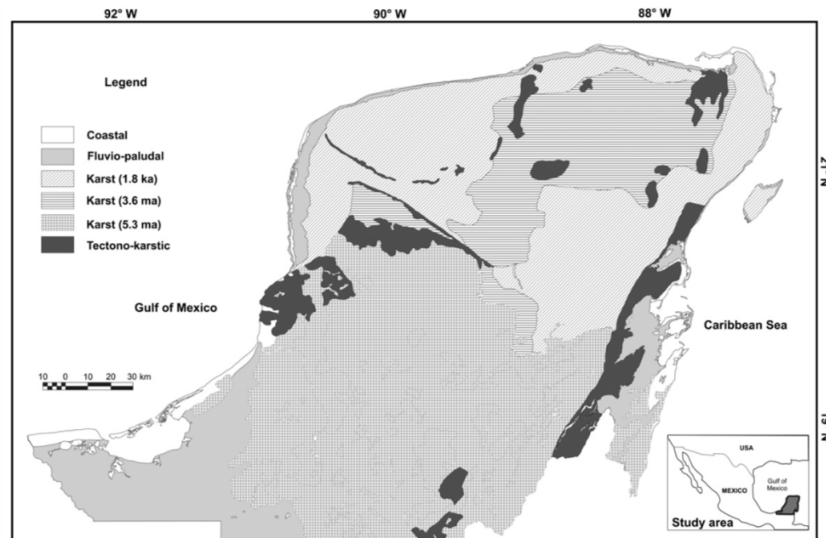
Figure 2.3: Schematic map with stages of karst development in Yucatan Peninsula in kiloannum or megaannum, [ka] or [ma] and with Terminos Lagoon in the left bottom corner [13]
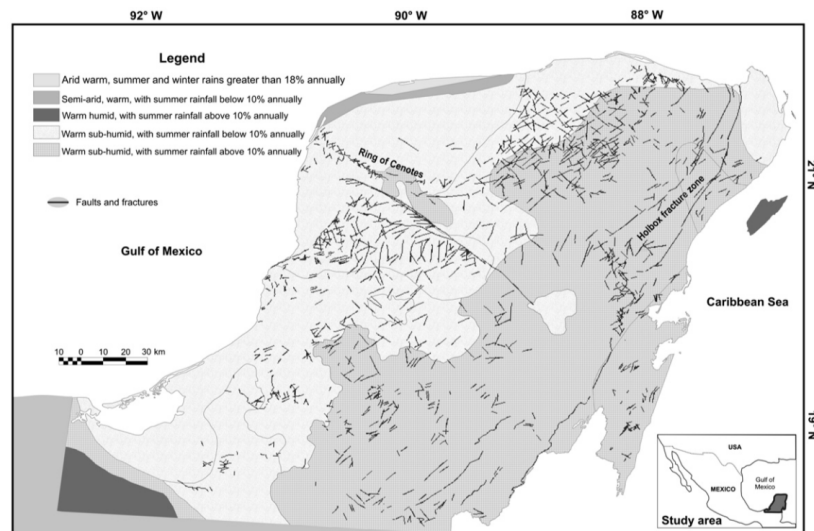
Figure 2.4: Schematic map of fractures in Yucatan Peninsula with Terminos Lagoon in the left bottom corner [13]

2.4. Bathymetry

The data used for the bathymetry originates from Secretaría de Marina (SEMAR) and National Institute of Statistics and Geography of Mexico (INEGI) [30, 53–56]. The bathymetry of the lagoon is shown in figure 2.5. The average depth of the lagoon is approximately 2.6 m with respect to mean sea level (MSL). The deepest point can be found in the navigation channel of the Carmen inlet, which is around 11 m below MSL.

(a) Depth range between -12.0 m – 0.5 m relative to MSL (b) Depth range between -4.5 m – 0.0 m relative to MSL
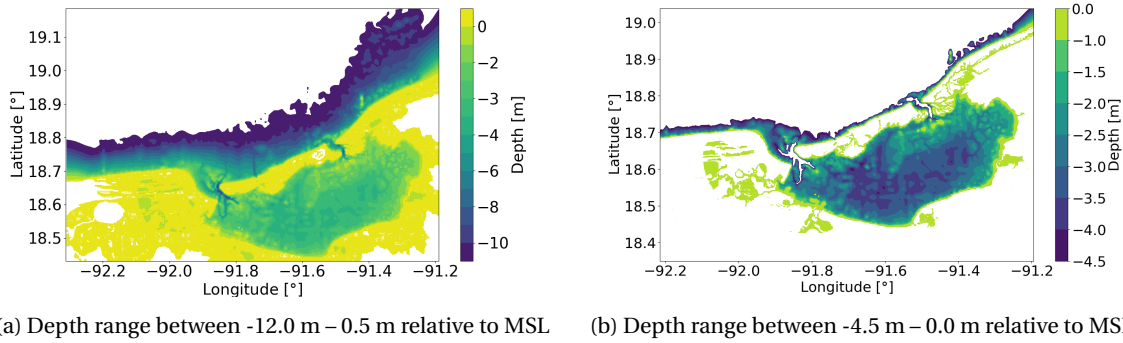
Figure 2.5: Bathymetry of Terminos Lagoon with depth in meters below mean sea level [30, 53–56]

Furthermore, the bathymetry shows that the water depth is smaller on the northeast side of the lagoon and larger on the southeast side of the lagoon with the exception of the Palizada river discharging area. The lagoon is shallower where the Palizada estuary is located. This is probably caused by deposition of sediment, which comes from the river. The bathymetry shows that there is no clear distinction between tidal flats and tidal channels. The Puerto Real inlet has an extensive flood tidal delta, there is no visible ebb tidal delta. These deltas have changed over time. The Carmen inlet does not show any tidal deltas, this probably indicates that this inlet is not tide dominated. In the main body of the lagoon, the bathymetry does not present channels or intertidal flats, so there is almost no intertidal storage. This indicates a flood dominant system and the residual transport for coarse sediment is in flood direction. This means that there is sediment import.

The cross-sections of the Carmen inlet and Puerto Real inlet are shown in figure 2.6. The maximum depth of Carmen inlet of the cross section is 10.4 m and the maximum depth of the Puerto Real inlet is 5.6 m, see figure 2.6b.

(a) Location of the depth cross-sections, based on NASA Earth Observatory [21] (b) Cross-section of the Carmen and Puerto Real inlets with distance from southwestern point of cross-section to northeastern point
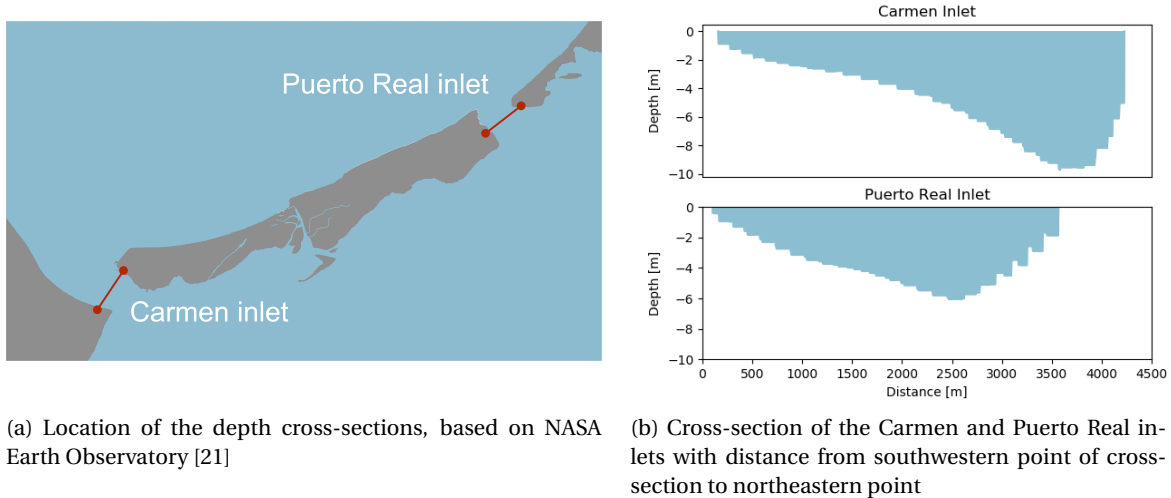
Figure 2.6: Map with the location of the cross-section lines and the depth cross-sections of the Carmen inlet and Puerto Real inlet

3

Data collection

In this chapter the data collection is described. The described data are necessary to obtain answers to the main research and sub-questions posed in section 1.3. For each data set, a description is given of the method and location of the measurements. The data collections are divided by their measurement method. First, data from the measurement stations are described. These stations measure parameters relevant to the water balance, as well as some spatial characteristics. Secondly, an overview of used remote-sensed data is given. These are used to look into the distribution of some spatial characteristics and to determine morphological features of Terminos Lagoon. Afterwards, field measurements are described, which are direct measurements of the spatial characteristics listed in section 1.3. Last, a brief description of the Delft3D-FLOW model is given, used to determine the lagoon hydrodynamics.

3.1. Measurement stations
The location of the measurement stations used in this research are shown in figure 3.1. The weather station in Villahermosa and the Palizada river discharge station are not included in figure 3.1.

Figure 3.1: Map with locations of measurement stations of SEMAR, E.Pargo, airport weather station and CONAGUA station at Isla del Carmen based on NASA Earth Observatory [21]

Ciudad del Carmen coastal observatory from ICML-UNAM is collecting data continuously at two different locations in Terminos Lagoon: E.Pargo (Estero Pargo Estation), located in a creek close to the coastal observatory station of the ICML-UNAM, and SEMAR Estation (Secretaría de Marina), the marine harbour in Ciudad del Carmen, see figure 3.1. These locations are chosen as measuring equipment can be left standing here undisturbed.

At the observatories SEMAR and E.Pargo, the same type of measurements have been collected. The measurements were taken every 30 minutes, starting in October 2016 up to August 2018. The measurements are used

to define the correlation between spatial characteristics and hydrological processes. The following parameters were measured:

- water pressure [kPa];
- electrical conductivity [μS/cm];
- concentration of dissolved oxygen [mg/L];
- atmospheric temperature [°C];
- water temperature [°C].

Furthermore, a dataset of the discharge of the Palizada river is provided by the ICML-UNAM. This dataset has an interval of 22 years, with the daily discharge in m^3/s, from April 1992 to December 2014.

The Ciudad del Carmen airport has an observatory providing weather data in Mexico. The location of the weather station corresponding to Terminos Lagoon is located at Ciudad del Carmen's airport. The airport weather station provides hourly data from January 1972 until December 2016. The data are used to determine the evaporation and air temperature. The variables measured by the airport weather station are:

- atmospheric temperature [°C];
- relative humidity [%];
- wind speed [km/h] and direction [°].

Moreover, the precipitation and atmospheric temperature are measured at CONAGUA station (Comisión Nacional del Agua), located near E.Pargo, see figure 3.1. The data lasted from September 1984 till August 2018. However, the data before 1986 are not used, as precipitation data in the year 1985 contained unrealistic values with respect to other years. The delivered precipitation values of 1985 were marked as erroneous.

The duration of the bright sunshine hours is measured in Villahermosa, a city about 150 km south-west of Terminos Lagoon. Sunshine duration is measured in monthly averages from January 1961 till December 1990 at the weather station in Villahermosa [69]. The duration of the bright sunshine hours is used for the calculation of evaporation in subsection 4.1.2.

To summarize, figure 3.2 provides an overview of the time duration and type of data collected from measurement stations.
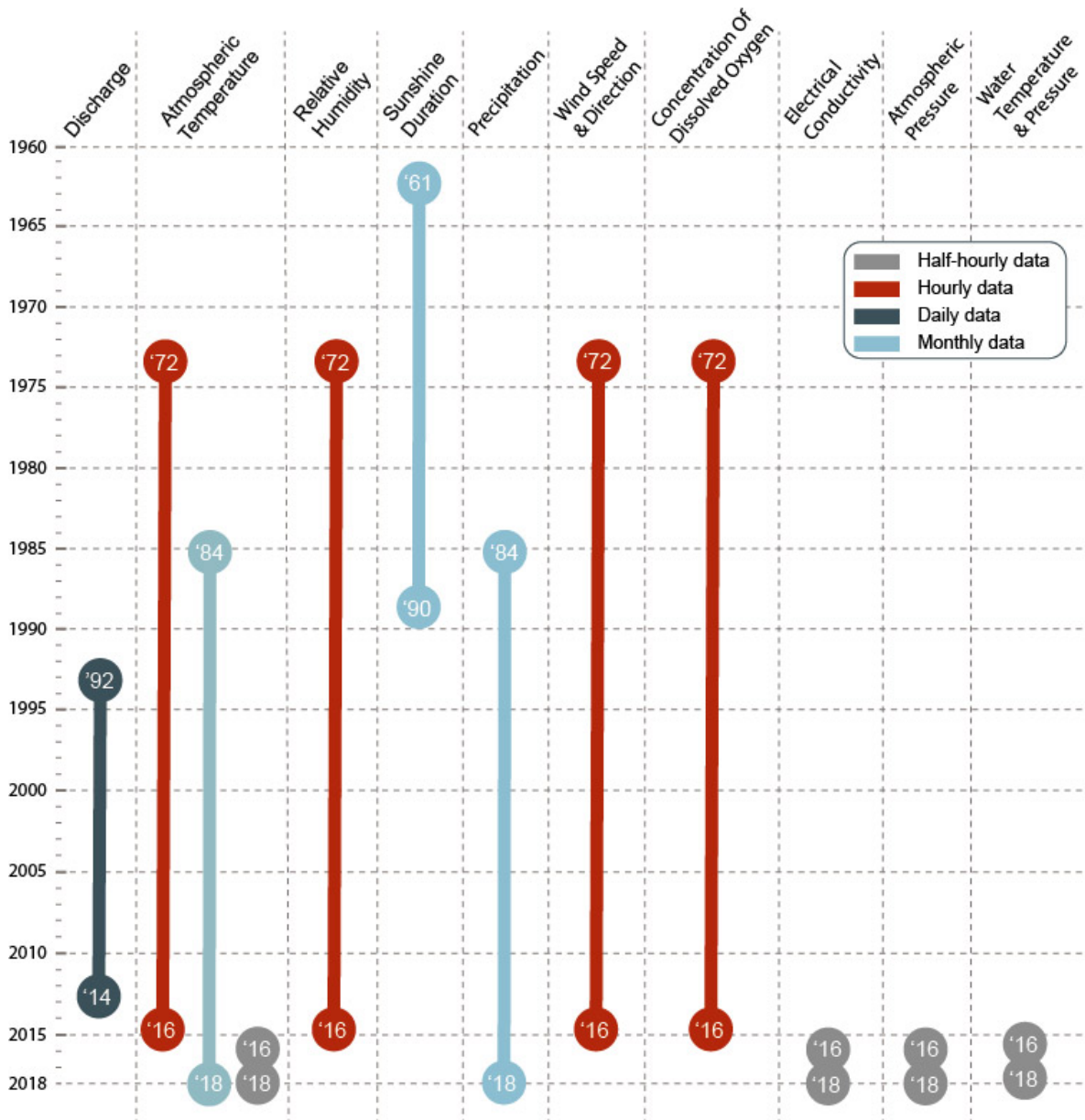
Figure 3.2: Timeline of the data from measurement stations

3.2. Satellite Imagery

In addition to in-situ collected data, satellite imagery is used to map changes in morphology of the lagoon, as well as surface temperature variations within the lagoon. Satellite imagery is available from an earlier point in time than most field measurements. For the purpose of this research, imagery with qualities in the visible and thermal spectrum are used. To this end, only open source imagery is considered. All satellite imagery is limited by overpass frequency, spatial resolution and time in orbit. These factors are considered when making the choice between data sources.

To look into surface temperatures, the available options still in orbit are Landsat 7 and Landsat 8, with comparable spatial resolution. Landsat 8 is equipped with two dedicated thermal infra-red sensors, making it the better choice between the two [4]. Landsat 8 is used to look into surface temperature fluctuations throughout the lagoon for varying seasons. The same images are used to determine Secchi depth distribution.

Surface area of the lagoon basin and of the tidally influenced areas surrounding it, is determined using a Landsat 8 image with low cloud cover. Its moderate spatial resolution of 30 m is adequate for purposes at

hand. Tidal inlet widths are analysed using Landsat 4-5 Thematic Mapper, Landsat 7 and Landsat 8 images; imagery with comparable spatial resolution and a data record dating back to the 1980's. It is the only open source set of imagery with such a long data record, which is required to study morphological changes. Secchi depth is also determined using Landsat 8 images, as chosen methodology proved to be relatively easy to implement on these. Another advantage is that thermal maps and Secchi depth maps can be compared for the same moment in time. In appendices A and C, D and E, explanations are given on methodology applied to extract information from mentioned imagery.

3.3. Fieldwork

A fieldwork campaign is set up by ICML-UNAM to collect in-situ data from the lagoon. The most recent campaign consisted out of two days: 5 and 7 September 2018. During the campaign, water samples are collected and various measurements are done. At the first day of the campaign, data are collected in a line from the Puerto Real inlet to the Candelaria-Mamantel river. This campaign was the first of its kind. During the second day a similar pattern of measurements is set out for the Carmen inlet and the Palizada river, similar campaigns are performed each September, starting in 2016.

The locations are chosen to obtain information most efficient, hence the choice for points from river to tidal inlet. There are two measurements in the river, one or two near the outlet of the river, two in the lagoon, two near the tidal inlets, one in the sea and a last one at SEMAR. The exact locations of the measurements performed in 2018 can be found in figure 3.3.
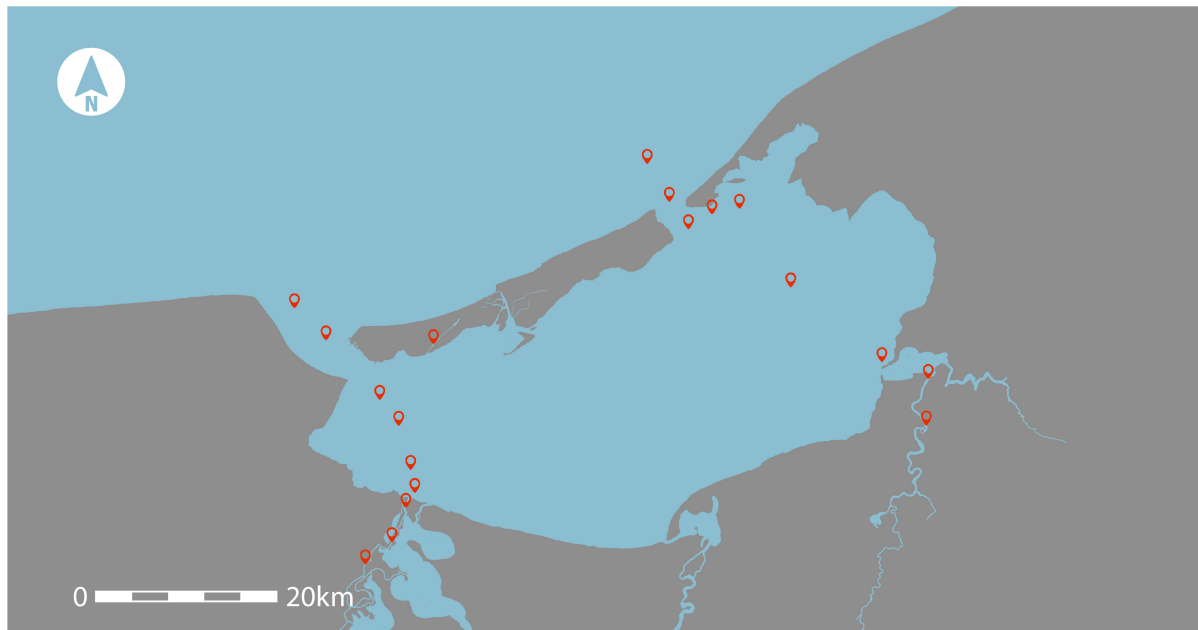
Figure 3.3: Fieldwork measurement locations in Terminos Lagoon based on NASA Earth Observatory [21]

At each measurement location various measurements are done. Locations are noted by their GPS locations. Temperature, salinity, oxygen content, dissolved oxygen (DO), total dissolved solids (TDS) and conductivity are measured at every half meter using an EXO Multiparameter sensor. The Secchi depth is measured with a Secchi disk. A Secchi disk is a circular plate with a diameter of 20 cm, painted alternately in black and white quarters. The Secchi depth is the depth at which the disk just not disappears from view [10].

3.4. Delft3D-FLOW modelling

Delft3D-FLOW is a finite element hydrodynamic model of Deltares and made for Terminos Lagoon by ICML-UNAM. The domain, boundary conditions and input parameters of the Delft3D-FLOW model are given in appendix F. The model is used to investigate the hydrodynamic processes of the lagoon. There are three Delft3D-FLOW models used with different combinations of driving forces:

- tides;
- tides and wind;
- tides, wind and the Palizada river discharge.

Using the data of the Delft3D-FLOW models, the main current can be defined, as well as the direction of the flow and the presence of tidal watersheds. Moreover, the influence of the river on the lagoon is calculated, as well as salinity distribution.

Data analysis & theory

This chapter is divided in four different sections: hydrological processes, hydrodynamic processes, spatial characteristics and statistical dependence. In these different sections the data described in chapter 3 are visualised and the theory behind the methods is explained.

4.1. Hydrological processes

In this section different hydrological processes are discussed. The precipitation, evaporation, river flow and groundwater flow are determined in order to determine the water balance of Terminos Lagoon which will be given at the end of this section. The different terms of the water balance give an insight in the (amount of) in- and outflow of the lagoon.

4.1.1. Precipitation

The annual sum of precipitation in Ciudad del Carmen is 1534 mm, measured daily over a period of 30 years by CONAGUA. Figure 4.1a shows the total monthly precipitation measured from January 1986 till August 2018, where the average monthly precipitation is 128 mm. Due to monthly variations, different seasons can be distinguished. The rainy season starts in June, which shows high precipitation rates in comparison with previous months. During the dry season precipitation rates are below 75 mm per month, which is low compared to the average monthly precipitation. The amount of precipitation varies within the Nortes season, but with significantly lower precipitation rates than during the rainy season. Figure 4.1b shows the box plot of the precipitation, more information about the interpretation of a box plot can be found in appendix G. In this figure, monthly variation is largest during the rainy season, where the precipitation rate is high.

(a) Average monthly precipitation from January 1986 - August 2018

(b) Box plot of the precipitation, see appendix G for a description of box plot features
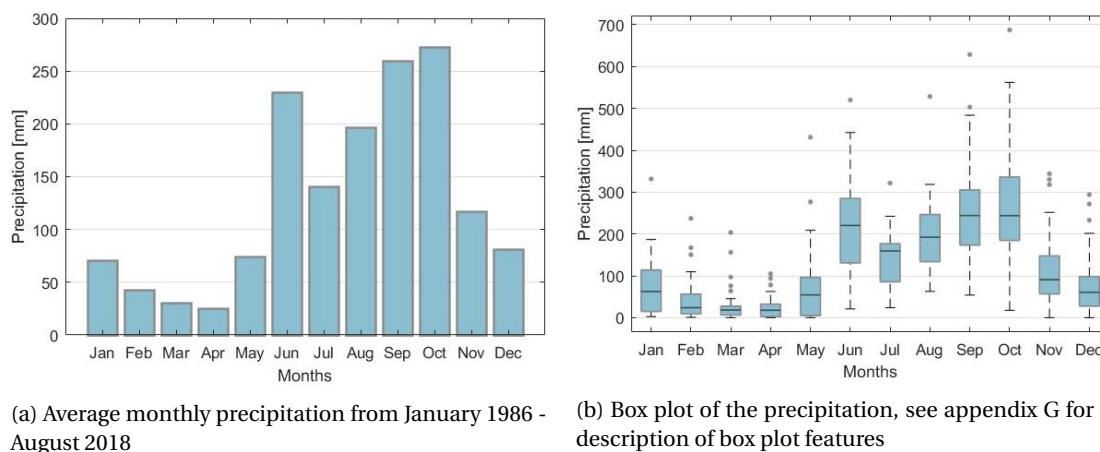
Figure 4.1: Intra-annual variation of precipitation from CONAGUA station, January 1986 - August 2018

In table 4.1 the precipitation rates in millimeter per month can be found. Average precipitation rates are

calculated per season and per year. Next, the precipitation is converted into cubic meter per second, where the amount of precipitation in mm/month is multiplied by the area of the lagoon of 1690 km^2 and divided by a time factor.

Table 4.1: Annual and seasonal mean precipitation from January 1986 - August 2018

Season	Mean precipitation [mm/month]	Mean precipitation [m^3/s]
Dry	42.7	27.4
Rainy	208.9	134.0
Nortes	100.2	64.3
Annual	*128.6*	*82.5*

4.1.2. Evaporation

Evaporation requires two processes to occur. First, there must be an energy supply to provide heat of vaporization. Secondly, a transport mechanism must be there to remove the vapour [29]. After combining both concepts, it is possible to derive an expression for evaporation that depends on measurable weather elements. By making approximations, the needed weather data reduce to four components:

- daily mean atmospheric temperature [°C];
- relative humity [%];
- wind speed [m/s];
- duration of bright sunshine [h].

The obtained quantity is the evaporation rate (E$_0$) for an open water surface exposed to the measured weather. This method is commonly known as the Penman Method, developed by Howard Penman in 1948 [29]. Temperature, humidity and wind data of the Ciudad del Carmen airport weather station (section 3.1) are used to calculate the evaporation. Data over a period of 30 years, from January 1987 until December 2017, are used to describe the current climate of the area. Next, the density of water in the lagoon is assumed to be 1020 kg/m^3 [62]. The open water evaporation E$_0$ is calculated using equation 4.1. More information about the formulas and method can be found in appendix H, formula H.2 - H.7.

$$E_0 = \frac{\left\{ \dfrac{sR_N}{\rho\lambda} + \dfrac{c_p\rho_a}{\rho\lambda}\dfrac{(e_s - e_a)}{r_a} \right\}}{s + \gamma} \tag{4.1}$$

With:

R_N	= Earth's net radiation	[J day^{-1}m^{-2}]
λ	= heat of evaporation (λ= 2.45 MJ/kg)	[J/kg]
s	= inclination evaporation curve	[kPa K^{-1}]
c_p	= specific heat of air with constant pressure (c$_p$ = 1004 J kg^{-1}K^{-1})	[J kg^{-1}K^{-1}]
ρ_a	= density of air (ρ_a = 1205 kg/m^3)	[kg/m^3]
ρ	= density of water (ρ= 1020 kg/m^3)	[kg m^3]
e_a	= actual vapour pressure of the air at 2 m height	[kPa]
e_s	= saturation vapour pressure	[kPa]
γ	= psychrometric constant (γ= 0.066 kPa/°C)	[kPa K^{-1}]
r_a	= aerodynamic resistance	[day m^{-1}]

Atmospheric temperature and humidity

The saturated vapour pressure (e$_s$) and the inclination of the saturated vapour pressure (s) are calculated using atmospheric temperature data as input value. The saturated vapour pressure is the maximum possible vapour pressure where condensation does not occur yet. The atmospheric temperature of Terminos Lagoon is depicted as a box plot in figure 4.2a. The atmospheric temperature fluctuates around 28 °C. The data that are used for the plot comes from the weather station at airport Isla del Carmen, from January 1987 until December 2016, see also chapter 3. The average atmospheric temperatures per season are given in table 4.2.

During the dry season (February-May), the average atmospheric temperature increases. The median of the atmospheric temperature is constant over the rainy season. For the first half of the Nortes season the median of the atmospheric temperature decreases, while it increases for the second half. The change in atmospheric temperature throughout the year is relatively small in comparison with for instance the Netherlands, where the atmospheric temperature fluctuates between -10 °C and 35 °C [65]. A maximum atmospheric temperature measurement of 58 °C, as well as a minimum measurement of 2 °C, is unrealistic, as these outliers have a difference of 10 °C with measurements within half an hour.

Table 4.2: Annual and seasonal mean atmospheric temperatures from January 1987 - December 2016

Season	Mean atmospheric temperature [°C]
Dry	27.8
Rainy	29.2
Nortes	26.2
Annual	*27.7*
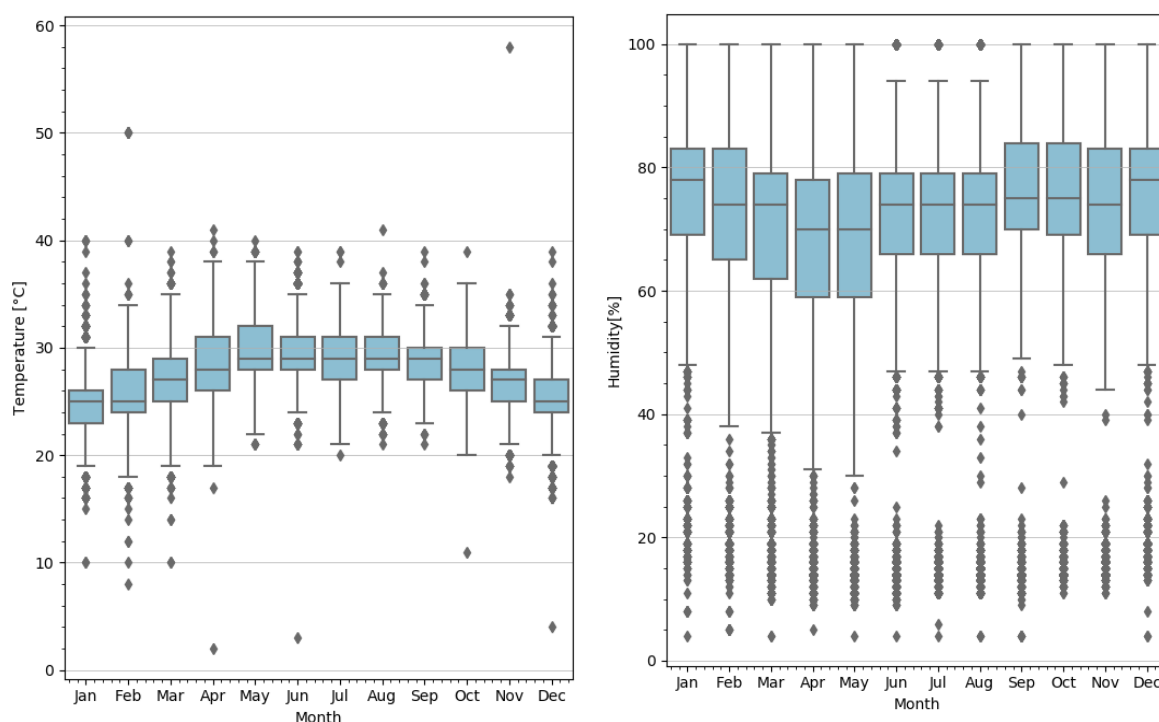
(a) Temperature box plot of hourly data from January 1987 - December 2016, see appendix G for box plot features

(b) Relative humidity box plot of hourly data from January 1987 - December 2016, see appendix G for box plot features

Figure 4.2: Temperature and humidity box plot of hourly data from Ciudad del Carmen airport, January 1987 - December 2016

In order to determine the actual vapour pressure, information about the humidity is needed. Humidity is the amount of water vapour in the air, the higher the humidity, the less water can be evaporated. The relative humidity is plotted in 4.2b, with the use of a box plot. The region is humid all year round, with an average yearly humidity of 67 %, a peak in December and January and a minimum around April and May. Now, the actual vapour pressure (e_a) can be determined by multiplying the saturated vapour pressure with the relative humidity.

Wind

Terminos Lagoon is located in a zone with trade winds or, more specifically, tropical easterlies. These trade winds travel from the subtropical high zone at 30 °N towards the equator. The Coriolis effect deflects the trade

winds to the right, resulting in moderate Northeast trades. These winds are persistent throughout the year. However, these winds could be overruled by tropical seasonal winds [14]. The Nortes season distinguishes itself by strong winds. The rest of the year the main wind direction is formed by a sea breeze system, with winds predominantly from the north and the east-southeast [71]. Wind roses are made using Ciudad del Carmen airport wind data. Main wind directions, frequencies and wind speeds are represented by these wind roses. The wind directions, wind speed and frequency of a time period of 30 years (1987-2017) are shown in figure 4.3.

High wind speeds are most frequent during dry season and lowest wind speeds are observed during rainy season. Looking at the frequency of occurrence, the main direction of the wind is observed to be east-southeast. The direction of the strongest winds is north and north-northwest with speeds higher than 46 km/h. The dry season and Nortes have an overlap in February and March which leads to a relatively similar wind rose.

(a) Dry season

(b) Rainy season

(c) Nortes season
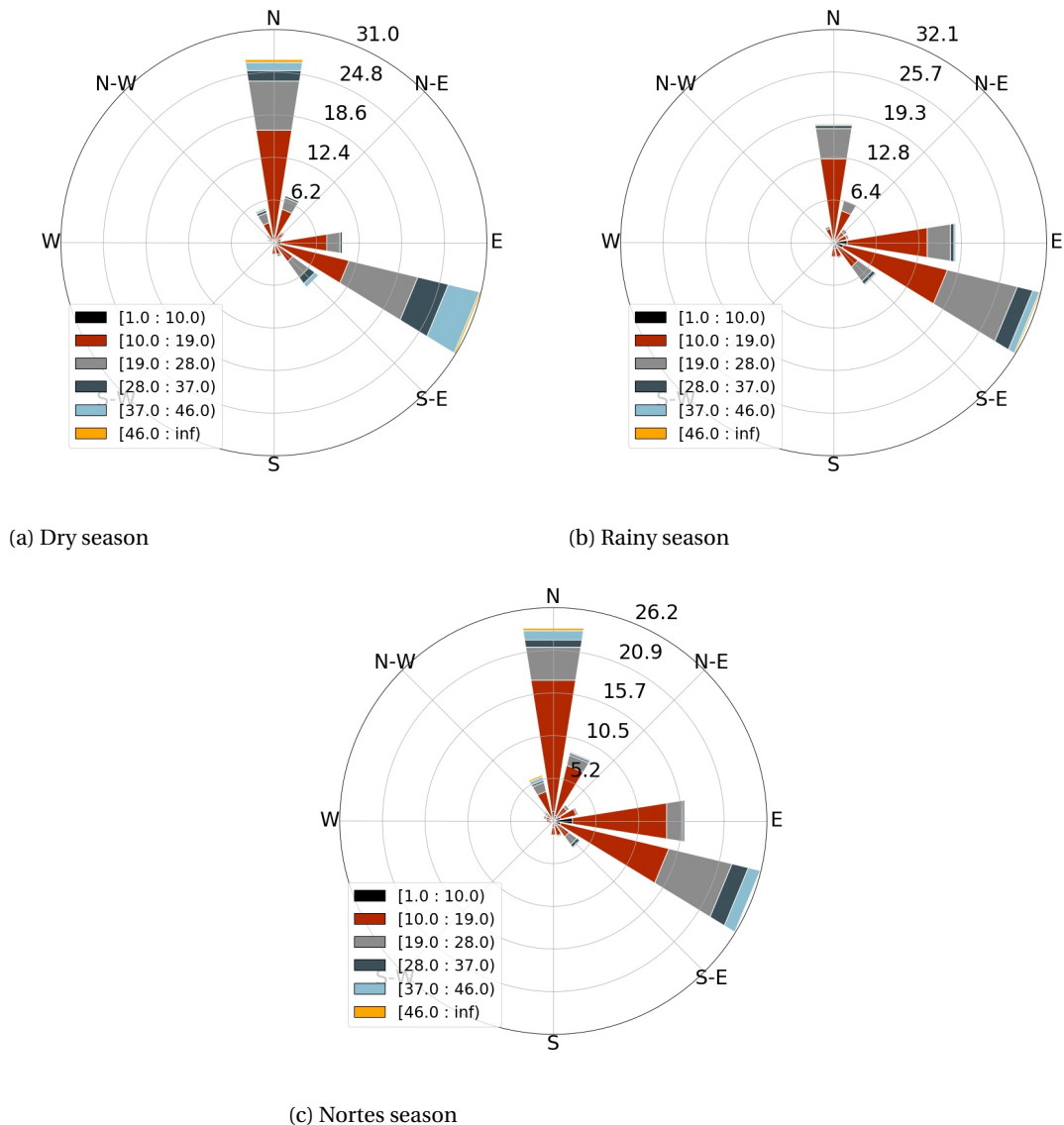
Figure 4.3: Windroses per season with wind speed in km/h in colortable and frequency in percentage on axis of hourly data from Ciudad del Carmen airport, January 1987 - December 2016

Using the wind speed, the aerodynamic resistance r_a can be calculated. Here, an empirical formula is used, with the wind speed at 2 m height as input value [52], which is elaborated in appendix H.

Solar radiation

The net radiation (R_N) is the difference between incoming short-wave radiation R_c and reflection from the Earth's surface by short-wave ($R_c \cdot a$) and long-wave radiation R_b. The reflective shortwave radiation is determined by the albedo factor (a). The schematic energy balance is shown in figure 4.4. In order to calculate the net radiation, the amount of bright sunshine hours divided by the length of the day, is required. It is assumed that the data of Villahermosa is similar to the Terminos Lagoon (chapter 4). Empirical tables are used to determine the outgoing short-wave and long-wave radiation [52]. Subsequently, net radiation is found with an empirical formula, using the assumption that the climate of Terminos Lagoon is similar to the climate of New Delhi. The difference in latitude between Terminos Lagoon and New Delhi is small, compared to the differences in latitude between Terminos Lagoon and other locations where an empirical formula for evaporation rate is available.
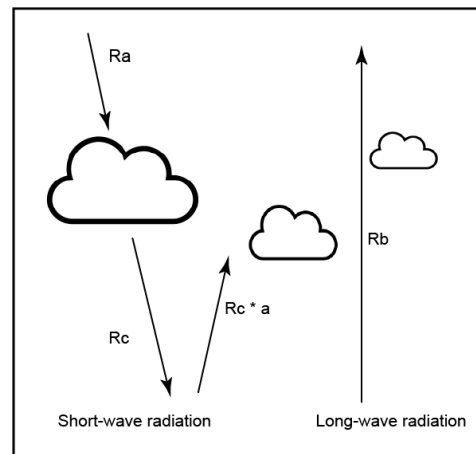
Figure 4.4: Schematic energy balance for solar radiation

4.1.3. Evaporation rates

Finally, using equation 4.1, the open water evaporation is determined, as a yearly average and an average per season in mm/day and in m^3/s. This can be found in table 4.3.

Table 4.3: Total open water evaporation

Season	Evaporation [mm/day]	Evaporation [m^3/s]
Dry	6.4	125.2
Rainy	7.1	138.9
Nortes	4.9	95.8
Annual	*5.6*	*109.5*

4.1.4. Rivers

There are four main watershed-river systems that flow into Terminos Lagoon, see figure 4.5. The Palizada river is part of one of the longest and most important rivers of the state, as it is the eastern branch of the Usumacinta River. The Usumacinta branches at the mouth of Amatitlán, 25 km upstream from the town of Amatitlán. It forms a natural boundary between the states of Campeche and Tabasco before it heads northeast to the area of Palizada. There it branches into the Palizada river, which finally opens to Terminos Lagoon. Another river is the Chumpan river, which develops in the coastal plain through Salsipuedes and San Joaquin river [47]. The river opens into the Laguna El Sitio Viejo, which flows into Terminos Lagoon. On the central southern-shore, the Candelaria river together with the Mamantel river are forming the Panlau Lagoon, which is connected to Terminos Lagoon through the Pargos outlet. The river systems are the main contributors of fresh water and sediments to Terminos Lagoon [47].

Figure 4.5: Map representation of the location of the main river systems based on NASA Earth Observatory [21]

River discharge

The discharge of the Palizada river is examined, using information described in section 3.1. To give insight in the flow of the Palizada river, the average monthly discharge is determined using daily discharge data. This is plotted over the years in figure 4.6a. As data is provided on daily basis, the tidal influence on the discharge is not visible. It is found that the discharge varies over the year and over the acquisition time, with a maximum of 700 m^3/s in September 2010 and a minimum of 60 m^3/s in April 2010. A box plot is used to illustrate statistic measures of central tendency and dispersion for monthly discharge. From figure 4.6b it can be observed that the minimum average monthly discharge occurs in May, where there is a median of 75 m^3/s, while a maximum discharge of 420 m^3/s is reached in October. As the Palizada is a rain-fed river, the yearly discharge pattern is roughly in line with the precipitation pattern (4.1b).
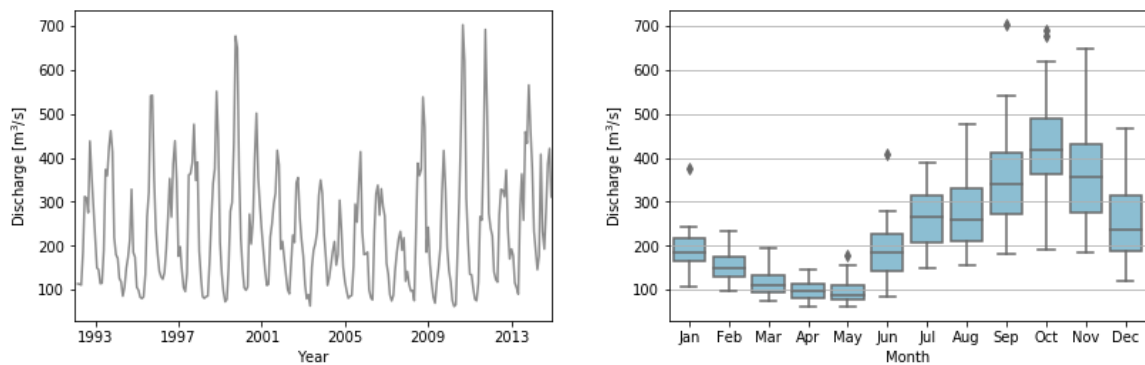
(a) Average monthly discharge [m^3/s] from April 1992 - December 2014

(b) Box plot of the monthly discharge, see appendix G for box plot features

Figure 4.6: Average monthly discharge Palizada river from ICML-UNAM data, April 1992 - December 2014

The Chumpan, Mamantal and Candelaria rivers are small compared to the Palizada river. The ICML does not have discharge data series available and there are no open sources. Therefore, literature is used to approximate the seasonal and average yearly discharge of these rivers. The mean discharge of the river Chumpan is 18 m^3/s [47]. On the central southern shore there are two fresh water inflows, the Candelaria of 67 m^3/s and the Mamantal with a flow of 5 m^3/s [47]. The river discharges per season are summarized in table 4.4, where the Chumpan, Mamantal and Candelaria river are combined as one inflow.

Table 4.4: Average seasonal discharge of Palizada river from April 1993 - December 2014, and average seosonal discharge of Chumpan, Candelaria and Mamantal river [47]

Season	Discharge Palizada [m³/s]	Discharge Chumpan, Candelaria and Mamantal [m³/s]
Dry	115	29
Rainy	271	120
Nortes	256	104
Annual	*234*	*90*

River influence

To determine the effect of the Palizada river, two Delft3D-FLOW models are used. One model includes tides, wind and the Palizada river, and the other model includes only tides and wind. The effect of the river on the lagoon is determined by subtracting the salinity in the case the Palizada river is included by the salinity in the case there is no Palizada river simulated. In figure 4.7 this effect on the salinity in Terminos Lagoon for different seasons is shown.

(a) Dry season

(b) Rainy season

(c) Nortes season
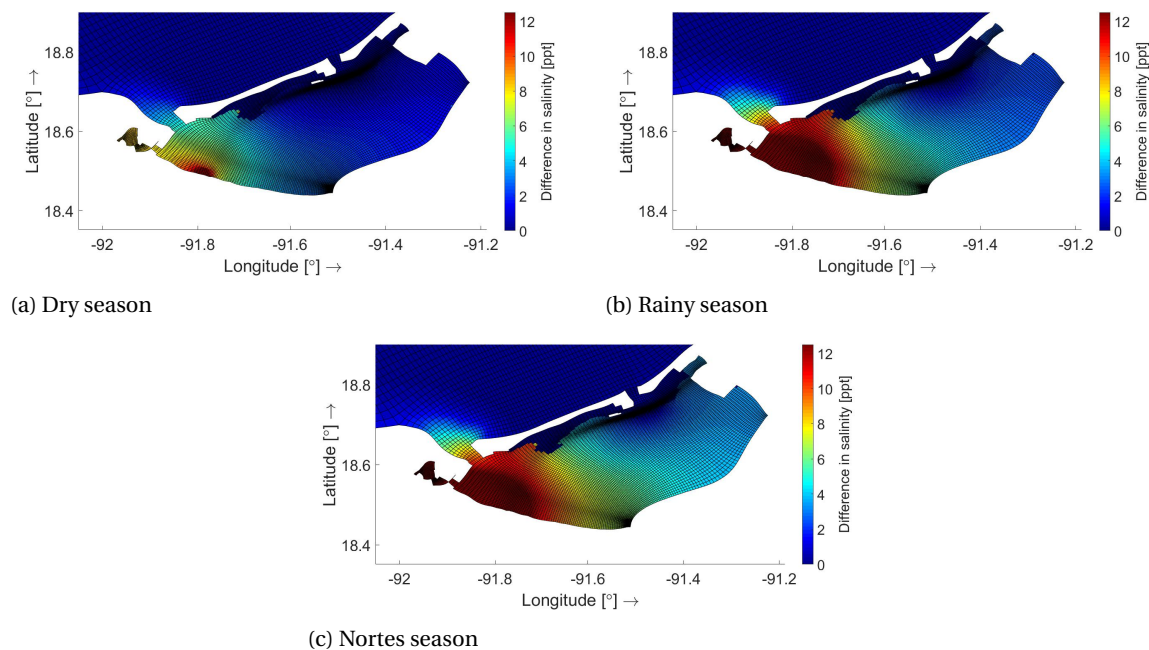
Figure 4.7: Difference in salinity for a situation with and without Palizada river, from Delft3D-FLOW

4.1.5. Groundwater flow

Rain water and sea water infiltrate through permeable limestone and marl layers. The total groundwater discharge (Q [m³/day]) can be calculated with Darcy's law [67]:

$$Q = KA\frac{\Delta h}{\Delta L} \tag{4.2}$$

With:

K	= hydraulic conductivity	[m/day]
Δh	= hydraulic head gradient	[-]
ΔL	= distance between two points	[-]
A	= area of the flow	[m²]

The hydraulic conductivity of the limestone marl layer depends on the degree of fracturing and is assumed to be equal to $7 \cdot 10^{-5}$ m/s for the matrix and $1 \cdot 10^{-3}$ m/s for the fractures [70]. However, figure 2.4 (section

2.3) shows that there are no fractures in the study area. Therefore, a hydraulic conductivity of 7x10^{-5} m/s is chosen. The hydraulic conductivity of the limestone and marl layers can be determined more precise with a falling head test [67] or other laboratory tests if samples are available.

The hydraulic head in the aquifers is required to determine the groundwater flow. Smith et al. (1999) determined the groundwater flow to Terminos Lagoon with a permeability range for gravel and silt and the largest measured hydraulic head difference [57]. To give an approximation of the groundwater discharge the difference in hydraulic gradient times the area from the research of Smith et al. (1999) is used with a hydraulic conductivity of 7·10^{-5} m/s:

$$Q = KA\frac{\Delta h}{\Delta L} = 7 \cdot 10^{-5} \cdot 243.921 = 0.017074 \, m^3/s \tag{4.3}$$

4.1.6. Water balance

A water balance is set up in order to understand the water system of Terminos Lagoon. The overview of the yearly average water balance in figure 4.8 shows that the exact amounts of the water balance terms range from 0 to 324 m^3/s. The yearly average water balance indicates a large influence of river discharge on the lagoon system, as this is the largest term in the water balance. Precipitation and evaporation have the same order of magnitude. Both terms are relatively small compared to the river discharge and net flow of the inlets. The groundwater flow is negligible small (chapter 4.1.5). An assumption is made that the permeability of the surface deposits, (chapter 2), is relatively high. Due to this assumption and the high vegetation levels near the shore, water will infiltrate earlier than it could runoff. Therefore, the runoff is neglected in the water balance. Now, the net flow through the inlets, which is seaward directed, is mainly caused by the river discharge. This net flow through the inlets is the largest outflow component of the water balance. As explained later in section 4.2.3, there is a residual current from the Puerto Real inlet towards the Carmen inlet. Therefore, the net outflow through the Carmen inlet is expected to be larger than 293 m^3/s. The quantities of the water balance are in the same range as previous studies [47]. The difference can be the result of the Chumpan, Candelaria and Mamantel rivers which were not taken into account in other studies. As the actual flow through the tidal inlets was not measured, the model cannot be properly tested. Furthermore, the evaporation and precipitation are assumed to be constant over the lagoon, this might be not the case. Moreover, the groundwater flow calculation in subsection 4.1.5 is an approach. There is not a detailed geological investigation done with piezometer heights, fractures and weathering of the aquifer.
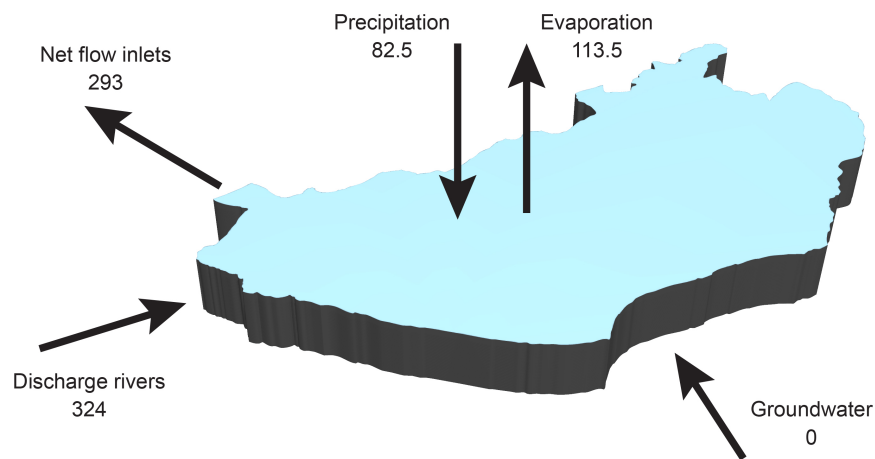
Figure 4.8: Mean water balance [m^3/s] of Terminos Lagoon

Figure 4.9 and 4.10 show that seasons are of significant influence on the water balance. In figure 4.9 the different terms are expressed in a percentage of the total seasonal in- and outflow of the water balance with the net flow of the inlets as unknown value. Both the rainy season and Nortes are comparable with the average yearly water balance. Relative influences of water balance components, between rainy season and Nortes, do not differ more than 5% from one another. Generally, the rainy season has the largest water fluxes. In contrast

to the rainy season and Nortes, the dry season shows a different distribution of the relative terms of the water balance. The evaporation during dry season is of relatively large influence on the water balance, although the net amount of evaporation is less than the rainy season. The net inlet flow of the dry season is low, as precipitation and discharge of the rivers are both relatively low compared to the yearly average situation. No data is available of the seasonal differences in groundwater flow.
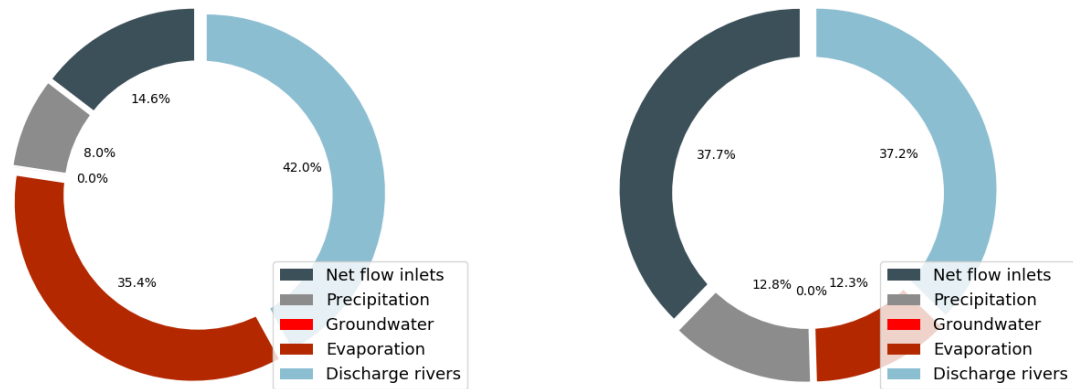
(a) Dry season

(b) Rainy season
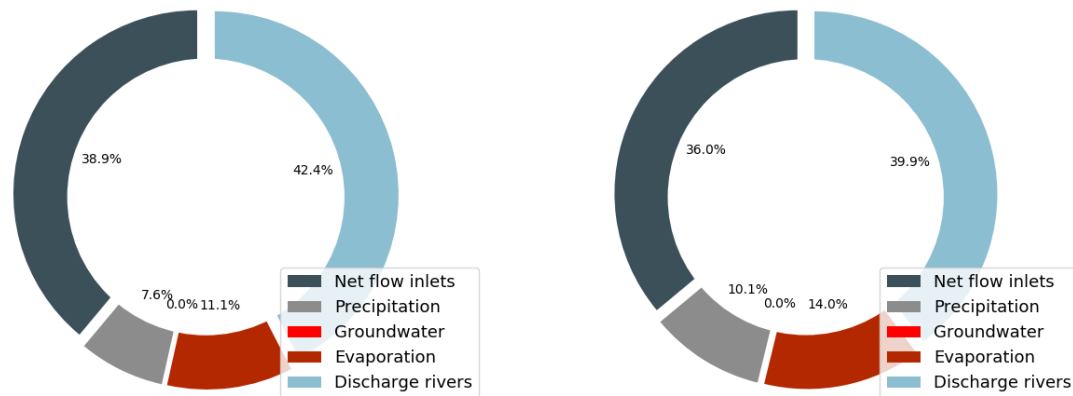
(c) Nortes season

(d) Annual mean values

Figure 4.9: Water balance charts for each season and mean situation
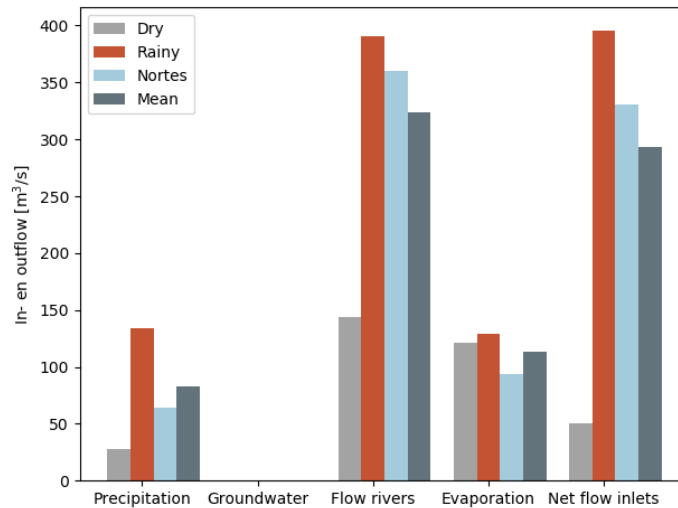
Figure 4.10: In- and outflow of Terminos Lagoon

4.2. Hydrodynamic processes

In this section first the tides and corresponding tidal climate are analysed. Secondly, the tidal inlet system is discussed, with the location of the tidal watershed and resulting tidal prisms. These parameters will later be used to investigate the stability of the tidal inlets. Thirdly the currents inside and outside the lagoon. Lastly the flushing time of the lagoon is discussed.

4.2.1. Tides

The water level variations due to the tidal forcing determines to a large extent the water in- and outflow of Terminos Lagoon. Tides are the result of gravitational attraction of the Sun and the Moon on the seas. They are composed of individual sinusoidal tidal harmonic components, which are called tidal constituents. Tidal constituents arise due to the changing position of the Earth relative to the Sun and Moon and the rotation of the Earth. Each tidal constituent has its own wave period and amplitude. The sum of the tidal constituents results in a unique local tidal signal. The amplitude of the tidal constituent determines the relative importance to the water level variations, for example the tidal constituents with the largest amplitude have the largest influence on the tidal climate. The tidal climate can be a diurnal tide, semi-diurnal tide, or a mix of both. A semi-diurnal tide means that two high waters and two low waters can be observed daily.

According to David (1998) [20], the tidal climate is mixed, mainly diurnal with a mean tidal range of 0.3 m in the Carmen inlet. In the Puerto Real inlet and the basin, the tidal climate is mixed mainly semidiurnal. These tidal ranges are based on two months of data. Another paper, written by Esparza [23], uses one year of data and found that the tidal patterns vary from mixed mainly diurnal in the tidal inlets of the lagoon, to diurnal inside the lagoon. ICML has a larger data set of the water pressure available, with approximately two years of data. This makes it possible to perform a new calculation of the tidal climate.

At the observation stations E.Pargo and SEMAR, locations indicated in figure 3.1, the water pressure (p) is measured. This pressure is converted to a water height by correcting it for the atmospheric pressure and using equation 4.4. In the calculation the assumption is made that the density is constant at 1025 kg/m^3 and the gravitational constant is 9.8 m^2/s.

$$h = \frac{p}{\rho \cdot g} \tag{4.4}$$

With:

p	= water pressure	[kPa]
ρ	= density of water (1025 kg/m^3)	[kg/m^3]
g	= gravitational acceleration (9.8 m/s^2)	[m/s^2]
h	= water height	[m]

With the known water level variations the tidal constituents are determined using two methods: the tidal fit toolbox of MATLAB and a Fast Fourier Transformation (FFT). The tidal fit toolbox of MATLAB returns the tidal constituents after loading the data file of the water level into MATLAB. FFT does not return the tidal constituents directly. The periods of tidal constituents are constant and known, as they are predicted using the orbits of the Sun and Moon. These periods are turned into frequencies. Based on the water level variations a signal is created by the FFT. After the FFT the signal is turned into a plot with frequency and amplitudes. The largest amplitudes can be distinguished, and the corresponding frequency can be found. Thereafter the frequency of the largest amplitudes is compared to the frequency of the tidal constituents. In this way the tidal constituents with the largest tidal amplitudes are found.

Table 4.5: Tidal constituents based on method and observatory

	E.Pargo		SEMAR	
Order	FFT	MATLAB Toolbox	FFT	MATLAB Toolbox
1	O1	K1	K1	O1
2	K1	O1	O1	K1
3	M2	S1	M2	M2
4	S1	M2	S1	P1
5	Q1	P1	Q1	Q1
6	N2	SSA	N2	N2

Table 4.5 gives the results of the Matlab Toolbox and FFT using water pressure measurements at observatories E.Pargo and SEMAR. Only the six tidal constituents with the largest amplitudes are shown. In appendix M, more tidal constituents of the MATLAB toolbox can be found and the entire signal of the FFT. Although the results of both methods are not exactly similar, the results are comparable. The diurnal constituents O1 and K1 are dominant.

The tidal climate can be classified by the factor F, which indicates the ratio between the diurnal and semi-diurnal tidal constituents. The value for F is calculated with formula 4.5 [15]. Table 4.6 gives information to interpret the results.

$$F = \frac{K1 + O1}{M2 + S2} \tag{4.5}$$

With:

$K1$	= amplitude of the lunar-solar declinational diurnal constituent	[m]
$O1$	= amplitude of the principal lunar diurnal constituent	[m]
$M2$	= amplitude of the principal lunar semidiurnal constituent	[m]
$S2$	= amplitude of the principal solar semidiurnal constituent	[m]

Table 4.6: Classification of tides with F as the ratio between the diurnal and semidiurnal tidal constituents and the corresponding category

F	Category
< 0.25	Semidiurnal
0.25 - 1.5	Mixed mainly semidiurnal
1.5 - 3.0	Mixed mainly diurnal
>3.0	Diurnal

Implementation of the results of the Matlab Toolbox and FFT leads to values of factor F shown in table 4.7. Based on the classification categories in table 4.6 it can be concluded that both methods give the same classification of the tides per observatory. At observatory E.Pargo the tide can be classified as diurnal and at observatory SEMAR as mixed mainly diurnal. In general the tide evolves from mixed mainly diurnal to mainly diurnal when it propagates further in the lagoon from SEMAR to E.Pargo measurement stations.

Table 4.7: F value E.Pargo and SEMAR by toolbox and FFT

	E.Pargo	SEMAR
MATLAB toolbox	3.4	2.4
Fast Fourier Transformation	3.6	1.6

4.2.2. Tidal inlet system

Terminos Lagoon is part of a tidal inlet system, which refers to the combined system of inlet, basin and ebb-tidal delta. The inlet is part of the tidal inlet system and refers to the connection between the sea and the lagoon. Terminos Lagoon has three connections to the Gulf of Mexico, from west to east: the Carmen inlet, the Puerto Real inlet and Sabancuy inlet. The Sabancuy inlet will be neglected, as described in the scope of the area, see subsection 2.1. Therefore, the tidal inlet system of Terminos Lagoon can be considered as a double inlet system. A double inlet system implies that the basins of the two inlets are not separated by land boundaries, they are separated by a watershed.

Tidal watershed

Due to the water surface elevation of the tide, there is an inflow and outflow of water between the sea and the lagoon. The volume of water, that enters the lagoon between mean low tide and mean high tide, is known as the tidal prism. The tidal prism influences processes with respect to the morphology and water quality. If a lagoon has multiple inlets, the situation becomes more complex. The tidal wave propagates through different inlets and will meet somewhere behind the barrier island. As a result the flow velocities at this location will be minimal, as well as the water exchange.

In case of Terminos Lagoon, the basin can be divided into two individual parts. A schematic overview of the lagoon is given in figure 4.11. One basin $A_{b,1}$ that receives water from the Carmen inlet and one basin $A_{b,2}$ that receives water from the Puerto Real inlet. The division line, which separates them, is called the tidal watershed. Two types of tidal watersheds can be distinguished: the hydraulic tidal watershed and the morphological tidal watershed. The hydraulic tidal watershed is the place in the basin where the standard deviation of the depth averaged flow velocity is minimal [68]. Due to the low flow velocities at the hydraulic watershed, the suspended particles in the water are able to settle, resulting in an elevation of the bed level compared to the surrounding bed. This is called the morphological watershed. In a state of equilibrium the hydraulic- and morphological watershed are at the same location. In a non-equilibrium state the morphological watershed follows the hydraulic watershed with some delay [68]. The location of the tidal watershed is mandatory for determining the tidal prism of the individual inlets, which subsequently influences the stability of these inlets.
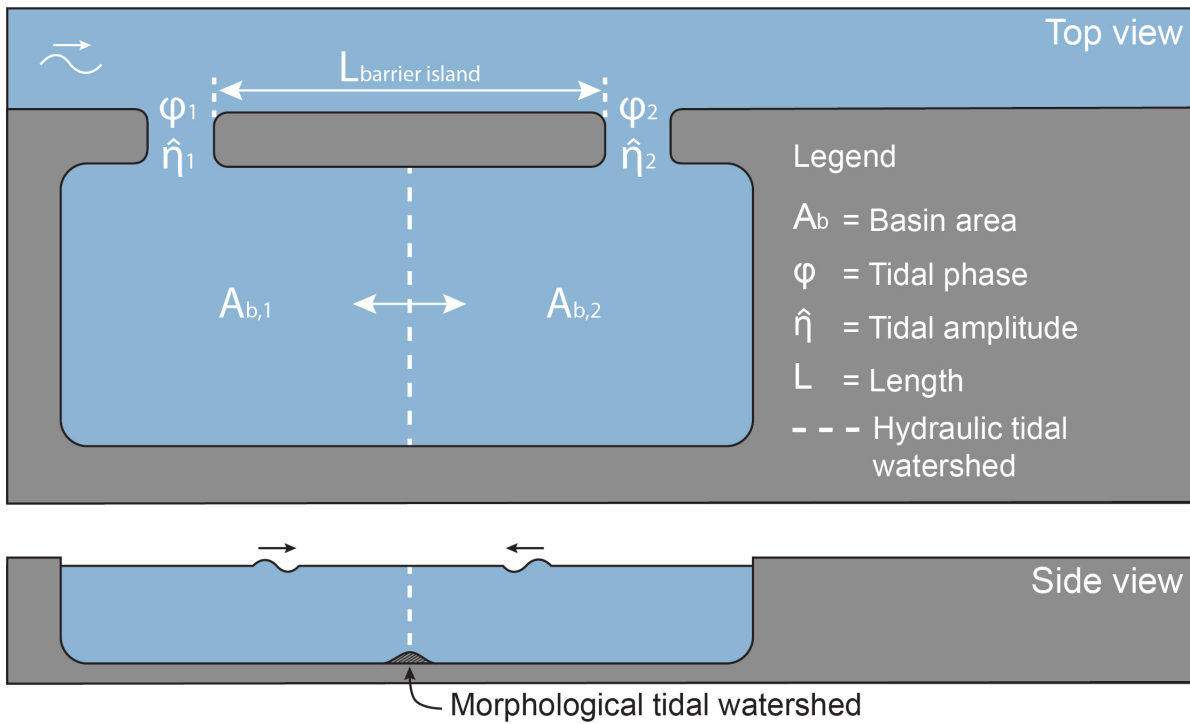
Figure 4.11: Schematic overview of tidal watershed in a double inlet system

The following theory on the location of the watershed is based on Vroom (2018). The location of the tidal watershed is predominantly determined by four parameters:

- The amplitude ratio of the tidal waves entering the lagoon.

$$a = \frac{\hat{\eta}_1}{\hat{\eta}_2} \tag{4.6}$$

- The phase difference of the tidal waves entering the lagoon.

$$\varphi = |\varphi_1 - \varphi_2| \tag{4.7}$$

- The relative channel length (ratio between length of the barrier island and tidal wavelength, with wavenumber indicated by k).

$$\frac{2\pi}{L_{tidal\,wave}} \cdot L_{barrier\,island} = k \cdot L_{barrier\,island} \tag{4.8}$$

- The bottom friction (σ).

Different scenarios can be described considering the idealized case of a channel in which two tidal waves propagate in opposite direction. A requirement for a tidal watershed to exist is that it need to be located in the realistic domain. The realistic domain is defined between $0 < x < L_{barrier\,island}$, in other words the watershed must be located in between the tidal inlets.

In the situation with an amplitude ratio of a=1, the watershed is located in the middle of the barrier island as long as the phase difference (φ) is smaller than the relative channel length. Otherwise there will be no tidal watershed. The phase difference only determines the magnitude of the flow velocities at the watershed, as long as the requirement $\varphi < kL_{barrier\,island}$ is valid. The larger the phase difference, the larger the flow velocities. In the situation in which the amplitude ratio a≠1, the watershed is shifted in the direction of the inlet with the largest tidal amplitude.

The magnitude of the amplitude ratio has impact on the influence of the phase difference, meaning that for a larger ratio the existence of a tidal watershed is less certain: there are stricter conditions for φ. On

the other hand, a larger relative channel length provides less severe conditions for the phase difference (φ) and amplitude ratio (a) in order to have a tidal watershed. The situation becomes more complex when considering the bottom friction. Bottom friction increases the influence of the phase difference and decreases the influence of the wave amplitude. Therefore, the tidal watershed will shift in the direction of the inlet where the wave enters last. However, if the friction becomes higher, the shifting effect is counteracted, as the wave length decreases and therefore the relative phase difference is smaller. Terminos Lagoon is a relatively shallow lagoon with a mean depth of approximately 2.6 m (section 2.4). The bottom friction can thus be expected to be of significant influence on the tidal wave propagation and therefore on the location of the watershed.

Previous research about the tidal current in the southern shelf of the Bay of Campeche indicated an amphidromic point in front of the coast of the Yucatan Pelinsula [51]. This is shown in figure 4.12. An amphidromic point is a location in sea where the tidal range is equal to zero. Due to Coriolis, the tidal wave spins around the amphidromic point. In the Northern Hemisphere this is directed in counterclockwise direction. This implies that the tidal wave arrives first at the Carmen inlet and propagates in the direction of the Puerto Real inlet. In figure 4.12 the dashed line shows the amplitude of the M2-tide and the solid line shows the phase difference in degrees. Based on this figure, the phase difference of the tidal wave arriving at the two inlets is estimated at 7.5 °, which corresponds to half an hour.
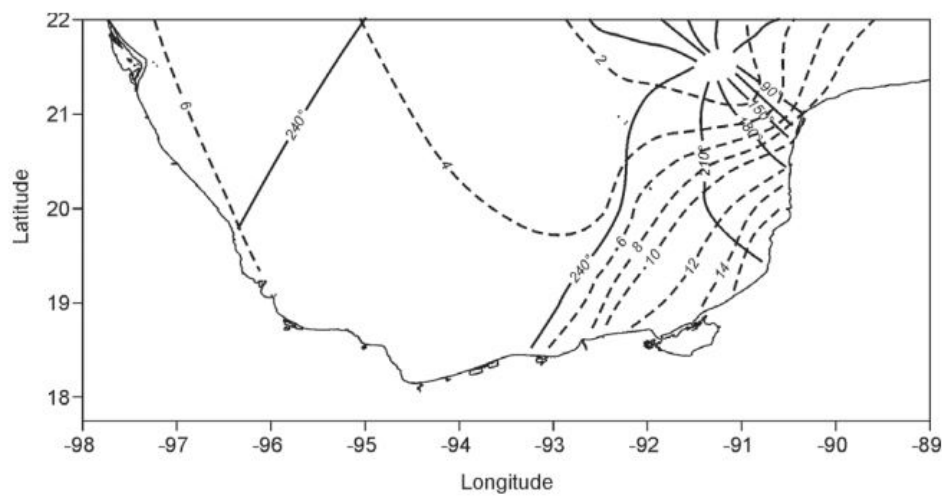
Figure 4.12: Tidal phase difference (solid line) and tidal amplitude (dashed line) map in the Gulf of Mexico [51]

The available water pressure data (section 3.1) only allows to investigate the tidal amplitude at the Carmen inlet. There are no measurements of the Puerto Real inlet available. Therefore, the amplitude ratio is determined based on the research by L.T. David and B. Kjerfve (1998), who defined a tidal amplitude in the Carmen inlet of 0.31 m and in the Puerto Real inlet 0.34 m [20]. Based on these results, the location of the tidal watershed will be located closer to the Puerto Real inlet. Bottom friction is expected to be of significant influence, meaning the phase difference influences the location of the tidal watershed. Due to the decreasing wavelength and wave celerity, the location of the tidal watershed would be shifted towards the Carmen inlet. The net result of both the amplitude ratio as well as the bottom friction would be a tidal watershed located somewhere around the middle of the barrier island.

This hypothesis is tested using the Delft3D-FLOW model. The model which only includes tides is used. As described before, the hydraulic tidal watershed can be found at the location where the standard deviation of the depth averaged flow velocity is minimal [68]. The standard deviation of the depth averaged flow velocity is shown in figure 4.13. The white line shows the location of the tidal watershed based on the model results. This allows to determine the surface area of both basins and accordingly the tidal prisms using the tidal range. The tidal watershed divides the lagoon in a western and an eastern part, respectively 871 km^2 and 816 km^2. The tidal range is based on the water level measurements at SEMAR, see section 3.1. From figure M.1a the tidal range is determined to be approximately 40 cm. The tidal prism is calculated with the formulas in appendix I and is 256.5·10^6 m^3 for the Carmen inlet and 278.4·10^6 m^3 for the Puerto Real inlet. These volumes will later be used in the calculation of the stability of the tidal inlets (subsection 6.2).
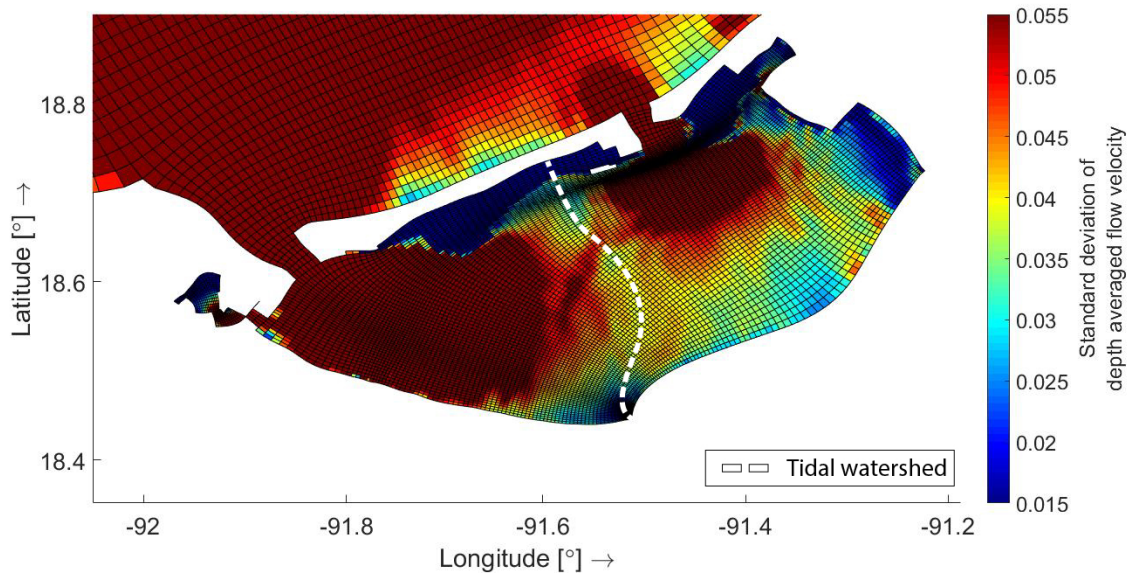
Figure 4.13: Location of tidal watershed within Terminos Lagoon, white areas are land

4.2.3. Currents

Currents may occur due to wind, tides, waves and density differences. As a result of different types of forcing, changes in the vertical velocity profile and direction of the currents occur. The currents are responsible for, among others, the distribution of heat, sediments, salt and oxygen through the lagoon. Three different kinds of currents are distinguished in the lagoon: wind-driven currents, tide driven currents and density driven currents. These currents, together with the inflow of the Palizada river, result in a residual current. Using the Delft3D-FLOW model, the depth averaged velocities are calculated. Accordingly the residual current is determined. Figure 4.16 shows the residual currents for the different seasons. Outside the lagoon the wave driven currents are considered, which are important to analyse the sediment transport of the adjacent coastline.

Wind-driven currents

The wind causes a shear stress on the water surface causing the water column to move in the same direction as the wind. The friction can be determined with the quadratic friction law, shown in equation 4.9. Because of the quadratic term in this law, a doubling of the wind velocity, results in a quadrupling of the current velocities. During strong wind events, the wind currents can be significantly higher than the current velocities due to tides. Furthermore the velocity profiles of wind- and tide driven currents are different. Figure 4.14 gives a representation of both currents over the water column.
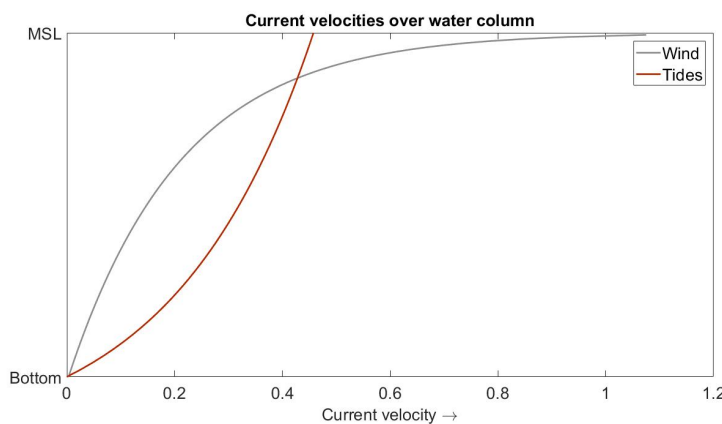
Figure 4.14: Schematic distribution of wind-driven and the tidal current over the depth of the water column

$$\tau_{wind} = C_d \cdot \rho_a \cdot W^2 \tag{4.9}$$

With:

τ_{wind}	= wind shear stress	[kg/m/s^2]
C_d	= drag coefficient of the wind	[-]
ρ_d	= density of air	[kg/m^3]
W	= wind velocity	[m/s]

For a wind driven current to develop, it takes hours and a fetch of tens of kilometers. Terminos Lagoon has two prevailing wind directions with strong winds ("Wind" in section 4.1.2). Terminos Lagoon has a long fetch, and therefore wind is likely to be an important driver for the currents in the basin.

Density driven currents

Fluids with differences in density may drive currents. These differences in density may arise because of temperature differences and/or differences in salinity. Water temperature and salinity of the water in Terminos Lagoon can differ locally. In figure 5.5 in section 5.1 the spatial distribution of salinity is given. The differences in salinity between the freshwater of the Palizada river and the water of the lagoon results in local density differences in the water column (appendix J). Furthermore, there might be temperature differences between water from the lagoon, rivers and sea. If there is a clear distinction between high and low values for these parameters, there is a large gradient which is called a thermocline for temperature (figure 4.15a) or a halocline for salinity (figure 4.15b). The difference in density results in pressure differences spatially, which causes a flow from high pressure to low pressure.

(a) Thermocline   (b) Halocline
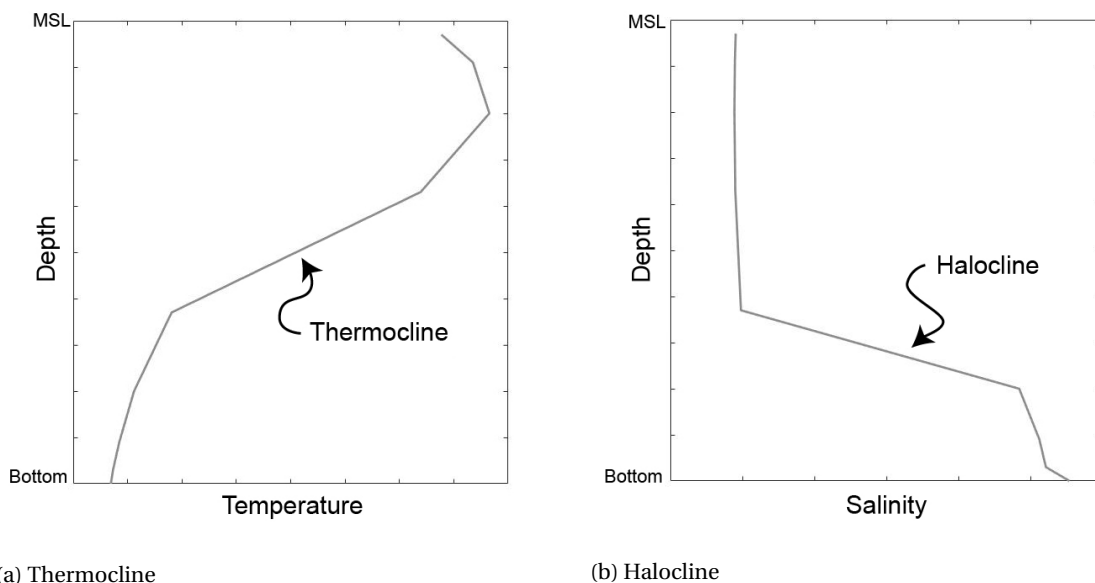
Figure 4.15: Schematic diagram of thermocline and halocline, the shape is based on measurements of Estacion 5 (appendix F.2)

Tide driven currents

Tides can be divided in a vertical tide and a horizontal tide. The vertical tide is the rise or fall of the water surface. The horizontal tide is the direction of the flow, also called the tidal current. The direction of the horizontal tide determines if the current is a flood tidal current or an ebb tidal current. The velocity of the flood tidal current is in the same direction as the flood propagates. The ebb tidal current is in opposite direction. Usually the vertical- and horizontal tide do not occur simultaneously. There can be a phase difference in which the horizontal tide leads the vertical tide. The occurrence of this phase difference depends on friction and (partial) reflections in the basin. Due to the shallowness of Terminos Lagoon, bottom friction plays an important role in the propagation of the tides, causing the flow velocity to lead the surface elevation. If friction is dominant over inertia, the phase difference will be between 0 and 45 °[14]. To simplify the horizontal

tide the assumption is made that the phase difference between vertical tide and horizontal tide has a maximum of 45 °, as the lagoon is shallow and friction is expected to be dominant. This assumption is later used in the figures with thermal imagery in subsection 5.2.

Wave driven currents

The propagation of waves results in a mass and momentum flux in wave propagating direction. Because of continuity this mass transport generates a return current in the shoreface, outside the lagoon, as the water does not pile up against the coast. This is called the undertow. There is a net onshore directed transport of water between the wave crest and the wave through. The undertow is the return current that is offshore directed and takes place in the lower part of the water column. In the situation in which the waves approach the coastline under an angle, an alongshore current is generated. The direction of the alongshore current depends on the angle of approach of the waves.

Residual currents

The combination of the before mentioned currents over a certain time period translates into a residual current. In figure 4.16 the residual currents of the different seasons are presented. The vectors in grey show the velocity and direction of the flow at their position. In red the main residual current is shown. These figures are based on the Delft3D-FLOW model including tides, wind and the Palizada river.

(a) Dry season

(b) Rainy season

(c) Nortes season
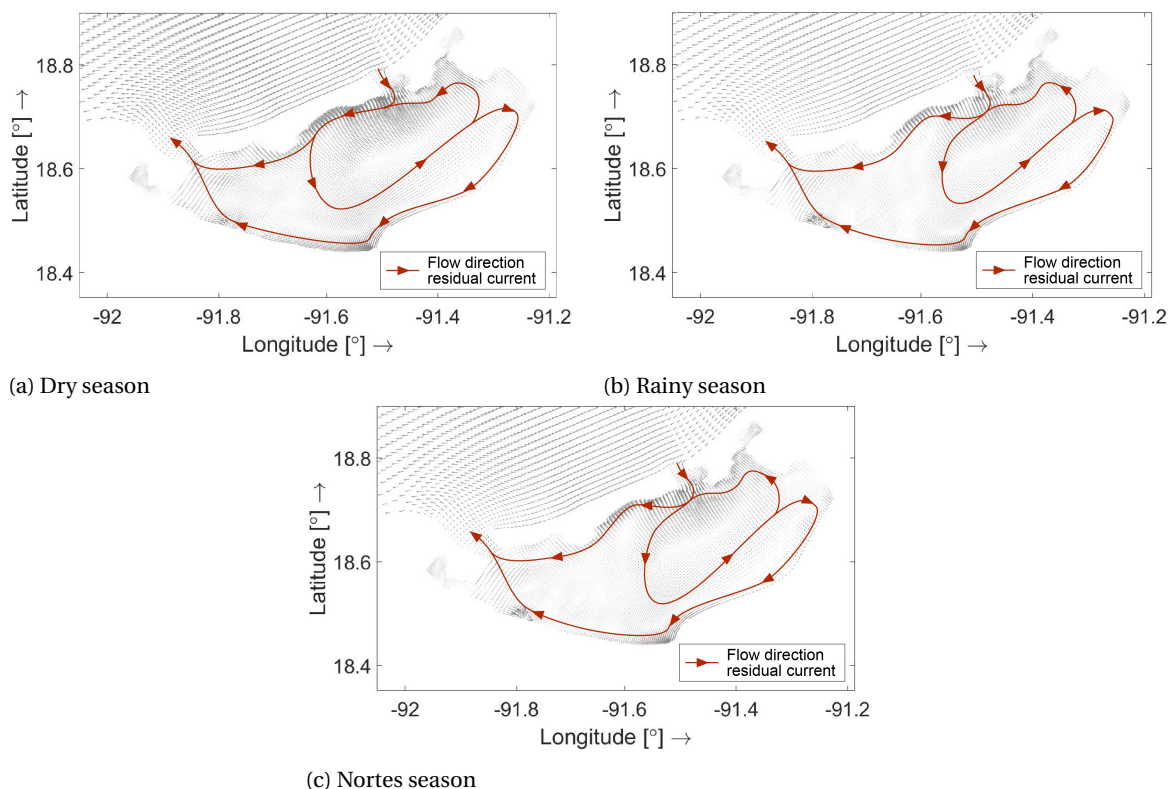
Figure 4.16: Residual currents in Terminos Lagoon

The results in figure 4.16 show that the residual current of Terminos Lagoon is directed from the Puerto Real inlet to the Carmen inlet. Another distinct feature is the circulating current in the eastern part of the lagoon. During the dry season, the size of the circulating pattern increases and includes more of the northern and western parts of the lagoon than during Nortes and the rainy season. The effect of the seasons on the inflow of the Palizada river is also notable. During the dry season the residual current shows lower flow velocities than during rainy season and Nortes, which is probably due to lower discharge rates during this season, see table 4.4. The flow pattern exposes a current from east to west along the edges of the lagoon. Besides all these flows, there are some areas which show no residual motion. It seems there are more places without residual motion during the Nortes and the rainy season than during the dry season. Overall the lagoon can be roughly

split into two parts based on the modelled current patterns: the east part, with the current circulation, and the west part, with the currents along the edges and the Palizada river input.

The residual current direction is determined by the Delft3D-FLOW model. A limitation of this model is that it gives an approximation of the situation. To make sure the model returns reliable predictions the model should be calibrated using field measurements. To compare the residual current of the model and the residual current in the field, Eulerian measurements in the field are needed. Also the other parameters that drive the residual current (wind speed, the tidal constituents and the river inflow) should be verified. For these parameters there are already measurements taken. To further increase the reliability of the model the inflow of the Chumpan river, Candelaria river and Mamantel river should be included in the model. Also the wave climate is not included in the model. There are no measurement of the wave climate close the to Terminos Lagoon, so this would be hard to add to the model and calibrate. A verification of the model will increase the reliability of the model. Moreover, some input values of the Delft3D-model are assumed to be constant. For example the bottom friction will change in space and the position of the landboundaries may change in time.

4.2.4. Flushing time

According to Monson et al. (2002) [40], the flushing time is defined as a parameter describing the water body exchange characteristics without distinguishing underlying physical processes or any spatial distribution. A large flushing time can contribute to high pollution levels in the lagoon, as substances cannot flow out of the lagoon. Within this study, different flow rates are employed for the flushing time estimate based on the tidal prism, the river discharge, and the different seasons (dry, wet, Nortes). The calculation of the flushing time is elaborated in appendix L. As the tidal flow factor (b) is unknown, a sensitivity analysis is performed. The tidal flow factor is the fraction of effluent water that is returning to the lagoon each flood tide. This factor b varies between 0 and 1, respectively the ratio where the entire tidal prism volume contributes to the water exchange and the ratio where the tidal flow does not renew the water in the lagoon. Results are shown below in table 4.8. Figure 4.17 shows the mean flushing time in days, where factor b varies between 0 and 1.

Table 4.8: Flushing time per season

Season	Flushing time for ratio b [days]				
	0.0	0.25	0.5	0.75	1.0
Dry	8.12	10.74	15.86	30.34	348.75
Rainy	7.80	10.20	14.71	26.40	128.44
Nortes	7.84	10.26	14.85	26.84	139.50
Annual	*7.87*	*10.34*	*15.01*	*27.37*	*155.00*
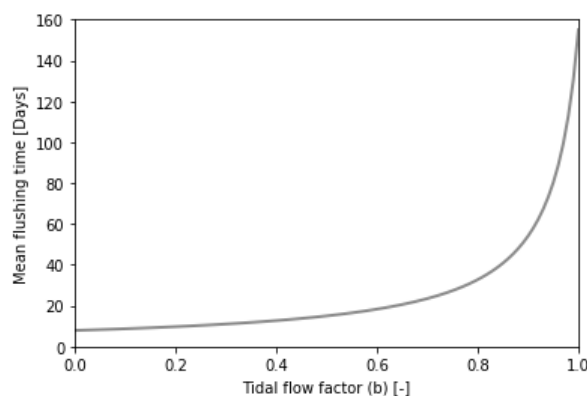
Figure 4.17: Mean flushing time for different ratio of b [days]

In Terminos Lagoon the yearly average flushing time ranges between 8 and 155 days, for a tidal flow factor of 0 and 1 respectively, see figure 4.17. As this wide range is not an informative result, research should be conducted into the returning flow at the tidal inlets in order to precisely define the flushing time of the lagoon. Furthermore, it is be found that the flushing time varies over the seasons due to the difference in river

discharge. The larger the factor of tidal returning flow, the more the seasonal difference will become.

4.3. Spatial characteristics

In this section, different spatial characteristics are touched on. Salinity, water temperature and dissolved oxygen data, measured at SEMAR and E.Pargo, are visualised. Sediments near Terminos Lagoon are presented. Explained is the use of remote-sensed data products to obtain measures of temperature and Secchi depth.

4.3.1. Salinity

Water salinity is measured during the field measurement campaigns and at the stationary observatories of E.Pargo and SEMAR. At the observatory stations, see figure 3.1, the salinity is not measured directly. The salinity is expressed in practical salinity unit, PSU, which is a unit based on the properties of sea water. The practical salinity unit is the salt concentration in g/kg. Based on the measured conductivity and temperature at these locations, the salinity can be derived. This derivation is done following the example of Foffonof and Millard [24]. The calculation is elaborated in appendix K.

The salinity at both stations is plotted in figure 4.18 and 4.19. The data sets of the observatory SEMAR and E.Pargo have a duration of respectively 22 and 16 months. Both data sets show gaps, especially the data set of observatory E.Pargo. It has a large gap from April to October 2017. The reason for these gaps is unknown. Although data is missing, visualisation seems to confirm that SEMAR and E.Pargo show a similar deviation in the box plot. The data set of observatory SEMAR is missing data in the month September and has limited data available in the month August. From the SEMAR data, seasonal variability can be observed. In the period October to February, which is a part of the Nortes season, the deviation of salinity is large, while the salinity is almost constant in April, which is part of the dry season. The large deviation in salinity could be explained by the strong wind events during the Nortes season. A clear pattern can be observed in the median of the salinity. The maximum monthly median salinity is measured in the month April, which is part of the dry season. This could be explained as a result of the reduced fresh water inflow of the rivers, see the discharge rates in table 4.4, which in turn are a result of the lower precipitation rates, see figure 4.1.
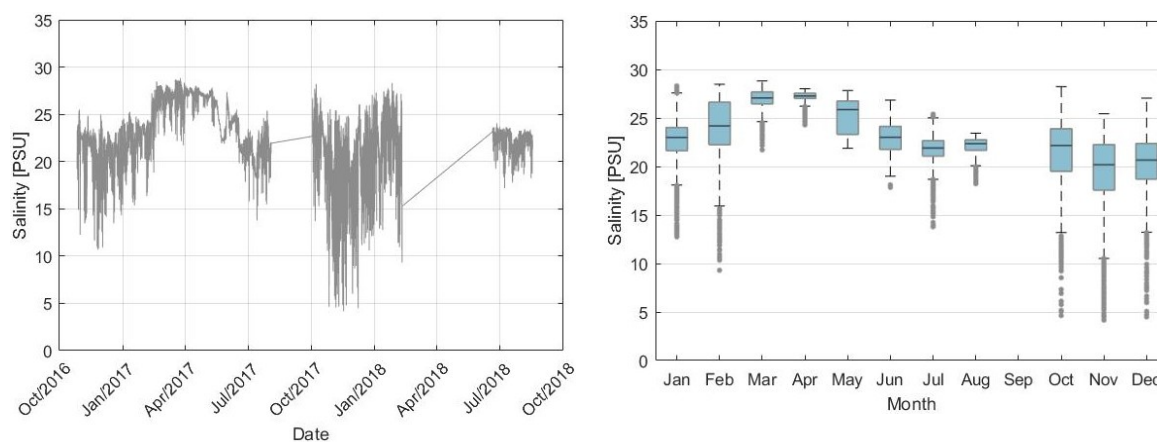
(a) Salinity at observatory SEMAR

(b) Box plot of the salinity at observatory SEMAR, see appendix G for box plot features

Figure 4.18: Salinity of the water in Terminos Lagoon, measured at the observatory Semar, hourly averages from October 2016 - August 2018
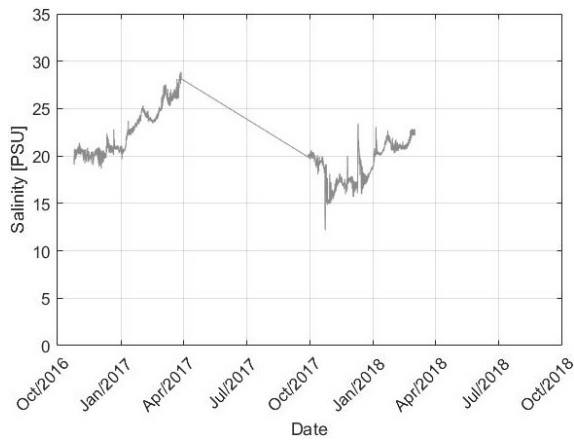
(a) Salinity at observatory E.Pargo
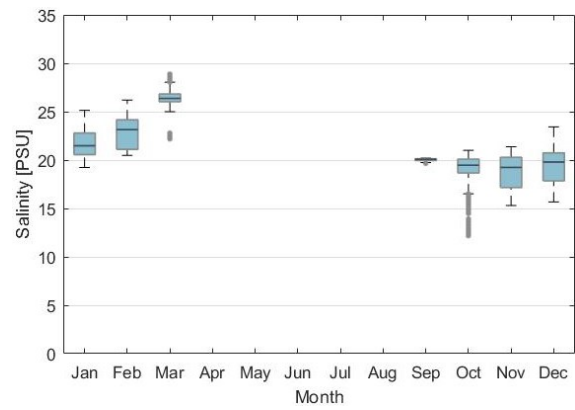
(b) Box plot of the salinity at observatory E.Pargo see appendix G for box plot features

Figure 4.19: Salinity of the water in Terminos Lagoon, measured at observatory E.Pargo hourly averages from October 2016 - March 2018

4.3.2. Water temperature

Temperature of water is measured at depth during the field measurement campaigns and at fixed height at the observatory stations. Spatial variation of surface water temperature per season is investigated using satellite imagery. The water temperature at the observatory station SEMAR has a yearly fluctuation between a minimum temperature of 22.6 °C, in January, and a maximum temperature of 34.6 °C in August. During the dry season an increase in atmospheric temperature is observed, while during the Nortes season the atmospheric temperature is decreasing. On a daily basis the water temperature fluctuates with 1 to 3 °C. The range of daily fluctuation in temperature are smaller for water, compared to air. This is intuitive; water warms and cools slower than air. The fluctuations in the water temperature are related to the fluctuations in the atmospheric temperature. The water temperature, however, reaches its daily maximum on average 2.5 hours later than the atmospheric temperature. In other words, there is a lag between the water temperature and atmospheric temperature. These findings are depicted in figures 4.20 and 4.21.
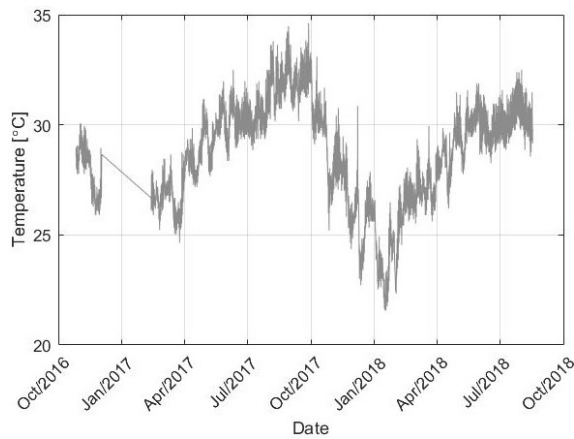
(a) Water temperature at observatory SEMAR
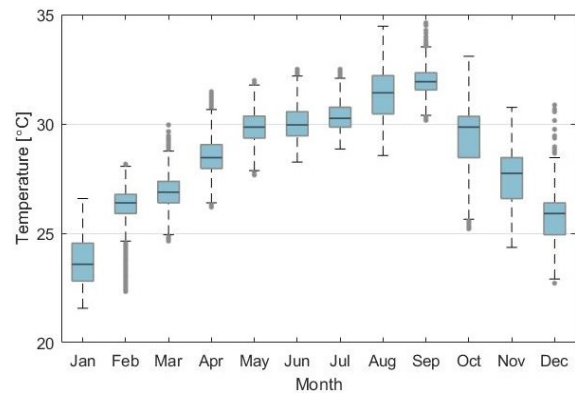
(b) Box plot of the water temperature at observatory SEMAR, see appendix G for box plot features

Figure 4.20: Water temperature, measured at observatory SEMAR, hourly averages from October 2016 - August 2018
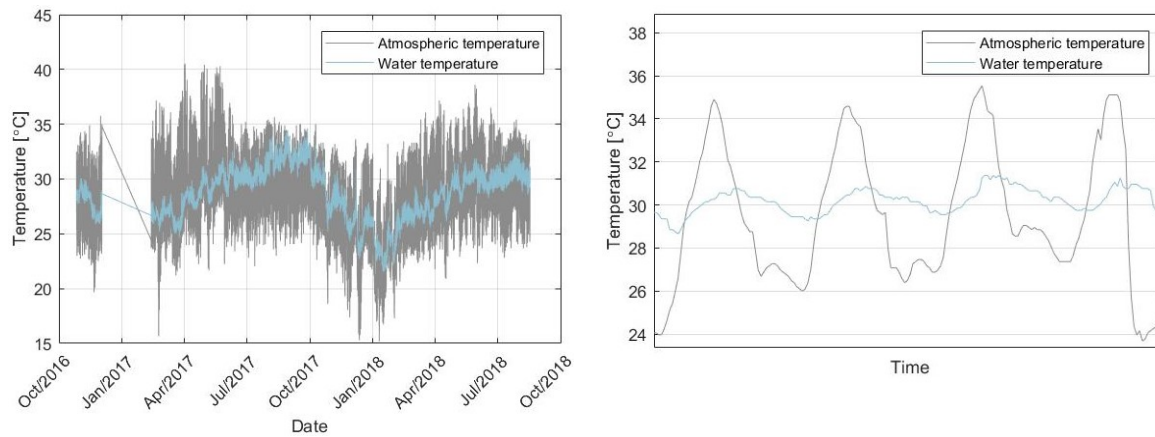
(a) Water temperature and atmospheric temperature at observatory SEMAR

(b) Phase shift between water temperature and atmospheric temperature at observatory SEMAR

Figure 4.21: Water temperature and atmospheric temperature, measured at observatory SEMAR, hourly averages from October 2016 - August 2018

Temperature fluctuations in space and between seasons are looked at using satellite imagery. Landsat 8 has two distinct thermal bands in the infra-red spectrum, which can be used to easily obtain top of atmosphere brightness temperature [5, 34]. This temperature can then be used as reference material. It is, however, atmosphere uncorrected. As in-situ measurements and temperatures as calculated using Landsat images differ, the temperature maps resulting from processing Landsat imagery will not be used as direct temperature measurements. They can, however, be used to look into the spatial patterns of temperature within and near the Terminos Lagoon. Extracting temperature from the Landsat imagery is done as follows.

The Digital Numbers (DN) provided by the raw data are first converted to at-sensor spectral radiance using equation 4.10:

$$L_\lambda = ML \cdot Q + AL \tag{4.10}$$

With:

L_λ	= spectral radiance	[W/(m$^2\cdot$ sr $\cdot\mu$m)]
ML	= radiance multiplicative scaling factor for the band	[-]
AL	= radiance additive scaling factor for the band	[-]
Q	= pixel value	[DN]

Band 10 is used as thermal band. Now the atmosphere uncorrected surface temperature can be determined using equation 4.11:

$$T = \frac{K_2}{Ln(\frac{K_1}{L_\lambda+1})} - 273.15 \tag{4.11}$$

With:

T	= top of atmosphere brightness temperature	[°C]
L_λ	= spectral radiance	[W/(m$^2\cdot$ sr $\cdot\mu$m)]
K_1	= thermal conversion constant for the band	[-]
K_2	= thermal conversion constant for the band	[-]

All necessary constants are provided in the meta file, included with the data. A total of five images per season are collected, one for every year since 2014. Tides for each acquisition are determined using the tidal signal found in subsection 4.2.1. Following this, top of atmosphere brightness temperature pattern in the lagoon is compared per season.

4.3.3. Dissolved oxygen

Dissolved oxygen (DO), is a water quality parameter that is important for aquatic life [2]. Different species need different amounts of dissolved oxygen. Roughly there are two groups, bottom feeders and shallow water fish. They need, respectively, minimum amounts of oxygen between 1-6 mg/L and 4-15 mg/L. In the northern Gulf of Mexico a concentration of dissolved oxygen less than 2 mg/L is considered to be the limit at which water can no longer support living aquatic organisms [41]. This is called hypoxia. Measurements of dissolved oxygen are performed at the observatory stations, E.Pargo and SEMAR, and during the field measurement campaigns.

Dissolved oxygen has different sources, as it can enter the water through air by diffusion, or by aeration via wind and via photosynthesis, where oxygen is produced as by-product. The process of photosynthesis causes daily variations of oxygen concentration. During the day the concentration of dissolved oxygen increases due to sunlight. This is in contrast to the night, where the amounts of dissolved oxygen are used in respiration by the organisms [2]. Therefore, the dissolved oxygen concentrations are higher during the day than at night. Furthermore, the concentrations at the SEMAR station are expected to be higher than concentrations of the E. Pargo station, as, in general, concentrations are higher in open water than in small channels. This is due to the fact that open water receives more oxygen via diffusion and wind.

Figure 4.22 shows the measured dissolved oxygen concentrations at SEMAR and E. Pargo respectively. The original SEMAR data is shifted by +0.69 in the period 26 October 2016 until 11 February 2017 and by +0.19 in the period 11 February 2017 until 4 August 2017, as measurements were not calibrated properly. By applying these offsets to the data, the minimal values are artificially set to zero. This has implications on the reliability of the dissolved oxygen levels. However, the fluctuations can still be analysed. In figures 4.23a and 4.23b small parts of the data are given to investigate the daily fluctuations. The red line in the plots indicates the hypoxia limit of 2 mg/L [41]. Dissolved oxygen concentrations below this limit occur for both the SEMAR and E.Pargo stations. Furthermore, concentrations at both stations vary over the length of the day. Remarkably the peaks in the concentrations occur mostly at night instead of midday. This is unexpected as photosynthesis is maximum in the daytime. Finally, it is expected that concentrations of dissolved oxygen at SEMAR are higher than at E.Pargo, as tidal and wind influences are higher at the SEMAR station. However, this can not be confirmed due to different measurement periods.

It can be found that these measurements of dissolved oxygen are erroneous, as measurements are incomplete and not in line with expectations. Therefore, dissolved oxygen measurements from the observatories SEMAR and E.Pargo are not further used within this research.
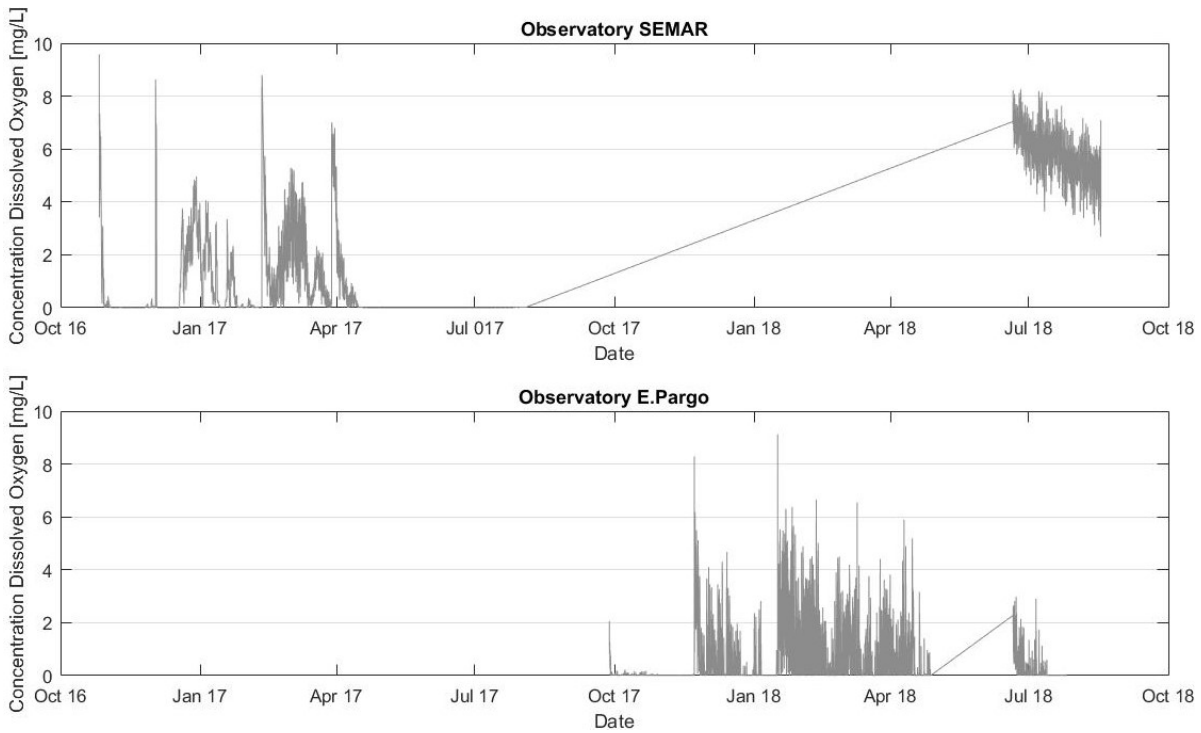
Figure 4.22: Dissolved oxygen in the water at observatories SEMAR and E.Pargo, hourly averages from October 2016 - August 2018
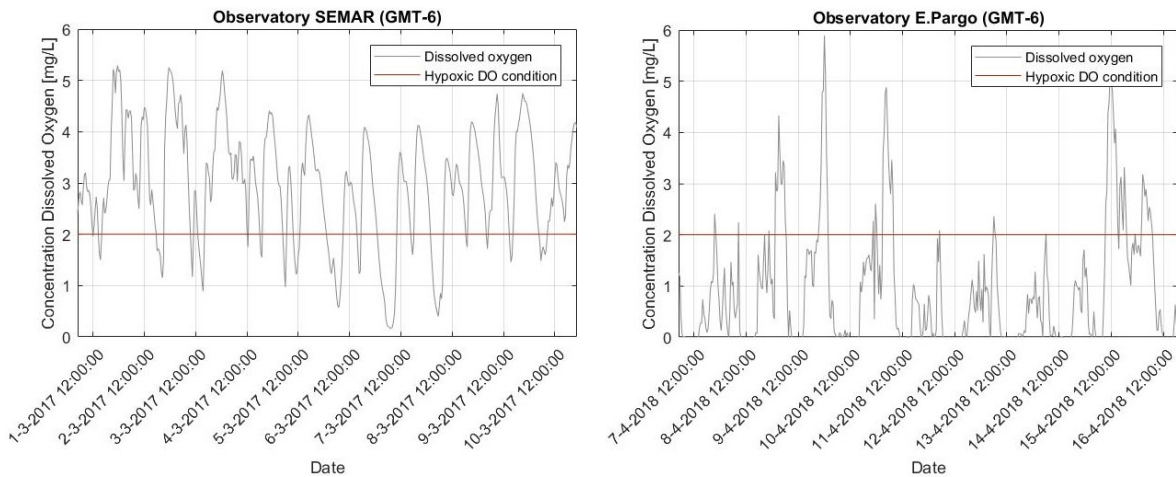
(a) Detail of the dissolved oxygen concentration at observatory SEMAR

(b) Detail of the dissolved oxygen concentration at observatory E.Pargo

Figure 4.23: Details of the measured dissolved oxygen concentration at observatories SEMAR and E.Pargo

4.3.4. Sediments

A literature study is conducted to find sediment distribution of Terminos Lagoon, as sediments distribution data are not available. In figure 4.24 a distribution of the sediments in Campeche Sound and Southern Mexico is given. The sediments at the bottom of the sea, located in front of Terminos Lagoon inlets, are mainly carbonate salty silt and carbonate mud. Mud is a mixture of material with a silt and clay size. Carbonate salty silt is possibly transported through the Puerto Real inlet and carbonate mud through the Carmen inlet.
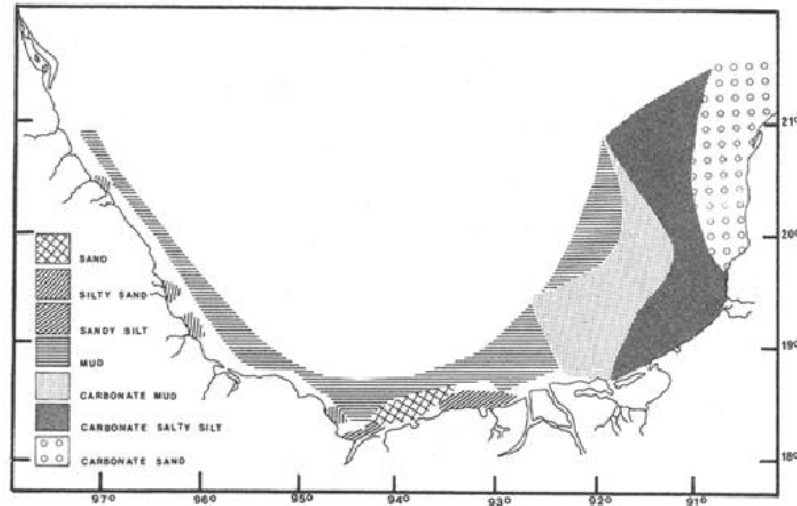
Figure 4.24: Sediment distribution in Campeche Sound and Southern Mexico, with the location in longitude and latitude [47]

4.3.5. Secchi depth

According to Lee et al. (2016) the transparency or water clarity is the first order description of the quality status of an aquatic environment [36]. It is a measure of depth from water surface level to the depth where one can still see into the water. Higher Secchi depths means clearer water. Lower Secchi depths means more turbid or colored water. The Secchi depth depends on day's conditions and the eyesight of the observer. Processes that are dependent on the underwater light field are biological, physical and chemical processes, like photosynthesis, sediment suspension and nutrient cycling respectively [10]. Secchi depth is measured during the fieldwork campaigns and by processing satellite imagery.

During fieldwork campaigns the transparency is measured by visual observation, the method is described in chapter 3.4. Secchi depth is also determined using Landsat 8 imagery, using a semi-analytical scheme [36, 48]. This methodology is chosen as it links remote-sensed measurements directly to Secchi depth. A Landsat 8 image of the 4 September 2018 is compared to the field campaign measurements of the 5 and 7 September 2018 for quality assessment of the chosen method, which is presented in appendix E. Secchi depth determination using remote-sensed imagery is deemed appropriate to look into spatial distribution of the parameter, though absolute values of these measurements cannot be guaranteed to be valid.

Secchi depth (Z_{sd}) through remote-sensed imagery is determined mainly using the following formula:

$$Z_{sd} = \frac{1}{2.5 Min(K_d^{tr})} ln(\frac{|0.14 - R_{rs}^{tr}|}{0.013}) \tag{4.12}$$

With:

K_d^{tr}	= Diffuse attenuation coefficient at the transparent window of the water body within the visible domain (410-665 nm wavelength)	[m^{-1}]
R_{rs}^{tr}	= Remote-sensing surface reflectance corresponding to this wavelength	[sr-1]

To obtain surface reflectance R_{rs}^{tr} from the Landsat 8 imagery, the Acolite algorithm is used, as detailed in Vanhellemont and Ruddick (2014) [66]. K_d^{tr} is derived using a mix of empirical and analytical formula's, which are described in appendix E. A total of five images per season are processed, similar to the ones used to look into thermal structure within the lagoon. Tides for each acquisition are determined using the tidal signal found in 4.2.1. Secchi depth in the lagoon is then compared per season.

4.4. Statistical dependence

In this section the correlations between the hydrological processes and spatial characteristics (salinity and water temperature) of the SEMAR data are presented. The Bayesian network of Terminos Lagoon is given,

subsequently the correlation matrix is shown. The purpose of the Bayesian network is to achieve a better understanding in the dependence of the individual parameters based on the available data. This information is used to draw conclusions about consequences of future developments. Lastly, the highest correlations will be investigated in detail by the application of semi-correlations.

The dependence between two variables, variables X and Y, can be quantified in different ways. Pearson's correlation coefficient (ρ_{XY}) is a measure to quantify the linearity between the variables X and Y [32]. The correlation coefficient can be positive, if X grows than Y grows, or negative, if X grows than Y decreases. The Pearson correlation coefficient is defined between -1 and 1. The values are defined as follows:

- X and Y are fully independent, ρ_{XY}=0;
- X and Y are perfectly dependent,ρ_{XY}= ± 1;
- X and Y are dependent, -1 < ρ_{XY} < 1.

The Spearman rank correlation is another measure to quantify the degree to which X and Y depend through a possibly non-linear but monotonic function of each other. This method ranks the original data of X and Y on the interval from 0 to 1, in contrast to Pearson. Based on these ranks the correlation coefficient is determined.

4.4.1. Bayesian network

A Bayesian network (BN) is a graphical model for representing multivariate probability distributions. The purpose of constructing a network is to model conditional dependence. Accordingly, one can conduct inference on the random variables.

A Bayesian network is build out of nodes, where each node represents an individual random variable such as the atmospheric temperature, and directed arcs, which represent dependence between two nodes. The arcs connect the nodes which are expected to have a dependence, for example the discharge is expected to have an influence on the salinity. The direction of the arc is essential, as discharge is expected to have an influence on the salinity, not vice versa.

In figure 4.25 the BN of Terminos Lagoon is shown. As not all data are available for the same time span, indicated by figure 3.2 in section 3.1, it is required to construct the Bayesian network with three different 'clusters'. Each cluster is a small Bayesian network with parameters recorded at the same time. The precipitation is recorded in cluster 1 (October 2016 - August 2018) as well as cluster 2 (April 1992 - November 2014), indicated as P and P2. As precipitation has a perfect positive correlation with itself (correlation of 1.0), this parameter is used to connect clusters 1 and 2. The same is true for the atmospheric temperature connecting clusters 1 and 3. The discharge and evaporation are expected to have an influence on the salinity. As these parameters have not been measured in the same period, their correlation is determined based on their monthly average values. This leads to 12 values which are used to compute the correlation.

The text on the arcs expresses the type of correlation. Some values indicate conditional rank correlations, which are the correlations between two nodes given other parameters. For instance Sal AT | P means the rank correlation between salinity and atmospheric temperature given the precipitation. This should not be confused with unconditional rank correlations which are given in the correlation matrix in table 4.9.
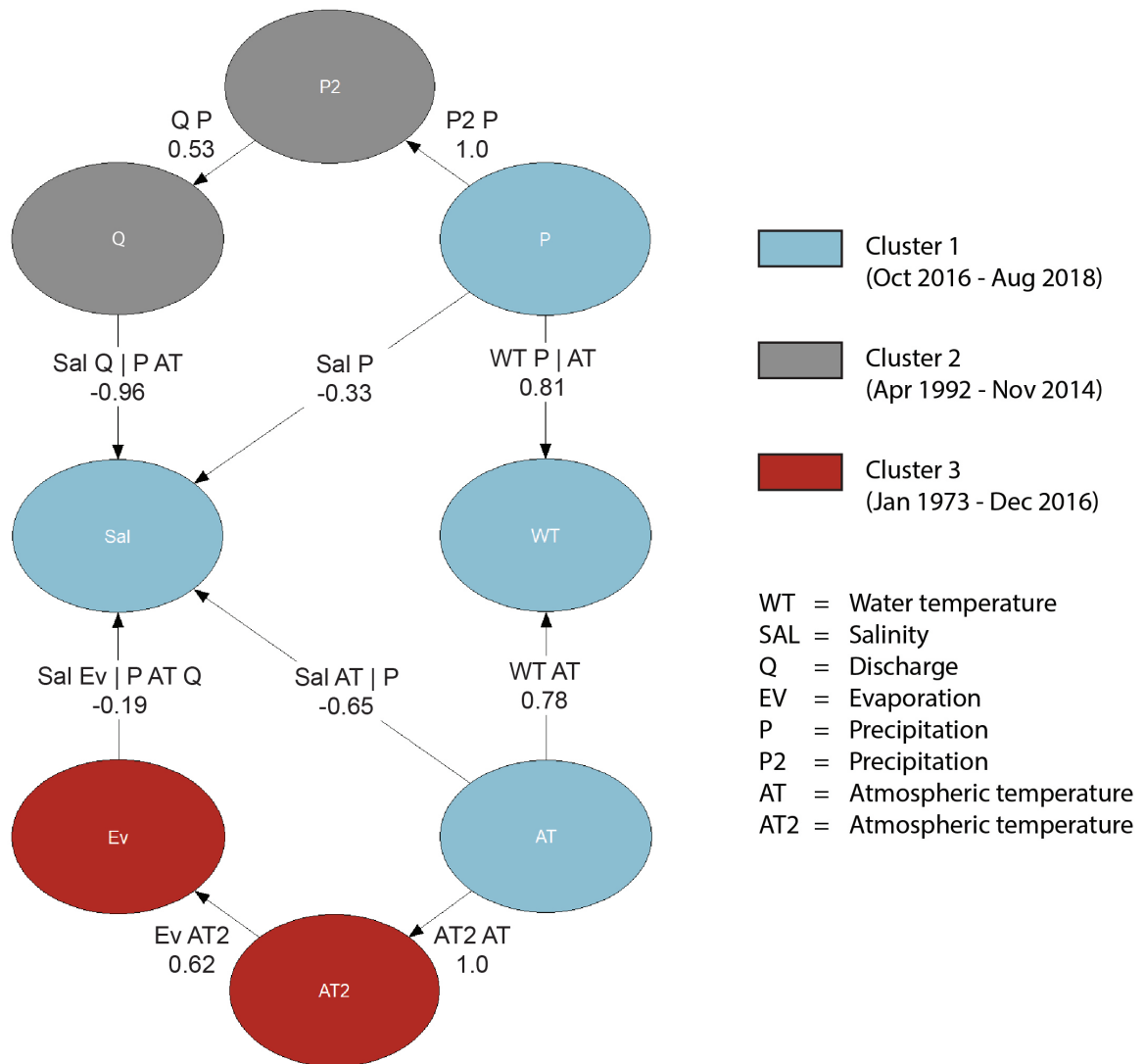
Figure 4.25: Bayesian network Terminos Lagoon

4.4.2. Correlation matrix

Uninet is used to obtain the correlation matrix. Uninet is a software package, which can couple random variables to a Bayesian network [8].

Table 4.9: Correlation matrix Terminos Lagoon (obtained using Uninet), with WT = Water temperature, AT = Atmospheric Temperature, P = Precipitation, Sal = Salinity, Ev = Evaporation, Q = Discharge

	WT	AT	P	Sal	P2	Ev	AT2	Q
WT	1	0.779	0.481	0.314	0.481	0.486	0.779	0.262
AT	0.779	1	0	0.613	0	0.617	1	0
P	0.481	0	1	-0.333	1	0	0	0.530
Sal	0.314	0.613	-0.333	1	-0.333	0.355	0.613	-0.732
P2	0.481	0	1	-0.333	1	0	0	0.53
Ev	0.486	0.617	0	0.355	0	1	0.617	0
AT2	0.779	1	0	0.613	0	0.617	1	0
Q	0.262	0	0.530	-0.732	0.530	0	0	1

The correlation coefficients are checked with the critical values for Pearson's correlation, for a two-sided test,

with a level of confidence of 5%. These critical values are given in table 4.11 [42] and depend on the number of samples (n) (table 4.10). These values are used to check the non-hypothesis: you cannot say that the correlation coefficient is not equal to 0. If a correlation coefficient from table 4.9 is larger than the critical value, than the non-hypothesis can be rejected and the correlation is not 0. The non-hypothesis cannot be rejected for the correlations WT-Sal, AT-P, Sal-P, Sal-Ev, Ev-P, Ev-Q and Q-AT. Some of these correlations need a larger number of samples, therefore more data is required.

Table 4.10: Number of samples for correlations, with WT = Water temperature, AT = Atmospheric Temperature, P = Precipitation, Sal = Salinity, Ev = Evaporation, Q = Discharge

Parameter 1	Parameter 2	Number of samples	Rejected (✓) not rejected (x)
WT	AT	22	✓
WT	Sal	18	x
WT	P	22	✓
AT	Sal	18	✓
AT	P	22	x
Sal	P	19	x
Sal	Q	11	✓
Sal	Ev	11	x
Ev	P	368	x
Ev	Q	273	x
Q	AT	272	x
Ev	AT	169776	✓
P	Q	272	✓

Table 4.11: Critical values Pearson's correlation with a 5% confidence interval

Number of samples - 2	Critical value Pearson
9	0.602
10	0.576
11	0.553
12	0.532
13	0.514
14	0.497
15	0.482
16	0.468
17	0.456
18	0.444
19	0.433
20	0.423
> 100	0.195

The correlation coefficients for which the non-hypothesis is rejected can be interpreted using the definitions of table 4.12. As the interpretation of correlation coefficients vary per context, for simplicity the interpretations of Hinkle (1988) [28] are used. The strength of the correlation is not dependent on the sign.

From the correlation coefficient matrix (table 4.9) can be observed that the salinity is mostly dependent on the discharge, which has a negative correlation of -0.732. This can be explained by the freshwater inflow which lowers the salinity in the lagoon. The water temperature is mostly dependent on the atmospheric temperature with a positive correlation of 0.779. These two correlations are the only parameters that have a high correlation. There are three combinations that have a moderate positive correlation: atmospheric temperature - evaporation, atmospheric temperature - salinity and precipitation - discharge, with a correlation coefficient of 0.617, 0.613 and 0.530 respectively. However, a side note must be made with respect to the correlation between atmospheric temperature and evaporation. The data set of evaporation is not based on measurements, but is calculated using Penman's equation, equation 4.1. The values of different data sets are used, including the atmospheric temperature data set. So, this results in a higher correlation. The correlation

Table 4.12: Interpretation of the Pearsons ranked correlation coefficient [28]

Size of correlation coefficient	Interpretation
0.90 to 1.00 (-0.90 to -1.00)	Very high positive (negative) correlation
0.70 to 0.90 (-0.70 to -0.90)	High positive (negative) correlation
0.50 to 0.70 (-0.50 to -0.70)	Moderate positive (negative) correlation
0.30 to 0.50 (-0.30 to -0.50)	Low positive (negative) correlation
0.00 to 0.30 (0.00 to -0.30)	Negligible correlation

atmospheric temperature - salinity, probably contains some intermediate steps. Two possible reasons for this correlation are: higher atmospheric temperature corresponds to periods of lower precipitation and thus lower discharges which results in a higher salinity, or higher atmospheric temperature results in higher precipitation rates, less water in the basin and thus a higher salinity. The correlation between precipitation can be explained by the fact that the Palizada river is a precipitation river. Higher precipitation rates will result in a higher discharge.

The results are based on datasets of different locations. The consequence of this is that the correlation coefficients may be weaker than they would be in reality. Also the measurement frequencies of the datasets are different. This has a large effect for cluster 1. To determine the correlation, all the measurements are monthly averages for cluster 1. This reduces the datasets of cluster 1 to 22 values to compute the correlations. For cluster 2 and cluster 3 the entire dataset is used.

4.4.3. Semi-correlations
Semi-correlations are a tool to validate how well a certain copula describes the bivariate distribution of variables X and Y. In this method the empirical data of X and Y is transformed to standard normal, meaning X and Y have a mean equal to zero and a standard deviation equal to one. Accordingly this data is plotted and divided into quadrants where the vertical line is located at the mean of the X data and the horizontal line is located at the mean of Y data. The definition of the quadrants is as follows: Quadrant 1 is the north eastern quadrant, Quadrant 2 is the north western quadrant, Quadrant 3 is the south western quadrant, Quadrant 4 is the south eastern quadrant. Next, the correlation coefficients of each quadrant are calculated, which are called the semi-correlations. Like the correlation coefficients the semi-correlations have a value between -1 and 1 to express the linear dependence between variables X and Y. These values are compared to several families of copulas, for example the Gaussian copula, to determine which copula represents the empirical copula best. It might be the case that one copula is best in describing a certain quadrant while another quadrant is not well described by the same copula. Therefore the choice for a copula also depends on which quadrant is of most interest. For instance in the case of flooding (maxima) the upper quadrant is the most important, while in the case of drought (minima) the lower quadrant is most important.

In section 4.4.2 it was found that only two correlations can be indicated as a high correlation. Firstly the water temperature and atmospheric temperature and secondly the salinity and discharge. As mentioned before the correlation between salinity and discharge is only based on the 12 monthly averaged values due the non-corresponding measuring times. Therefore, only the correlation between water temperature and atmospheric temperature is investigated using semi-correlations.

Water temperature and atmospheric temperature
Figure 4.26 shows the bivariate distribution of the water temperature and atmospheric temperature transformed to standard normal. Based on the correlation of these parameters different copulas are fitted from which the semi-correlations are calculated. The plots of these copulas can be found in appendix N.
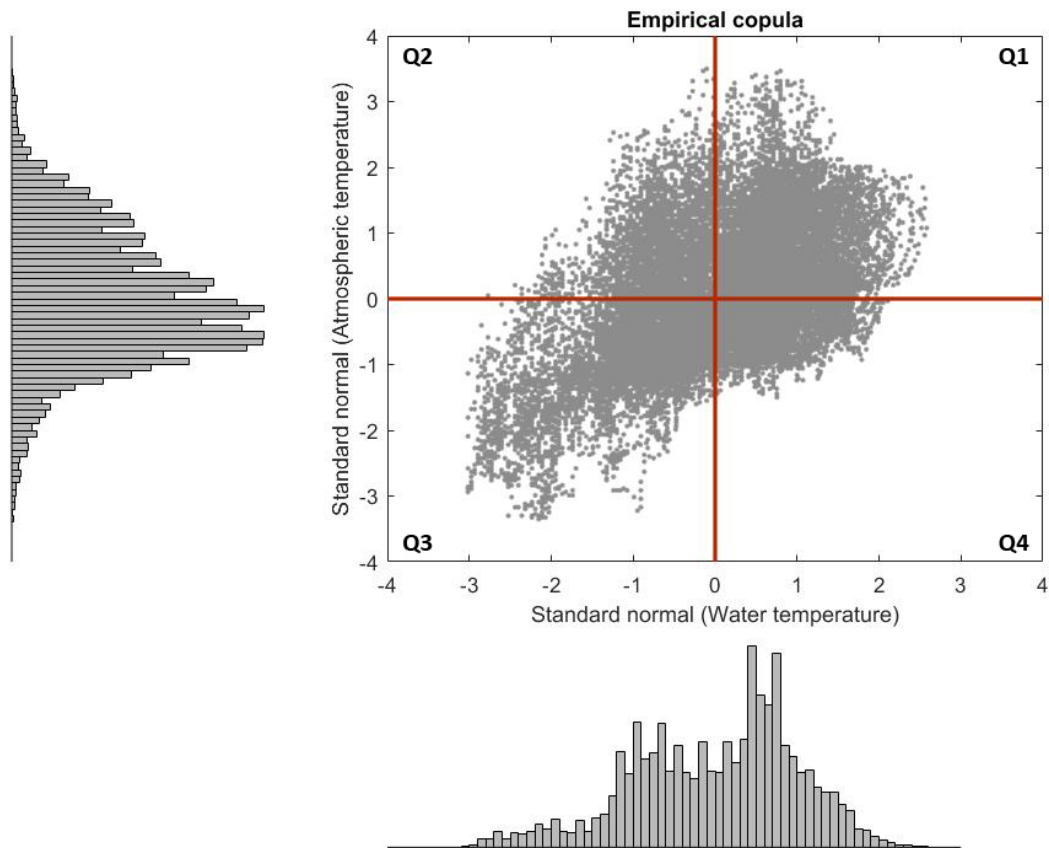
Figure 4.26: Semi-correlation water temperature and atmospheric temperature

Table 4.13 shows the Pearson's correlations for each quadrant, for the empirical copula as well as the other copulas. At first sight, there is not a distribution which represents the empirical data well in each quadrant. The lower tail, in quadrant 3, is best described by T. The upper tail, in quadrant 1, is best described by Clayton. The remaining quadrants 2 and 4 are reasonably represented by respectively T and Frank. Overall, the T-copula is considered to give the best representation of the empirical bivariate distribution.

Table 4.13: Values of the semi correlations between water temperature and atmospheric temperature

	Quadrant 1	Quadrant 2	Quadrant 3	Quadrant 4
Empirical	0.0442	0.2110	0.5974	0.1314
Gaussian	0.2802	0.1321	0.3747	0.0729
Gumbel	0.7038	0.1712	0.4181	0.2302
Clayton	0.1759	-0.0459	0.7703	0.0281
Frank	0.3747	0.1183	0.3592	0.1940
T	0.5083	0.2258	0.5117	0.0478

Results and discussion - Spatial distribution

In this section the results and discussion of the spatial distribution of salinity, water temperature, dissolved oxygen, Secchi depth and sediments are given. Where possible, the seasonal distribution of the spatial characteristics is presented. The profile line of the fieldwork measurement locations can be observed in figure 5.1. The point indicated with the yellow arrow in figure 5.1b is an additional measurement, which was added a few hours later after hypoxia was measured. Measurements of the field campaigns were taken during upcoming flood.
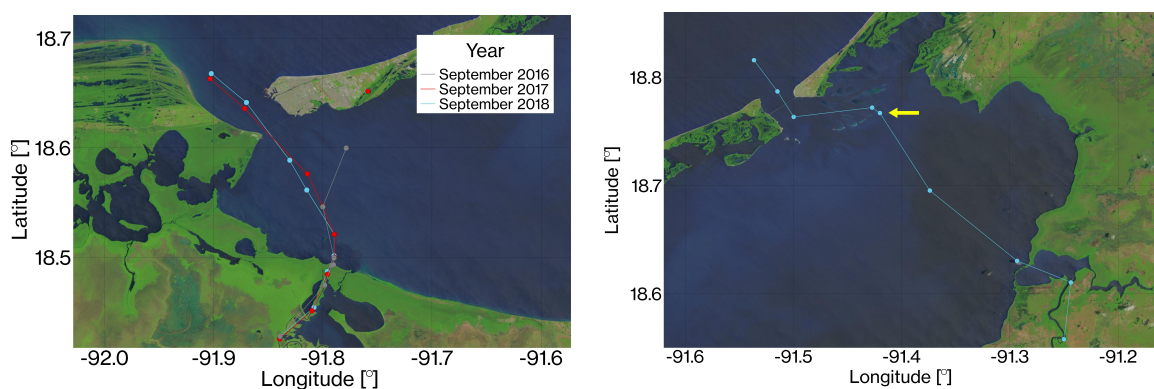
(a) Palizada campaign measurement locations and corresponding profile lines

(b) Candelaria campaign measurement locations and corresponding profile line

Figure 5.1: Profile lines and measurement locations field campaigns, background image from Landsat 8 13-04-2018

5.1. Salinity

Salinity at different depth percentages is shown in figure 5.2 for the fieldwork measurements done in September 2018. The depth percentages are similar to the three depth percentages of the Delft3D-FLOW models. Percentages per line indicate at what depth percentage the salinity is calculated. Depth averaged salinity profiles of the Palizada and Candelaria profiles are given in figure 5.3.

Figure 5.4 shows different modelled salinity depth profiles. In appendix J more results of the salinity profiles over depth from different stations and seasons are given. In figure 5.5 the depth averaged salinity in PSU is shown for the three different seasons at station 6 (close to the Palizada river mouth, see appendix F), determined with Delft3D-FLOW. This model included tides, wind and the Palizada river discharge.
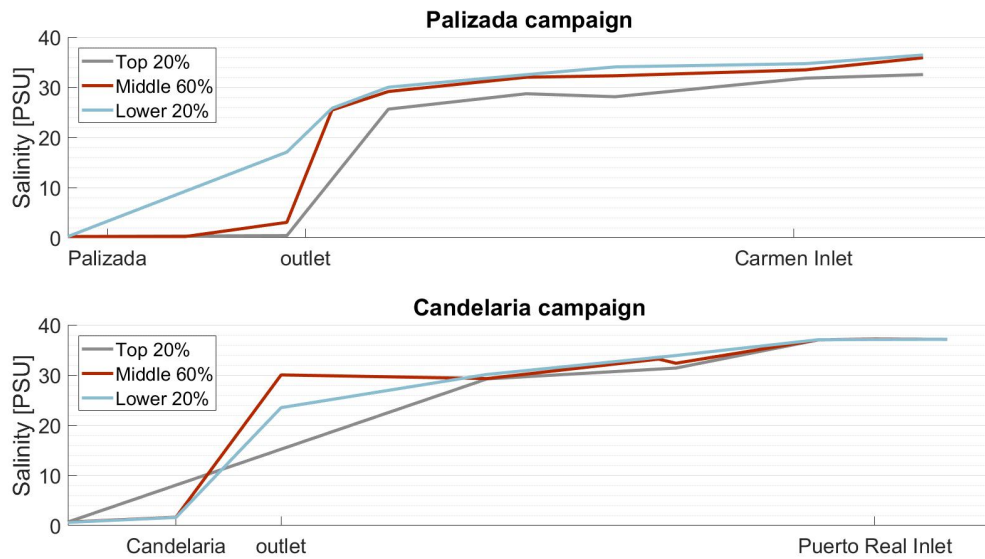
Figure 5.2: Salinity profiles field campaigns 2018 at varying depth percentages

(a) Salinity of Palizada measurement campaigns

(b) Salinity of Candelaria measurement campaign
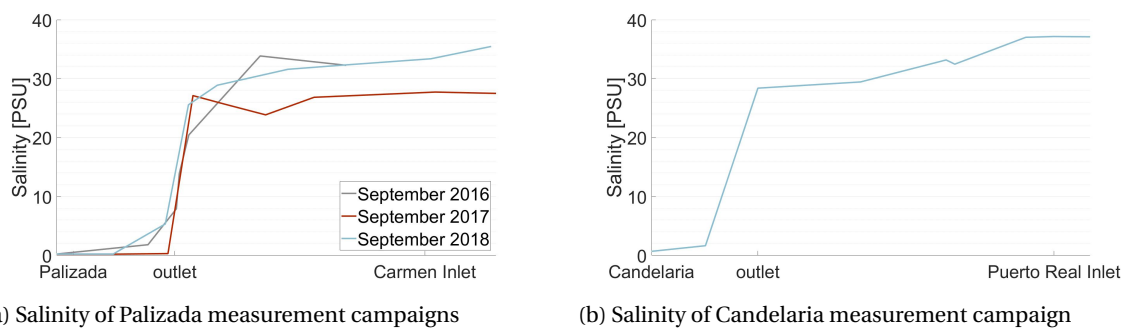
Figure 5.3: Salinity profiles of the measurement campaigns

Figures 5.2 and 5.3 show that salinity spikes significantly when water reaches the lagoon. The two measurement campaigns show similar patterns in salinity, where depth averaged salinity increases from river outlet to tidal inlet. Along the chosen lines, salinity in the lagoon is lower than at sea. From the field measurements it seems that the eastern part of the lagoon is mixed better over depth and is slightly more saline, as the salinity of the top, middle and bottom parts of the lagoon lay closer together for the Candelaria campaign than the 2018 Palizada campaign (figure 5.2). This is probably due to the shallower regions of the eastern Terminos Lagoon, in comparison with the western lagoon.

As the Palizada is the biggest contributor of fresh water to the lagoon, lower salinity in the western part of the lagoon would be expected. However, this expected lower salinity in the western part does not show in the field measurements. Also, the differences between different years show larger deviation in salinity than the difference between the eastern and western part of the lagoon in one year.

Figure 5.3 shows that in 2017, the salinity was lower than salinity in 2016 and 2018. At larger water depth, salinity is mainly higher than in shallower water layers, showed by figure 5.2. This can be a result of different tides or weather conditions at data collection moments. The top 20% layer for the Candelaria campaign is lacking data points near the river mouth. This lack of data points explains the intersection of the top 20 % line with the other two lines.

From the modelled depth averaged salinity in figure 5.5, it turns out that there is variation in salinity in space. The variation in salinity is strongly related to the discharge of the Palizada river and thus the seasons. The

(a) Dry season   (b) Rainy season   (c) Nortes season
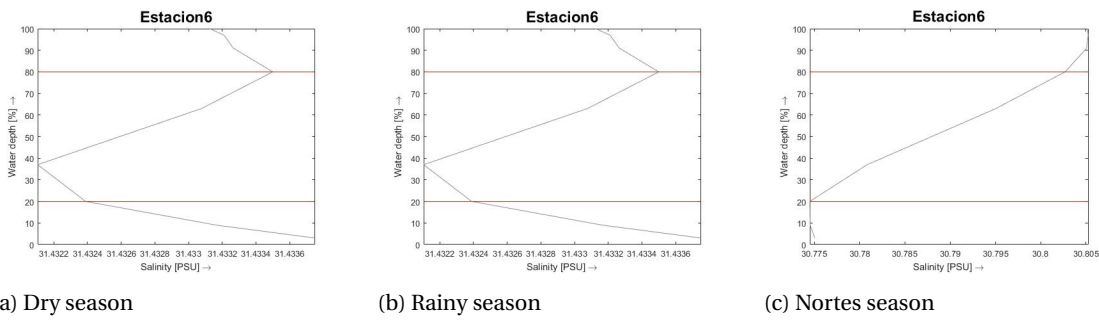
Figure 5.4: Salinity profile over depth of Estacion 6 for different seasons

difference can be seen if the dry season, figure 5.5a, is compared to the rainy and Nortes season, figure 5.5b and figure 5.5c respectively. From the fieldwork measurements and the Delft3D-FLOW model follows there is also variation in salinity over depth. However, this variation in salinity over depth at one location is smaller than 0.1 PSU, according to the Delft3D model. This means the system can be considered as well mixed. The effect of the river on the salinity becomes clear in figure J.2 and figure J.3. In these figures, the salinity of the upper layer is larger than the salinity deeper in the water column, this changes at Estacion 6, see figure J.4. These figures show variation of salinity over depth. However the field measurements (figure 5.2) indicate that the variation at one location and at one specific moment in time is larger than the variation of the salinity over depth by the Delft3D-FLOW model.

(a) Depth averaged salinity - dry season   (b) Depth averaged salinity - rainy season

(c) Depth averaged salinity - Nortes season
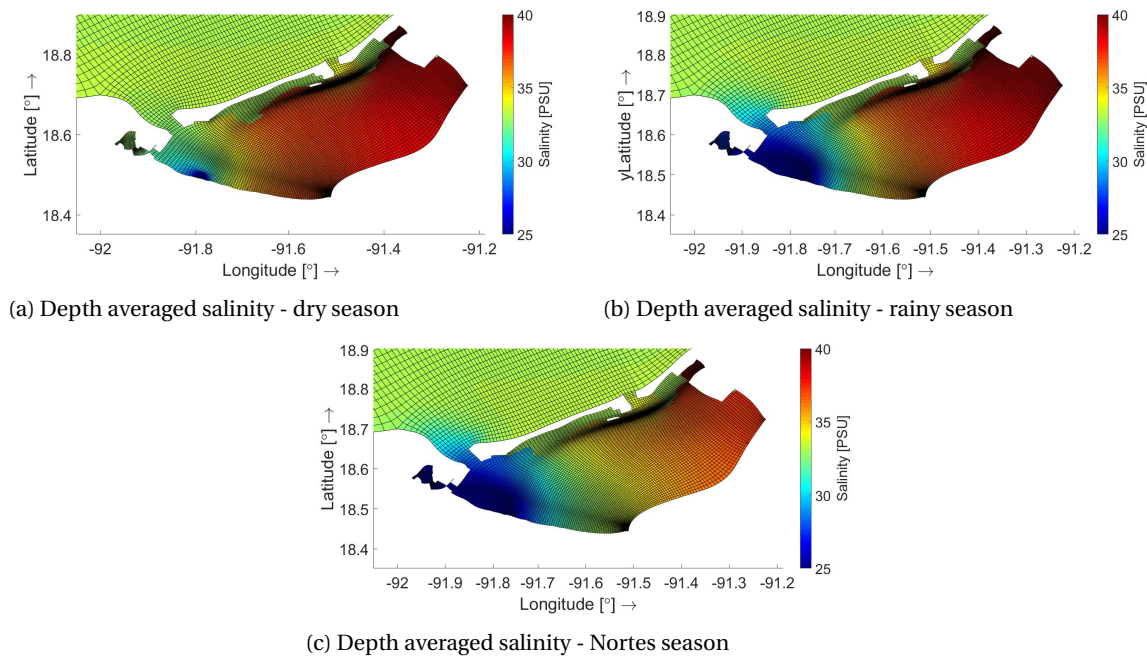
Figure 5.5: Depth averaged salinity of the different seasons

Combining figures 5.5 and 5.3a, figure 5.6 is created. While the modelled seasonal averaged values are remarkably close to the measured salinities, negligible differences in salinity over depth are present in the model. Figure 5.6 represents the western part of the lagoon. Salinity is overestimated for the eastern part of the lagoon by about 10 PSU. The salinity of the Palizada river being set to zero in the Delft3D model thus seems appropriate. More fresh water outlets should be included in the Delft3D-FLOW model to better model the eastern lagoon.
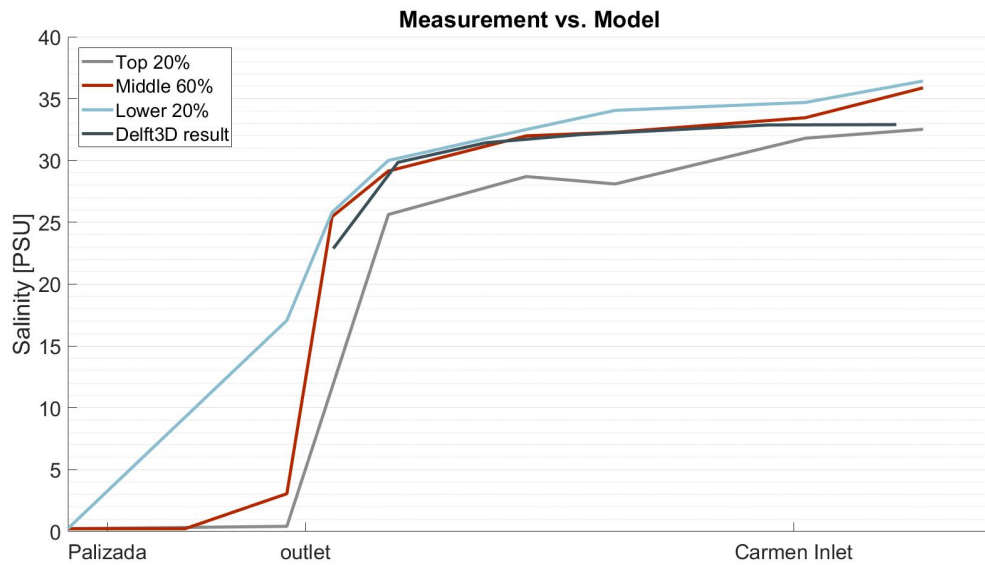
Figure 5.6: Comparison salinity Palizada campaign to Delft3D-FLOW model for rainy season

5.2. Water temperature

The water temperature profiles of Palizada and Candelaria campaigns are shown in figure 5.7. The profiles follow the line of the fieldwork campaigns as shown in figure 5.1.

Figure 5.7 shows that the temperature is increasing from Palizada and Candelaria to river outlet. From the river outlet to the tidal inlet, the temperature decreases for the Candelaria campaign. For the Palizada campaign the temperature fluctuates. The water temperature over the lagoon are less constant for the Candelaria campaign than the Palizada campaign. The coolest year, 2017, shows lowest water temperatures.

(a) Water temperature profiles of Palizada measurement campaigns

(b) Water temperature profile of Candelaria measurement campaign
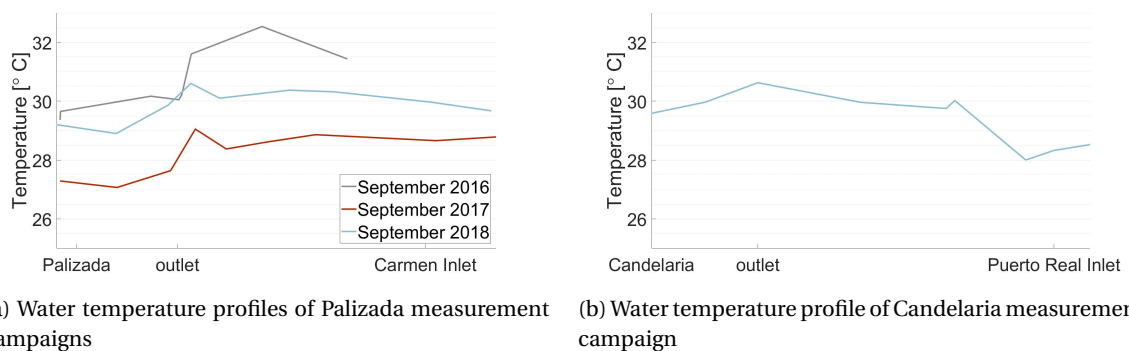
Figure 5.7: Water temperature profiles of the measurement campaigns

Figure 5.8 shows the spatial distribution of top of atmosphere brightness temperature within Terminos Lagoon for dry, rainy and Nortes seasons during flood tide. These figures are chosen as representative for that specific season. A comparison at peak horizontal ebb for two seasons is given in figure 5.9. Temperature distribution maps for other dates can be found in appendix D.

(a) Dry season, 07-05-2015

(b) Rainy season, 26-07-2015

(c) Nortes, 20-01-2017
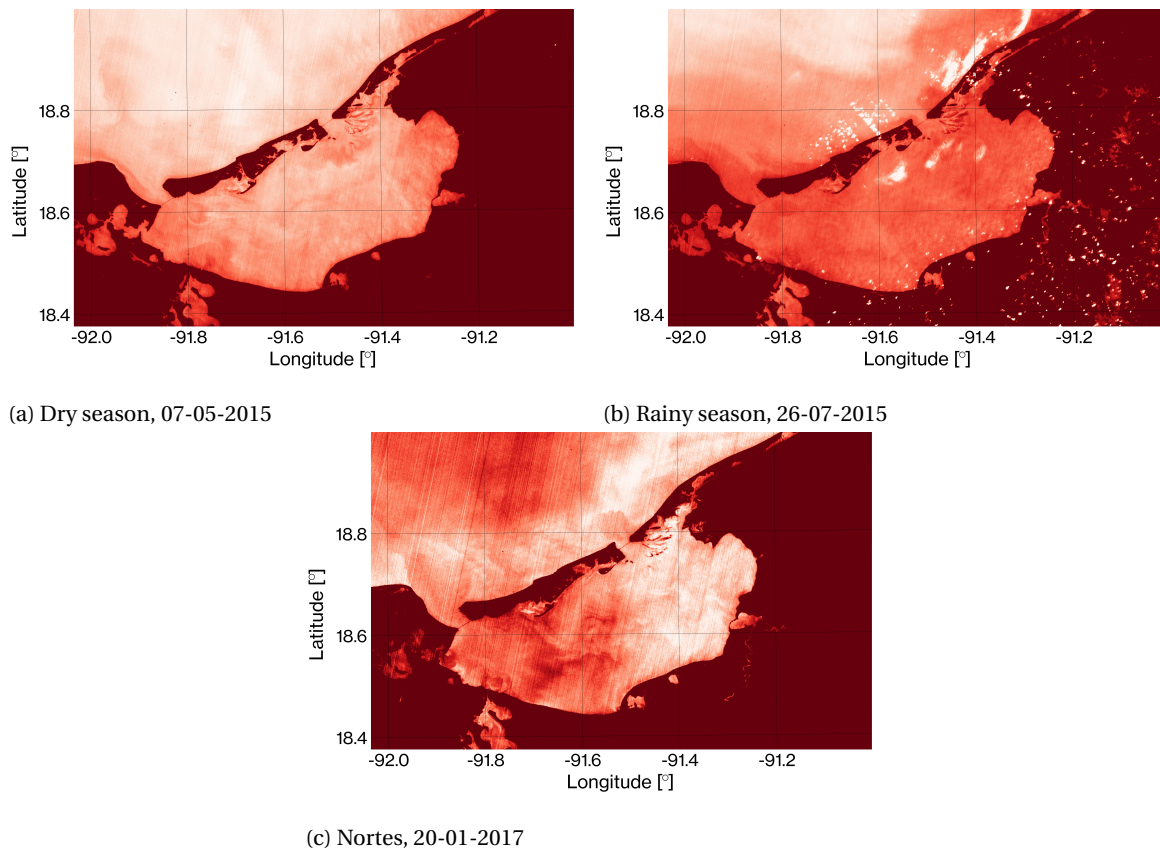
Figure 5.8: Spatial distribution of temperature in Terminos Lagoon for the different seasons during flood. White indicates cooler regions, red indicates warmer regions

(a) Dry season, 01-03-2014

(b) Nortes, 28-01-2014
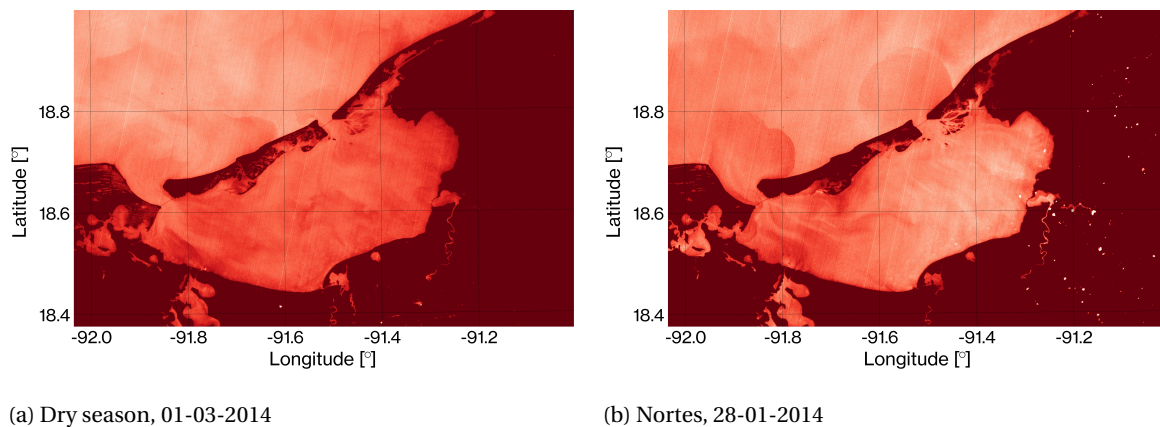
Figure 5.9: Spatial distribution of temperature in Terminos Lagoon for the different seasons during ebb. White indicates cooler regions, red indicates warmer regions

Figures 5.8 and 5.9 show that the water temperature is higher close to land surfaces. This warmer water spreads along the dominant local flow direction. This temperature structure comes back in figure 5.7a and 5.7b. The swirls in the middle of the lagoon observed in these figures roughly correspond with the circulating residual current in the eastern part of the lagoon. This confirms the presence of the residual current as described in subsection 4.2.3. During dry season, the northward movement of the circulating residual current cannot be seen in the water temperature distribution. Tides are distinguishable by looking into water temperature distribution. During ebb, a zone with different temperatures than its surroundings is visible from tidal inlet into the sea. The opposite is true during flood. The lagoon main basin has often a higher water temperature than the sea, the western part most often has a higher water temperature than the eastern part.

During Nortes, the temperature difference between west and east follows the boundary of the tidal watershed (subsection 4.2.2). This is visible in figures 5.8c and 5.9b. During ebb, the water that is flowing out of the lagoon is flowing further away during Nortes than during dry season, which is seen in the larger temperature zones at the Carmen inlet during Nortes. This is visible in figure 5.9. The reason for this might be the additional water that flows out of the lagoon due to the larger river discharge in the Nortes season. Conform the field measurements, the temperature from Palizada river to Carmen tidal inlet is close to constant, with highest temperatures close to the river outlet.

Temperature structures over a large area are easily disturbed by clouds. For the rainy season, this causes problems in acquiring clear thermal images of the lagoon. The low overpass frequency of the Landsat missions, 15 days, gives high uncertainty of good circumstances on a given day. Other problems are the tides. These are distinguishable from resulting images, but should always be taken into account when using applied methodology.

5.3. Dissolved oxygen

Figure 5.10 shows the dissolved oxygen concentration according to the field measurements along the lines of both Palizada and Candelaria river in figure 5.10a and 5.10b respectively.
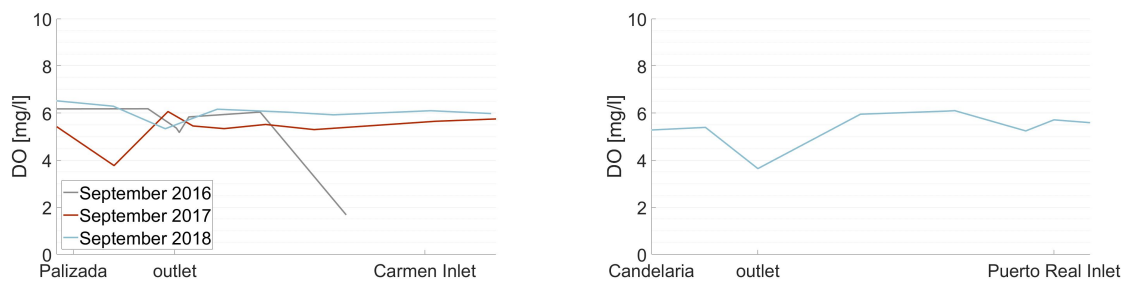
(a) Dissolved oxygen profiles of Palizada measurement campaign

(b) Dissolved oxygen profile of Candelaria measurement campaign

Figure 5.10: Dissolved oxygen profiles of the measurement campaigns

In 2017, the average lowest dissolved oxygen concentration is measured for the Palizada measurement campaign, see figure 5.10. The east side of the lagoon has lower dissolved oxygen concentrations than the west side of the lagoon. It is noticeable that dissolved oxygen concentrations show high variations. Furthermore, as only daytime dissolved oxygen concentrations are measured, daily variations cannot be investigated.

5.4. Secchi depth

Figure 5.11 shows the Secchi depth results along the line of the fieldwork campaigns, respectively Palizada and Candelaria in 5.11a and 5.11b. It shows the lowest measured Secchi depths at the river outlet. The fieldwork results show that water tends to get clearer away from the river, up until right after the inlet, where Secchi depth drops again. Changes over the years are relatively small, though noticeable. The 2016 Palizada campaign has clearer water in the direction of the Carmen inlet, which is most likely due to a combination of upcoming ebb and the location of the last measurement. The east has clearer water than the west of the lagoon.

In figure 5.12 the Secchi depth from remote-sensed data is shown for the three different seasons. These figures are chosen as representative for the corresponding season, during flood tide. Secchi depth from remote-sensed data is also determined during ebb for dry season and Nortes, which are shown in figure 5.13. The west of the lagoon and the Carmen inlet have relatively low Secchi depth, which probably is the result of the Palizada river. This result comes back in the fieldwork data (figure 5.11). High sediment output of this river and flow in western direction seem to accumulate more light-reflecting particles in the west, compared to elsewhere in the lagoon. In the tidal flats near the Puerto Real inlet there is a local minimum, possibly caused by erosion of the tidal delta. The water of Terminos Lagoon seems more clear in the centre and east of the lagoon. In between these clearer areas, more turbid water is observed. This turbid water can be a result of particles from eroding tidal flats as they move from the inlet and follow the residual current. Along the coast
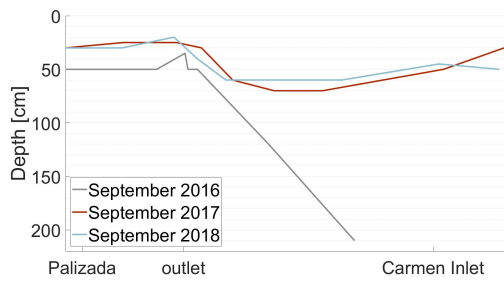
(a) Secchi depth profiles of Palizada measurement campaign
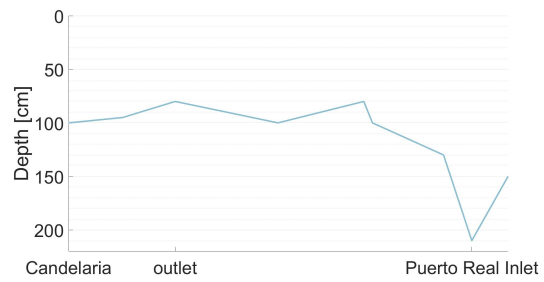
(b) Secchi depth profile of Candelaria measurement campaign

Figure 5.11: Secchi depth profiles of the measurement campaigns

of Isla del Carmen and in the western lagoon, Secchi depth is low. Water near river mouths are more turbid than surrounding areas, as the rivers bring with them more light-reflecting particles. It is also evident that there are more sunlight reflecting particles near the western banks of the mainland outside of the lagoon than along the coast of Isla Aguada.
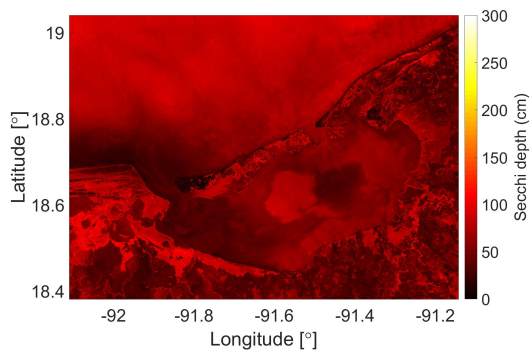
(a) Dry season, 07-05-2015
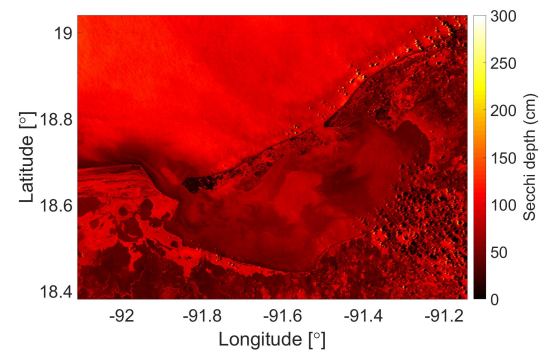
(b) Rainy season, 08-08-2014
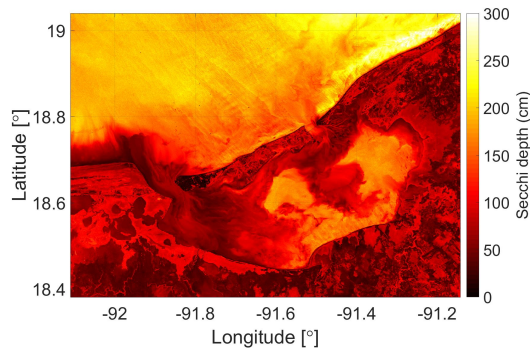
(c) Nortes season, 20-01-2017

Figure 5.12: Secchi depth in Terminos Lagoon for different seasons during flood

(a) Dry season, 01-03-2014   (b) Nortes season, 28-01-2014
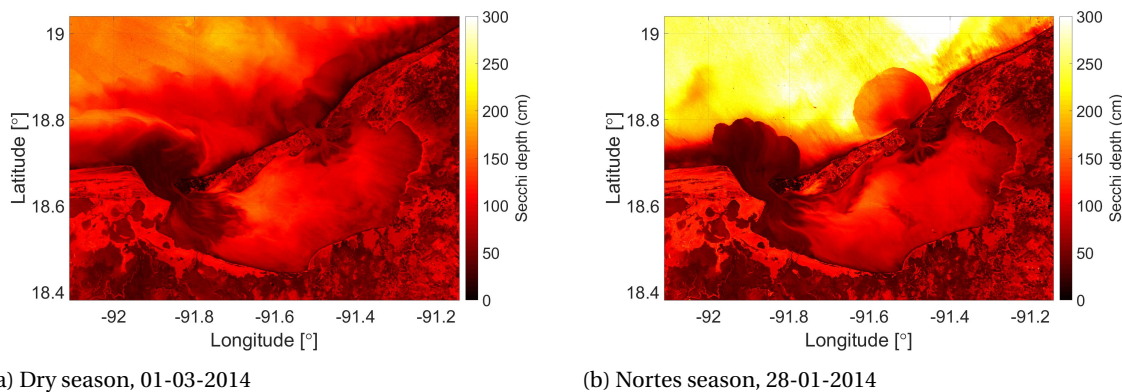
Figure 5.13: Secchi depth in Terminos Lagoon for different seasons during ebb

Nortes seems to be significantly less turbid than other seasons. The surrounding landscape and the Gulf of Mexico further from the coast, assumed to provide a relatively constant Secchi depth, but the Secchi depth changes during all seasons in this area. These differences may be attributed to differences in atmospheric properties between the seasons. It cannot be concluded whether this attributes to all of the differences observed. Similar as in thermal imagery (figure 5.9), it seems from figure 5.13 that during ebb in the Nortes season water is transported further out of the lagoon than during ebb in dry season. The field measured Secchi depths look similar to the remote-sensed Secchi depths for the western Terminos Lagoon in the rainy season, see figure 5.11 and 5.12. Secchi depth discrepancy between field measurement and remote-sensed measurements is larger for the eastern lagoon than the western part.

The eastern part of the lagoon seems significantly clearer than the western part, which is in line with the field measurements. This is most likely caused by the combination of flow patterns and the Palizada river. Generally, the residual current is in the direction of the Carmen inlet and the Palizada river is the biggest contributor of sediments to the region. Based on Secchi depth, the Terminos Lagoon can be divided in two parts: in a more clear eastern part and a more turbid region in the western part. The turbidity of the centre and east of the lagoon seem to be strongly tidally dependent. This also explains the relatively large "jump" in Secchi depth for the two measurement points of the Candelaria campaign, which were measured close to each other at different times.

5.5. Sediments

Sediments are deposits that settle the bottom of a liquid. The amount of the deposits is unknown, therefore a quantitative description of the sediments is not given. However, the distribution of the sediment sizes is available, see figure 5.14. In this figure the sediments are divided by grain sizes: clay < 0.002 mm, 0.002 < silt < 0.063 mm and 0.063 mm < sand < 2 mm.

Sand size sediment is present at Puerto Real inlet, the navigation channel of the Carmen inlet and the coast of Isla del Carmen. Sediments with a silty clay size are located at the Candelaria en Mamantel estuary, at the east of the lagoon and at some smaller regions in the middle of the lagoon. A mix of sand, silt and clay sized sediments are deposited at the Palizada estuary, the Carmen inlet and a region across the lagoon. The sediments in the rest of the lagoon consist of silty and clayey sand deposits (figure 5.14).
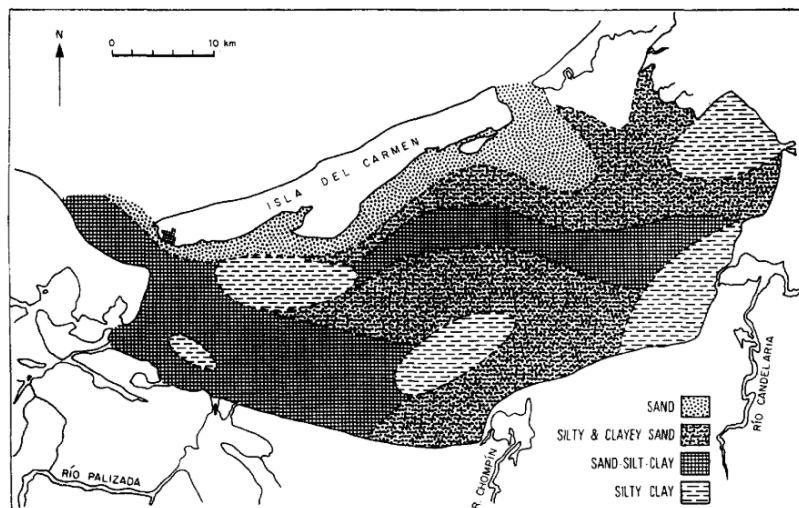
Figure 5.14: Distribution of sediment sizes in Terminos Lagoon [44]

Sediments are transported by currents, so the sediment distribution is influenced by the residual current direction (figure 4.16) [14]. The distribution of alluvial sediments depends on the river discharge. It can be assumed that the alluvial sediments have a relatively large range in grain sizes: from clay to sand [11]. The sediments imported at the Puerto Real inlet are carbonate salty silts, which have a greater grain size than carbonate mud, that is imported by the Carmen inlet (see figure 4.24). Figure 5.14 also shows that the sediment size is larger near the Puerto Real inlet than the Carmen inlet. However, there is a difference in grain size, because in figure 5.14 the sediments near the Puerto Real inlet have a sand size and the sediments outside the Puerto Real inlet have a silt size (figure 4.24). One reason of this difference could be that two different soil classification rules are used.

The area of the present alluvial sediments, with a wide range of particle sizes, is greater for the Palizada river than for the Candalaria, Chumpan and Mamantel rivers. So the Palizada river transports more alluvial sediments than the other rivers. The discharge is higher for the Palizada river than the other discharging rivers. So a higher river discharge could lead to a greater distribution area of alluvial sediments. By looking at figure 5.14, it seems the Palizada river sediments are deposited in an area from the outlet of the Palizada river to the Carmen inlet, so the direction of the sediment transport by the river is expected to go from the Palizada outlet to the Carmen inlet. This is conform the residual current in figure 4.16.

The Secchi depth is lower for the zones with sand silt clay sized material and sand sized sediments. The Secchi depth is higher for silty and clayey sand. These results could mean that the sand silt clay sized material contains more sediments that can be in suspension in comparison with the silty and clayey sand. The presence of erosion could be a reason why the Secchi depth is smaller in the zones with sand silt clay sized material. The suspended sediments from erosion lead to lower Secchi depths, visible in figure 5.12.

6

Results and discussion - Future developments

In this chapter possible future developments will be discussed. First developments in climate change will be touched on, then the potential morphological changes of Terminos Lagoon. Finally, input of industrial contaminants into the lagoon will be briefly discussed.

6.1. Climate change

According to Eugene Y. Chan [17] climate change refers to a gradual change in the Earth's climate and physical geography that accompany an increase in the Earth's temperature. Today, it is one of the greatest challenges facing life on Earth [17]. Both international and regional effects can be distinguished. Acknowledged effects are sea level rise, increase in global temperature and more extreme weather events.

Likewise, Terminos Lagoon could be influenced by changes in climate. Though most models agree on the sign of change for atmospheric temperature and precipitation rates on a global scale [33], exact numbers are difficult to predict. For Terminos Lagoon, increased atmospheric temperatures and sea level are likely to occur. Precipitation rate changes are more uncertain, as mentioned models show changes in sign of precipitation rate change per season [33]. Relevant to this study is how various hydrological and hydrodynamic processes, as well as the spatial characteristics within Terminos Lagoon will change. Hence, the scenarios that are considered on the case of Terminos Lagoon are:

- change in annual precipitation rate;
- increase in atmospheric temperature;
- increases in sea level.

The scenarios will be described using the information gathered in the previous chapters. Information from, among others, the water balance and statistical dependencies are used to substantiate possible consequences following said scenarios. These consequences are qualitatively in nature, though quantitatively where possible.

6.1.1. Change in precipitation rate

Changes in precipitation rate influence the influx of fresh water into the lagoon. All rivers that flow into the lagoon are rain-fed rivers and therefore will be influenced by a change in precipitation rate. The moderate positive correlation of 0.53 between precipitation and discharge confirms this (section 4.4). A change in water influx will change the net outflow through the inlets as well. Probable changes in precipitation are hard to quantify. Therefore, both an increase and decrease of 20 %, arbitrarily chosen extreme scenarios, in yearly average precipitation rate are looked at for the water balance. New water balances are made, under the assumption that an increase in precipitation would increase the influx of fresh water through both rain and river by the same margin. They are shown in figure 6.1.
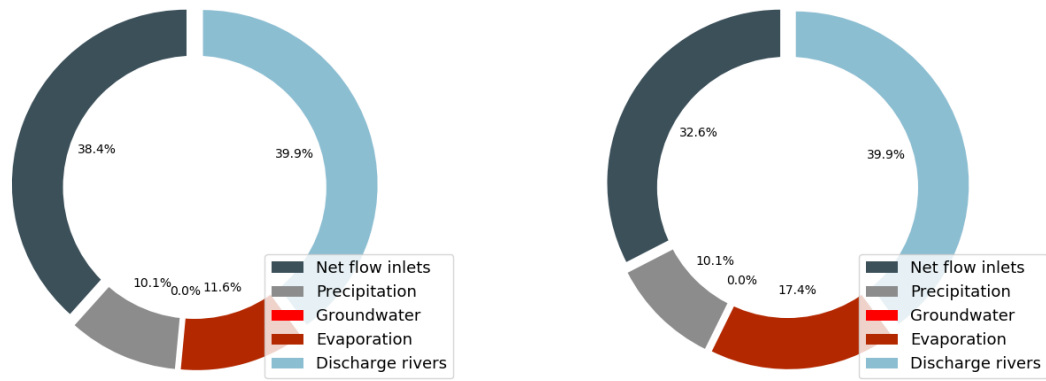
(a) Increase of precipitation with 20%   (b) Decrease of precipitation with 20%

Figure 6.1: Water balance for changes in precipitation rate based on the Penman calculation

Following figure 6.1, it is found that an increase of precipitation will lead to relatively higher net flow through the inlets. The opposite applies for a decrease in precipitation. Although relative changes are small, absolute changes are of significant influence. Note that inflow always equals outflow and both inflow parameters, precipitation and discharge rivers, are increased relatively the same, resulting in relatively the same relevance on the water balance for both an increase and decrease in precipitation.

A consequence of an increase in precipitation is that more water has to be transported from river to the tidal inlet. Biggest absolute change would be for the Palizada river, assuming all rivers are affected relatively the same. Residual flow velocities through the inlets will increase likely, most noticeable at the Carmen inlet.

Another effect of a change of precipitation is a change in salinity of the lagoon. According to table 4.9, there is a high negative correlation between river discharge and salinity of -0.732. Higher precipitation rates are likely to decrease salinity and vice versa.

6.1.2. Increases in atmospheric temperature
Another possible effect of climate change is an increase in atmospheric temperature, and therefore an increasing evaporation rate. In figure 6.2 the evaporation rates as a result of increasing atmospheric temperature are shown. These evaporation rates are a result of changing the temperature term in the Penman calculation (appendix H).
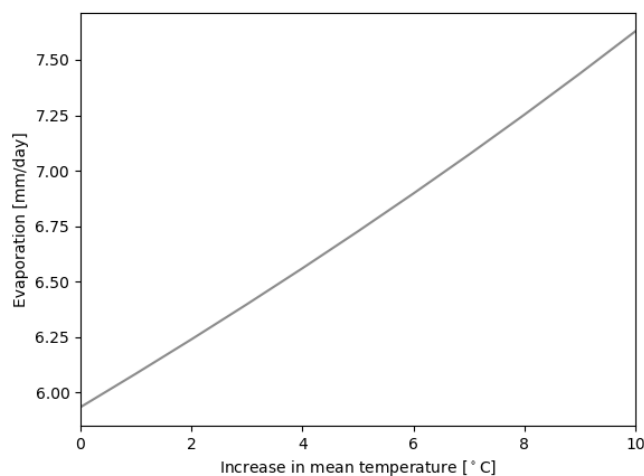

Figure 6.2: Change in the evaporation rate with increasing atmospheric temperature

Atmospheric temperature increase has a positive effect on the lagoons evaporation rate and the water temperature. Both correlations between, atmospheric temperature & water temperature and atmospheric temperature & evaporation are high and moderate with 0.779 and 0.617, respectively (table 4.9). Figure 6.2 shows a linear relation between atmospheric temperature increase and evaporation rate. An increase of 1 °C will lead to 0.16 mm/day, or 3.12 m³/s extra evaporation, according to the Penman calculation. The increase in evaporation will affect the water balance, where the outflow via evaporation will become a larger part. There is more outflow through evaporation, which decreases the net outflow via the inlets under the assumption other water fluxes remain unchanged. Relatively speaking, these effects will influence dry season most, as the evaporation rate has the relative largest influence in the water balance during dry season (figure 4.9). The water balances of rainy and Nortes seasons will not be affected as much by evaporation increases, as evaporation is a smaller component of the water balance for these seasons.

By examination of the top of atmosphere brightness temperature, the eastern part of the lagoon is slightly cooler than the western part of the lagoon (appendix D). The eastern part is also shallower (figure 2.5). A thinner layer of water warms faster than a thick one. Thus, disregarding other influences, the eastern part of Terminos Lagoon likely warms more easily than the western part.

6.1.3. Increase in sea level

A higher sea level will lead to an increase in the water level of the lagoon, as both mediums are connected. This implies that the volume of the basin increases, as well as the surface area of the tidal inlets. The tidal prism is not expected to increase significantly. The combined effect of the increase of surface area of the tidal inlet and a nearly unchanged tidal prism is a decrease in flow velocities through the inlet. This will result in sedimentation in the inlet. In section 6.2 the morphological changes of the inlets are investigated more thoroughly.

According to equation L.1, a larger volume of water will increase flushing time, as the tidal prism is not expected to increase significantly and therefore the volume of tidal flow is also not expected to increase. An increase of 10 cm of water level theoretically decreases flushing time by 3.8 % in this context. Assuming no other changes, sea level change does not have a significant impact on the local water balance of Terminos Lagoon.

6.2. Morphological changes

The coastal zone is shaped by different natural processes, such as tides and currents, but also by anthropogenic interference. In this subsection the coastal area is divided in three components: the tidal inlets, the tidal delta and the adjacent coastline. Escoffier stability concept is used to test whether the inlet system is in equilibrium [22]. Next, the morphological changes over time are visualized to see how the tidal delta and the adjacent coastline evolve over time. Erosion may result in damage to existing infrastructure. On the other hand, sedimentation may result in required dredging activities to maintain the shipping channels.

6.2.1. Stability of the inlets

Tidal inlets exhibit a dynamic morphology due to locally strong tidal currents. The cross-sections of the inlets change over time. The stability of the inlets has significant influence on the flow patterns inside the lagoon. The following definition of inlet stability is used:

> *"The inlet is considered stable when it is not migrating and when its cross-sectional area is fixed at an equilibrium value A_{eq} or performs steady oscillations about A_{eq}."* [61]

The position of the inlets is more or less fixed by the foundation of the bridges over both inlets, though the shape of the inlets can change. The cross-sectional stability of an inlet is investigated by applying the closure curve by Escoffier [22]. Escoffier related the maximum entrance channel velocity to the geometry of the inlet:

$$\hat{u}_e = \frac{\pi \cdot P}{A_{eq} \cdot T} \tag{6.1}$$

With:

$\hat{u}_e$	= maximum cross section averaged entrance velocity	[m/s]
T	= tidal period for a diurnal tide	[s]

A_{eq} = equilibrium cross-sectional area of the inlet below mean sea level   [m^2]
P = tidal prism   [m^3]

The amplitude of the velocity, which is the maximum cross section averaged entrance velocity ($\hat{u}_e$), is calculated using the equation of Escoffier, see formula 6.1. The tidal prism is already calculated based on the location of the tidal watershed and the tidal range (subsection 4.2.2). To estimate the tidal period, a part of figure M.1a is used. In this figure, the amount of tidal cycles is counted and divided by the time to determine the tidal period. This gives a tidal period of 24 hours and 35 minutes. The cross sections of the tidal inlets are shown in figure 2.6 (section 2.4). The areas for the Carmen inlet and the Puerto Real inlet are respectively 20,100 m^2 and 12,900 m^2. Results of the maximum cross section depth averaged entrance velocities are shown in table 6.1. Velocities are also calculated with Delft3D-FLOW. From the Delft3D-FLOW model, which included tides, wind and the Palizada river discharge, it follows that the depth averaged magnitude of the flow velocity of the Puerto Real inlet is 0.794 m/s and the velocity of the Carmen inlet is 0.486 m/s, see table 6.1.

Table 6.1: Comparison $\hat{u}_e$ by Escoffier and Delft3D-FLOW

Inlet	Escoffier $\hat{u}_e$ [m/s]	Delft3d-FLOW $\hat{u}_e$ [m/s]
Carmen inlet	0.446	0.486
Puerto Real inlet	0.766	0.794

To determine whether the tidal inlet is stable or unstable, the maximum cross section averaged entrance velocity should be around 0.9 m/s, which is a constant that only depends on the sediment diameter [22]. Escoffier and Delft3D-FLOW show that the maximum flow velocity in the inlets is smaller than 0.9 m/s, see table 6.1. So, this means that the inlets are not yet in equilibrium. How the cross sections of the inlets evolve over time can be schematically presented in the Escoffier curve. The Escoffier curve is a graph that shows the relation between the cross sectional area of the inlet and the maximum flow velocity. From the graph it follows that the inlet closes between A and B. Between B and E the inlet adapts till it reaches the natural equilibrium of point D. This can be achieved by erosion of the inlet, if the inlet is between B and D, or by sedimentation, if the inlet is between D and E. The position of the Carmen inlet and Puerto Real inlet in the graph are based on the cross sectional area (section 2.4). The maximum flow velocity in the Carmen inlet is lower and the cross sectional area is larger than the Puerto Real inlet. Therefore, the position of both inlets must be between point D and E in the Escoffier curve. The arrows in the figure show how the velocity and the inlet area change in time, based on their start position. Figure 6.3 shows the positions of the Carmen inlet and the Puerto Real inlet.
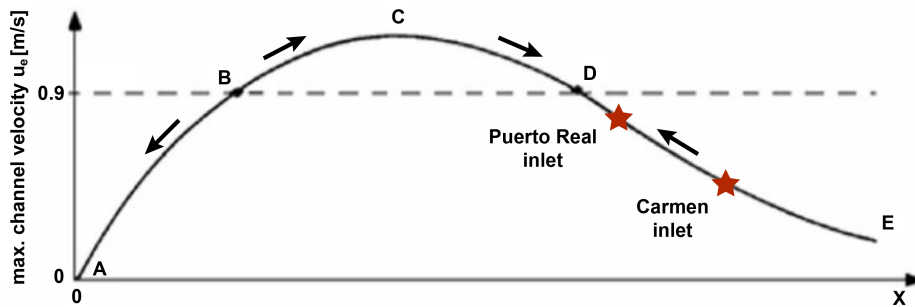
Figure 6.3: Escoffier closure curve, position of the Carmen inlet and Puerto Real inlet with on the x-axis the cross-sectional area and on the y-xis the maximum channel velocity in m/s [14]

It becomes clear that maximum flow velocities in the Carmen inlet are too low to maintain the flow area. The residual current direction of the Carmen inlet is outwards the lagoon, this is shown in subsection 4.2.3. So, when the discharges of other rivers, Candelaria, Mamatal and Chumpan will be taken into account, it is possible that the magnitude of the maximum flow velocity will increase. Nevertheless, it is not likely that

the maximum flow velocity will exceed the equilibrium flow velocity of 0.9 m/s, because the volume of water transported by the river is just a fraction of the tidal prism. Thus, the Carmen inlet is expected to sedimentate till it reached point D, the natural equilibrium, in figure 6.3. The flow velocities in the Puerto Real inlet are close to 0.8 m/s. As well as the Carmen inlet, it is not likely that the flow velocities will increase by taking into account the discharge of the Candelaria, Mamantal and Chumpan. The discharge of these rivers will presumably flow out through the Carmen inlet according to figure 4.16.

6.2.2. Tidal delta and adjacent coastline

Due to the tides there is an exchange of sediment between the basin and the areas outside the basin. This sediment exchange leads to sediment deposits, which are called tidal deltas. The tidal deltas consist of channels and flats. The delta located outside the basin is called an ebb tidal delta. The delta located inside the basin it is called flood tidal delta. This second type of delta can exist, because the flow is diverging after arriving at the lagoon, resulting in lower flow velocities and particle sedimentation. Tidal deltas show a dynamic behaviour. The interaction between waves and tides determines the morphology of the tidal delta. A wave dominated climate results in a stronger flood tidal delta, as the waves push the sediment landwards and the ebb tidal delta cannot spread out.

The Puerto Real inlet has a clear flood tidal delta, with channels and flats. When comparing the size of the tidal flats, it is found that they have retreated. This is shown in Figure 6.4 where the areas in red have retreated in the period from 1984 until 2016. The increase of vegetation might indicate that the flood tidal delta increased in height, although the decreased area of the flood tidal delta indicates a decreased volume of the flood tidal delta.

Figure 6.4: Size difference of the flood tidal delta of Puerto Real with in red the drowned flat area between 1984 and 2016 [3]

The sediment of the tidal delta may origin from different locations, such as the adjacent coastline, the basin or from offshore. In figure 6.5 the change of the adjacent coastline around the Carmen inlet is presented. The red line represents the situation of the coastline in 1988, the map shows the situation of 2014.

Figure 6.5: Aerial map of coastline change in the period 1988-2018, the red line represents the coastline in 1988 [3]

If the different observations and the knowledge about the 2.longshore current are combined, figure 6.6 can be made. The possible future development of the tidal delta and the adjacent coastline may be predicted. If the coastline is considered from east to west a longshore current can be distinguished. This longshore current is also directed from east to west and transports sediment. On the eastern side of the Puerto Real inlet the adjacent coastline is showing a small retreat of the coastline over time. At the Puerto Real inlet a decrease of the flood tidal delta is observed. This means that longshore currents are transporting more sediment in western direction after the Puerto Real inlet. Between the Puerto Real inlet and the Carmen inlet the coast line is stable. The artifical beach widening of Ciudad del Carmen should not be taken into account in the natural sediment transport. The western part of the lagoon imports sediment. This results in erosion of the adjacent coast line in western direction of the Carmen inlet. This beach widening and the erosion on the western side of the Carmen inlet can be seen in figure 6.5. What is striking, is that sediment transport at the tidal inlets is in opposite direction of the residual current. This also contradicts the sediment distribution study (section 5.5). Thus, to get a good prediction of future morphological changes near Terminos Lagoon, future research is required, especially on the sediment transport near the Carmen inlet.
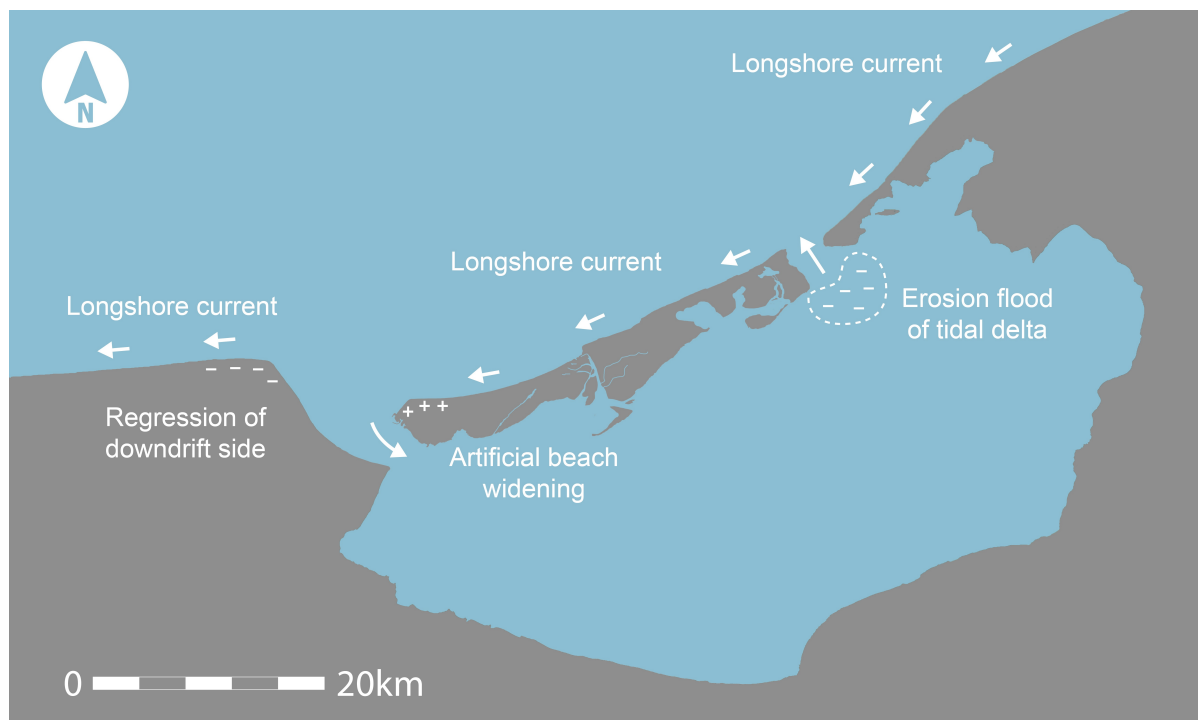
Figure 6.6: Morphological changes of the adjacent coast line and the tidal delta

6.3. Industrial contaminants

Ciudad del Carmen is the gateway to the oil reserves just off the coast. This oil exploitation can pose a major pollution threat to the ecological stability of Terminos Lagoon. One of the biggest oil spills ever recorded, Ixtoc I in 1979, is a testimony to this fact as it had great impact on the local biodiversity around Terminos Lagoon [50, 58]. However, the amount of pollution that can be traced back to the oil industry remains unclear. Next to that, similar pollutants to those from oil industry activity reach the lagoon from rivers upstream [45, 58]. As measurable indicator of industry's effect on the environment, often is looked at trace metals [37, 43], which can move up the food chain for negative effects [39].

Looking at the trace metal measurements, collected a year after the oil spill in 1979, it seems that most pollution in the lagoon comes from the river systems [45]. The Palizada river contributes most to this pollution, with highest particulate trace metal concentrations. Páez-Osuna (1987) also notices that the sea shelf near the Carmen inlet might be influenced from trace metals from upstream. Upstream from the Palizada river, there are industries present, most likely responsible for the pollution. The environmental risk due to upstream industry can thus be regarded as high in the western part of the lagoon, but lower in the eastern areas

of the lagoon.

Most industrial contaminants in Terminos Lagoon originate from the Palizada river. Heavy metal particles released by industries are mostly bigger and heavier than sediments carried by the river system. These particles also reflect sunlight, so contaminant might affect Secchi depth, though unclear is by which margin. The particles will follow the dominant current, which flows from the river mouth through the Carmen inlet, see figure 4.16. More upstream industrial activity will most likely lower local Secchi depth. It will harm the ecosystem of the western part of Terminos Lagoon main basin the most, because of aforementioned reasons.

Increase in offshore oil-industry activity might affect Terminos Lagoon as well. Contaminants most likely enter the lagoon through the Puerto Real inlet. Areas affected most are the places where the residual current is directed to, starting at the Puerto Real inlet. This is close to the boundaries of the lagoon and the middle of the eastern part of the lagoon, where a circular current is present. Contamination entering through the Puerto Real inlet reaches a larger area of the lagoon than contamination entering through the Palizada river due to this circular current. It likely also gets relatively more dispersed.

7

Conclusion

Terminos Lagoon is an important ecosystem, locally and regionally. The lagoon is prone to change, which might harm the local ecosystem. To better protect the area, knowledge is required on hydrodynamic and hydrological processes, and their relation to spatial characteristics of the lagoon. To this end, data sources with different temporal and spatial scales are analysed and compared, taking seasonal differences and potential future developments into account. In this chapter sub-questions are answered to give an answer on the main question: 'What is the influence of hydrological and hydrodynamic processes on spatial characteristics of Terminos Lagoon, now and in the future?'

A water balance is made by examining hydrological processes. From the inputs of the water balance, it is concluded that the largest input of fresh water is the Palizada river. According to the results of the Penman method, yearly average evaporation is about one third more than annual precipitation. It is found that the groundwater flow is negligible small and therefore the inflow of Terminos lagoon is determined by the precipitation and river flow. Nortes and rainy season show a water balance similar to the mean water balance. During dry season evaporation plays a relatively bigger role, being in the same order of magnitude as the discharge of the rivers in this season.

The distribution of the spatial characteristics is investigated. According to the results of a Delft3D-FLOW model, the salinity is higher in the eastern part of the lagoon than the western part. However, the field measurements show smaller differences between the measurements of the Palizada and Candelaria campaign. A reason for these differences in salinity is that only the Palizada river was modelled in Delft3D, while there are more sources of freshwater input. From top of atmosphere brightness temperature maps, is concluded that the water temperature is higher close to land surfaces and generally higher in the main basin than at sea. The western part of the lagoon has often a higher water temperature than the eastern part of the lagoon. Field measurements showed that the east side of the lagoon has lower dissolved oxygen concentrations than the west side of the lagoon. The Secchi depth increases from the river to the inlet, from where the Secchi depth drops again in the direction of the Gulf of Mexico. The east and centre of the lagoon have clearer water than the west of the lagoon. River deposits seem to accumulate more light-reflecting particles in the west. The sediments in the western part of the lagoon have a wider range in grain size than the eastern part, due to the river deposits of the Palizada.

It is investigated how hydrodynamic processes are visible in the distribution of the spatial characteristics. A Delft3D-FLOW model gave reason to expect a circular residual current in the eastern lagoon. Based on this current the lagoon can be split in two parts. The eastern part shows a circular residual current. The western side shows a residual current which follows the boundaries of the lagoon from east to west. The Palizada river has a strong influence on the residual currents near its river mouth. The tidal watershed divides the lagoon in two equal areas which are more or less in line with the areas of the residual currents. The same division of the lagoon was observed in the distribution of the spatial characteristics. The Secchi depth and the top of atmosphere brightness temperature follow the residual currents during flood. The calculated Secchi depths show also that the regions with a lower residual current are less turbid. This confirms the modelled direction of the residual current. The effect of the river inflow in the lagoon could be recognised in the Secchi depth and the water temperature. The river discharge contains suspended sediments, which is visible in

Secchi depth patterns. Moreover, the water from the river transports heat from the land to the water in the lagoon, along similar patterns. This also confirms the direction of the residual current. Secchi depth and temperature distribution show strong tidal dependencies. During ebb water flows out of the lagoon, lowering Secchi depth and showing a clear seaward pattern of water temperature. During flood, the lower Secchi depth and deviating temperatures flow into the lagoon, mainly follow the residual currents.

Seasonal variations are observed in the spatial characteristics as they show variation throughout the year. During the Nortes season the salinity is the lowest, during the dry season the highest. The temperature difference between west and east follows the boundary of the tidal watershed during Nortes. The lagoon is significantly less turbid during Nortes than other seasons. Conclusions about the seasonal differences in dissolved oxygen and sediment distribution could not be drawn.

The statistical dependence between the hydrological processes and spatial characteristics is investigated by the application of a Bayesian network. The considered hydrological processes were river discharge, evaporation, precipitation and atmospheric temperature. The considered spatial characteristics were water temperature and salinity. The largest correlation is found between the atmospheric temperature and water temperature with a positive correlation of 0.779. Furthermore, the salinity is mostly affected by the river discharge of the Palizada river. A negative correlation coefficient of -0.732 is found. The evaporation and precipitation showed low correlations with the spatial characteristics.

Effects of climate change could include a temperature increase, sea level increase and a change in precipitation rate. Increased air temperatures can lead to increased water temperature and evaporation rates. This is likely to become most apparent in the eastern part of the lagoon. The direct effects of a higher air temperature will be most noticeable during dry season. A sea level rise causes more sedimentation at tidal inlets and higher Secchi depths. The flushing time is expected to decrease in this case. Locally, the sea level rise does not have significant impact on the water balance. A change in precipitation rate will influence the input of fresh water in the lagoon. As the rivers emerging in the lagoon are positively correlated with precipitation, river flow is likely to change as well. Due to these changes the net flow through the inlets changes. An increase in precipitation will lead to a relatively higher net flow trough the inlets. The opposite applies for a decrease in precipitation rate. The increase in fresh water influx to the lagoon most likely reduces the salinity of the lagoon.

Looking at the evolution of the adjacent coastline and the flood tidal delta over the last 30 years, a prediction of the future development of the adjacent coastline and the flood tidal delta can be made. From east to west the following changes can be expected: retreat of the adjacent coastline east from the Puerto Real inlet, erosion of the flood tidal delta at the Puerto Real inlet and erosion of the adjacent coastline west from the Carmen inlet. Besides the adjacent coastline and the flood tidal delta also the inlets will develop. At this moment the inlets are not stable and they will move to an equilibrium. To decrease the cross sectional area of the inlets and reach a natural equilibrium, both inlets will sedimentate.

Most industrial contaminants originate from the rivers that enter the lagoon, especially the Palizada river. Industrial contaminants can negatively effect the Secchi depth and harm the ecosystem of mainly the western part of the lagoon. Oil industry can cause major pollution in the Gulf of Mexico, although the specific effects on Terminos Lagoon are unsure. Most likely the contaminants will follow the residual current, flowing from the Puerto Real inlet to the eastern and middle part of Terminos Lagoon.

8
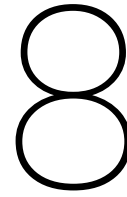
Recommendations

In this report the influence of hydrological and hydrodynamic processes on spatial characteristics are investigated using fieldwork measurements, a Delft3D-FLOW model, measurement stations and satellite imagery. The results of the fieldwork campaigns are compared with the Delft3D-FLOW model and satellite imagery studies where possible, to achieve more reliable results. Further research is needed to validate and expand these results in order to protect the lagoon. In further research, models should be optimized, as well as the measurement campaigns.

Delft3D-FLOW is used to determine the residual current direction. The current direction can be verified with GPS trackers or with dye tracing. With GPS trackers, the water flow of the surface can be determined and with dye tracing the water flow of the total water column can be investigated. These measurements can be performed in, for example, the river outlets and at tidal inlet system. Results can be used to validate flow models.

The greatest discrepancy between fieldwork measurements and Delft3D-FLOW model, are the salinity distribution in the eastern lagoon. This could be due to the Chumpan, Candelaria and Mamentel river discharges, which are not taken into account in Delft3D models to lower computational effort. Moreover, some input parameters are taken as constant in the Delft3D-FLOW model, while these are not constant in the real situation. The model needs to be optimized after comparing the results with field measurement data. A Delft3D flexible mesh could be used for this optimization. With a flexible mesh, the grid size can be decreased in areas where more details are required, for instance the inlets. On the other hand, grid sizes can be increased in less interesting areas, the Gulf of Mexico for example. A Delft3D flexible mesh model could decrease the model runtime, which makes it possible to run more models in a shorter time, to add more rivers to the model or look more upstream on the river.

Field measurements and sample testing can be used to validate the Delft3D-FLOW model. Slight changes in measurement methodology might improve reliability of the field measurements. First, preferably the campaigns should be scheduled during a satellite overpass. This can improve the use of satellite imagery to look into a variety of characteristics. Overpass dates can be predicted for landsat, for example, by using the prediction calendar [64]. Furthermore, sediment sieving tests are recommended to look into sediment distribution over time in Terminos Lagoon. Last, with the current measurement locations little information is gained in the center of the lagoon. Collecting samples in this area will increase the knowledge on hydrological and hydrodynamic processes and distribution of spatial characteristics in Terminos Lagoon.

While a complete water balance is created, it is based on the assumption that groundwater flow is negligible and net flow through tidal inlets equals the "gap" in between estimated in- and output to Terminos Lagoon. Preferably, these are measured as well to improve the accuracy of the water balance. Near both tidal inlets ADCP (Acoustic Doppler Current Profiler) measurements could be performed to get insight into flow velocities through the inlets. Moreover, the rate of return could be determined in order to define the flushing time of the lagoon. Next, similar ADCP measurements could be performed in the four largest discharging rivers. Preferably measurements should be repeated monthly. In order to get a view of groundwater flow, the surrounding area can be obtained by performing an extensive fieldwork campaign, installing piezometers over a regular grid surrounding Terminos Lagoon and sampling testing to obtain the hydraulic conductivity. Other

uncertainties include the assumption that evaporation and precipitation are equal over the whole lagoon. These uncertainties can be reduced by setting up weather stations in and around the lagoon, near the Palizada and Candelaria river outlets for example. This can increase the accuracy of the spatial distribution of parameters over the lagoon.

The determined correlations between hydrological processes and spatial characteristics are useful in objectively finding relations between varying parameters in a given region. Main obstacle in finding more accurate correlations between parameters, are gaps in datasets. Some parameters had lasting corresponding timeseries of data, while other corresponding timeseries were relatively short. Second, found correlations are expected to differ from reality, as they are not all measured at the same location. Recommended is to keep running the current measurement stations, in order to expand existing timeseries. If possible, a measurement device could be installed at the east side of the lagoon, to get a more comprehensive view of statistical correlations between hydrological processes, hydrodynamic processes and spatial characteristics of the whole lagoon.

Morphology of Isla del Carmen will change in the future, though contradictory processes have been observed. Future research is required to get insight in these processes. Possible additional research could be done on the future morphological developments of the island, the currents and tides present near the Carmen inlet, or a wave model for the lagoon could be created.

9

Acknowledgments

We would like to thank the partial financial support for field campaigns and sensors from the research project:

Bibliography

[1] Catálogo localidades. `http://www.microrregiones.gob.mx/catloc/LocdeMun.aspx?tipo=clave&campo=loc&ent=04&mun=003`. Accessed: 2018-09-28.

[2] Fundamentals of environmental measurements; dissolved oxygen. `https://www.fondriest.com/environmental-measurements/parameters/water-quality/dissolved-oxygen/`. Accessed: 2018-09-28.

[3] Google earth engine. `https://earthengine.google.com/timelapse/`. Accessed: 2018-09-27.

[4] What are the band designations for the landsat satellites? `https://www.usgs.gov/faqs/what-are-band-designations-landsat-satellites-0?qt-news_science_products=7#qt-news_science_products,`. Accessed: 2018-09-13.

[5] Landsat 8 data users handbook - section 5. `https://landsat.usgs.gov/landsat-8-l8-data-users-handbook-section-5/,`. Accessed: 2018-09-18.

[6] What is a box plot? `https://docs.tibco.com/pub/spotfire/6.5.1/doc/html/box/box_what_is_a_box_plot.htm`, September 2014. Accessed: 2018-10-16.

[7] Mexican president pledges to boost country's oil and gas sectors. `https://www.publicfinanceinternational.org/news/2018/07/mexican-president-pledges-boost-countrys-oil-and-gas-sectors`, 2018. Accessed: 2018-09-24.

[8] Dan Ababei. Uninet lighttwist, December 2018. URL `http://www.lighttwist.net`. Accessed: 2018-10-10.

[9] I.M. Abascal-Monroy, M. J. Zetina-Rejón, F. Escobar-Toledo, G.A. López-Ibarra, A. Sosa-López, and A. Tripp-Valdez. Functional and structural food web comparison of terminos lagoon, mexico in three periods (1980, 1998, and 2011). *Estuaries and Coasts*, 39(4):1282–1293, 2016.

[10] K. Alikas and S. Kratzer. Improved retrieval of secchi depth for optically-complex waters using remote sensing data. *Ecological Indicators*, 77:218–227, 2017.

[11] J. R. Allen. A review of the origin and characteristics of recent alluvial sediments. *Sedimentology*, 5(2):89–191, 1965.

[12] E. B. Barbier and I. Strand. Valuing mangrove-fishery linkages–a case study of campeche, mexico. *Environmental and Resource Economics*, 12(2):151–166, 1998.

[13] F. Bautista, G. Palacio-Aponte, P. Quintana, and J. A. Zinck. Spatial distribution and development of soils in tropical karst areas from the peninsula of yucatan, mexico. *Geomorphology*, 135(3-4):308–321, 2011.

[14] J. Bosboom and M.J.F. Stive. *Coastal Dynamics I: lecture notes CIE4305*. Delft University of Technology, Delft, The Netherlands, 2015.

[15] K.F. Bowden. *Physical Oceanography of Coastal Waters*. 01 1983.

[16] A. Carranza-Edwards, L. Rosales-Hoz, and A. Monreal-Gómez. Suspended sediments in the southeastern gulf of mexico. *Marine Geology*, 112(1-4):257–269, 1993.

[17] E. Y. Chan. Climate change is the world's greatest threat - in celsius or fahrenheit? *Journal of Environmental Psychology*, 2018.

[18] J. Cohen. A coefficient of agreement for nominal scales. *Educational and psychological measurement*, 20(1):37–46, 1960.

[19] R.G. Congalton. A review of assessing the accuracy of classifications of remotely sensed data. *Remote sensing of environment*, 37(1):35–46, 1991.

[20] L.T. David and B. Kjerfve. Tides and currents in a two-inlet coastal lagoon: Laguna de terminos, mexico. *Continental Shelf Research*, 18:1057–1079, 1998.

[21] NASA earth observatory. Laguna de terminos. `https://earthobservatory.nasa.gov/images/90893/laguna-de-terminos`, 01 2017. Accessed: 2018-09-03.

[22] F.F. Escoffier. The stabilitiy of tidal inlets. *Shore Beach*, 8:114–115, 1940.

[23] A.C.R. Esparza, P. Douillet, and J. Zavala-Hidalgo. Tidal dynamics of the terminos lagoon, mexico: observations and 3d numerical modelling. *Ocean Dynamics*, 64(9):1349–1371, 2014.

[24] N.P. Fofonoff and R.C. Millard. Algorithms for the computation of fundamental properties of seawater. *Unesco technical papers in marine science*, 1983.

[25] Harte Research Institute for Gulf of Mexico Studies. Términos lagoon. `https://www.gulfbase.org/geological-feature/terminos-lagoon`, 2018. Accessed: 2018-10-09.

[26] J.J. Guerra-Santos and J.D.W. Kahl. Redefining the seasons in the terminos lagoon region of southeastern mexico: May is a transition month, not a dry month. *Journal of Coastal Research*, 34(1):193—-201, 2018.

[27] F. N. Güttler, S. Niculescu, and F. Gohin. Turbidity retrieval and monitoring of danube delta waters using multi-sensor optical remote sensing data: An integrated view from the delta plain lakes to the western–northwestern black sea coastal zone. *Remote Sensing of Environment*, 132:86–101, 2013.

[28] D. E. Hinkle, W. Wiersma, and S. G. Jurs. Applied statistics for the behavioral sciences. 1988.

[29] Penman H.L. Natural evaporation from open water, bare soil and grass. *Proc. R. Soc. Lond. A*, 193(1032):120–145, 1948.

[30] INEGI. Mapa edafológico 1:250,000 ciudad del carmen e15-6 inegi., 2007. data retrieved from INEGI, `http://www.beta.inegi.org.mx/temas/mapas/edafologia/#`.

[31] IOCCG. Software for ocean-colour algorithms. `http://www.ioccg.org/groups/software.html`, 2015. Accessed: 2018-10-05.

[32] S.N. Jonkman, R.D.J.M. Steenbergen, O. Morales-Nápoles, A.C.W.M. Vrouwenvelder, and J.K. Vrijling. *Probabilistic Design: Risk and Reliability Analysis in Civil Engineering*. TUDelft, Delft, The Netherlands, 2017.

[33] B. Kirtman, S.B. Power, J.A. Adedoyin, G.J. Boer, R. Bojariu, I. Camilloni, F.J. Doblas-Reyes, A.M. Fiore, M. Kimoto, G.A. Meehl, M. Prather, A. Sarr, C. Schär, R. Sutton, G.J. van Oldenborgh, G. Vecchi, and H.J. Wang. *Near-term Climate Change: Projections and Predictability, In: Climate Change 2013: The Physical Science Basis. Contribution of Working Group I to the Fifth Assessment Report of the Intergovernmental Panel on Climate Change*. Cambridge University Press, Cambridge, United Kingdom and New York, NY, USA, 2013.

[34] A.A. Lamaro, A. Marinelarena, S.E. Torrusio, and S.E. Sala. Water surface temperature estimation from landsat 7 etm+ thermal infrared data using the generalized single-channel method: Case study of embalse del río tercero (córdoba, argentina). *Advances in Space Research*, 51(3):492–500, 2013.

[35] Z. Lee, K.L. Carder, and R.A. Arnone. Deriving inherent optical properties from water color: a multiband quasi-analytical algorithm for optically deep waters. *Applied optics*, 41(27):5755–5772, 2002.

[36] Z. Lee, S. Shang, L. Qi, J. Yan, and G. Lin. A semi-analytical scheme to estimate secchi-disk depth from landsat-8 measurements. *Remote sensing of environment*, 177:101–106, 2016.

[37] Z. Liu, J. Liu, Q. Zhu, and W. Wu. The weathering of oil after the deepwater horizon oil spill: insights from the chemical composition of the oil from the sea surface, salt marshes and sediments. *Environmental Research Letters*, 7(3):035302, 2012.

[38] S. Manickchand-Heileman, F. Arreguín-Sánchez, A. Lara-Domínguez, and L.A. Soto. Energy flow and network analysis of terminos lagoon, sw gulf of mexico. *Journal of Fish Biology*, 53:179–197, 1998.

[39] M. Mendoza-Carranza, A. Sepúlveda-Lozada, C. Dias-Ferreira, and V. Geissen. Distribution and bioconcentration of heavy metals in a tropical aquatic food web: A case study of a tropical estuarine lagoon in se mexico. *Environmental Pollution*, 210:155–165, 2016.

[40] N.E. Monsen, J.E. Cloern, L.V. Lucas, and S.G. Monismith. A comment on the use of flushing time, residence time, and age as transport time scales. *Limnology and oceanography*, 47(5):1545–1553, 2002.

[41] Gulf of Mexico Hypoxia. Hypoxia. `https://gulfhypoxia.net/about-hypoxia/`, 2018. Accessed: 23-10-2018.

[42] University of Sussex. Table of critical values for pearson's. `http://users.sussex.ac.uk/~grahamh/RM1web/Pearsonstable.pdf`. Accessed: 2018-11-30.

[43] L.C. Osuji and C.M. Onojake. Trace heavy metals associated with crude oil: A case study of ebocha-8 oil-spill-polluted site in niger delta, nigeria. *Chemistry & biodiversity*, 1(11):1708–1715, 2004.

[44] F. B. Phleger and A. Ayala-Castanares. Processes and history of terminos lagoon, mexico. *AAPG Bulletin*, 55(12):2130–2140, 1971.

[45] F. Páez-Osuna, D.S. Valdez-Lozano, H.M. Alexander, and H. Fernández-Pérez. Trace metals in the fluvial system of terminos lagoon, mexico. *Marine Pollution Bulletin*, 18(6):294–297, 1987.

[46] J. Ramos-Miranda, L. Quiniou, D. Flores-Hernandez, T. Do-Chi, L. Ayala-Perez, and A. Sosa-Lopez. Spatial and temporal changes in the nekton of the terminos lagoon, campeche, mexico. *Journal of Fish Biology*, 66(2):513–530, 2005.

[47] D. Robadue Jr, A. Oczkowski, R. Calderon, L. Bach, and M. Cepeda. Managing freshwater inflows to estuaries. *Narragansett, Rhode Island: Coastal Resources Center, University of Rhode Island*, 2004.

[48] T. Rodrigues, E. Alcântara, F. Watanabe, and N. Imai. Retrieval of secchi disk depth from a reservoir using a semi-analytical scheme. *Remote Sensing of Environment*, 198:213–228, 2017.

[49] J.D. Rodriguez, A. Perez, and J.A. Lozano. Sensitivity analysis of k-fold cross validation in prediction error estimation. *IEEE transactions on pattern analysis and machine intelligence*, 32(3):569–575, 2010.

[50] M.C. Rosano-Hernández, H. Ramírez-Saad, and L. Fernández-Linares. Petroleum-influenced beach sediments of the campeche bank, mexico: diversity and bacterial community structure assessment. *Journal of environmental management*, 95:S325–S331, 2012.

[51] D. A. Salas-de León, M. A. Monreal-Gómez, D. Salas-Monreal, G. Expósito-Díaz, M. L. Riverón-Enzastiga, and F. Vázquez-Gutiérrez. Tidal current components in the southern bay of campeche, gulf of mexico. *Geofísica internacional*, 46(2):141–147, 2007.

[52] H.H.G. Savenije. *Hydrologie I*. Delft University of Technology, Delft, The Netherlands, 2014.

[53] SEMAR. S. m. 842.3, laguna de terminos, camp. entrada este., 1:20,000, 2008. data retrieved from SEMAR, `https://digaohm.semar.gob.mx/hidrografia/imagenesHidrografia/catalogo%202018.pdf`.

[54] SEMAR. S. m. 842.2, laguna de terminos, camp. entrada oeste., 1:20,000, 2013. data retrieved from SEMAR, `https://digaohm.semar.gob.mx/hidrografia/imagenesHidrografia/catalogo%202018.pdf`.

[55] SEMAR. S. m. 842, laguna pom a santa cruz, 1:100,000, 2016. data retrieved from SEMAR, `https://digaohm.semar.gob.mx/hidrografia/imagenesHidrografia/catalogo%202018.pdf`.

[56] SEMAR. S. m. 842.1, laguna de terminos, camp. y prox., 1:60,000, 2016. data retrieved from SEMAR, `https://digaohm.semar.gob.mx/hidrografia/imagenesHidrografia/catalogo%202018.pdf`.

[57] S. V. Smith, J. M. Crossland, and C. J. Crossland. *Mexican and central American coastal lagoon systems: carbon, nitrogen and phosphorus fluxes (regional workshop II)*. LOICZ International Project Office, Netherlands Institute for Sea Research, 1999.

[58] L.A. Soto, A.V. Botello, S. Licea-Durán, M.L. Lizárraga-Partida, and A. Yáñez-Arancibia. The environmental legacy of the ixtoc-i oil spill in campeche sound, southwestern gulf of mexico. *Frontiers in Marine Science*, 1:57, 2014.

[59] E. Soto-Galera, J. Piera, and P. López. Spatial and temporal land cover changes in terminos lagoon reserve, mexico. *Revista de Biología Tropical*, 58(2):565–575, 2010.

[60] O. Spaargaren. Major soils of the world. *Wageninen, The Netherlands: International Soil Reference and Information Centre*, 2001.

[61] V.U. Thi and T.H.U. Thuy. Aspects of inlet geometry and dynamics. 2013.

[62] M. Tomczak. Seawater density calculator. `https://www.mt-oceanography.info/Utilities/density.html`, 2000. Accessed: 2018-09-24.

[63] J. Urrutia-Fucugauchi, A. Camargo-Zanoguera, L. Pérez-Cruz, and G. Pérez-Cruz. The chicxulub multiring impact crater, yucatan carbonate platform, gulf of mexico. *Geofísica internacional*, 50(1):99–127, 2011.

[64] USGS. Landsat acquisition tool, December 2018. URL `https://landsat.usgs.gov/landsat_acq#acquisitionCalendar`. Accessed: 2018-11-30.

[65] Ministerie van Verkeer en Waterstaat. *Jaaroverzicht van het weer in Nederland*. KNMI, The Netherlands, 2017.

[66] Q. Vanhellemont and K. Ruddick. Turbid wakes associated with offshore wind turbines observed with landsat 8. *Remote Sensing of Environment*, 145:105–115, 2014.

[67] A. Verruijt. *Soil Mechanics*. Vssd, Delft, The Netherlands, 2012.

[68] Z.B. Wang, J. Vroom, B.C. van Prooijen, R.J. Labeur, M.J.F. Stive, and M.H.P. Hansen. Development of tidal watersheds in the wadden sea. In *RCEM 2011: Proceedings of the 7th IAHR Symposium of River, Coastal and Estuarine Morphodynamics, Beijing, China, 6-8 September 2011*. Tsinghua University Press, 2011.

[69] Deutscher Wetterdienst. Global station data 1961–1990. URL `http://w3techs.com/technologies/overview/content_language/all`. Accessed: 2018-09-21.

[70] S. H. Worthington, D. C. Ford, and P. A. Beddows. Porosity and permeability enhancement in unconfined carbonate aquifers as a result of dissolution. In *SPELEO Brazil 2001-13th International Congress of Speleology*, 2001.

[71] A. Yanez and J. Day. Ecological characterization of terminos lagoon, a tropical estuarine–lagoon system in the southern gulf of mexico. *Oceanologica Acta*, 5(4):431–440, 1982.

A
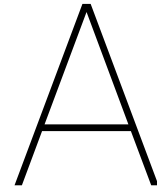
Area and volume Terminos Lagoon

The area of Terminos Lagoon needs to be known to determine a water balance. The total surface area also is required to determine how much water flows in and out of the lagoon due to tidal forces. Then two definitions are required, as within the water balance river outlets are considered boundary conditions of the main basin, while a different area is considered influenced by tides. Other work has shown to use variable surface areas for the lagoon. According to David & Kjerfe (1997), the lagoon has a surface area of 2500 km^2, while Ramos-Miranda et al. (2005) used a surface area of 1661 km^2 for the lagoon main basin. The discrepancies between studies encountered forced to redefine the surface areas required.

Determining both surface areas of the lagoon is done by land classification. Classification methodology is similar to the methodology described by Soto-Galera et al. (2010), except images were not pre-classified. This is not required as here no spatio-temporal relation is sought for. To distinguish between land and water, GRASS 7.4.0 and a Landsat 8 imagery is used. Landsat 8 imagery is selected as it is easily accessible, the spatial resolution is moderate and comparable available imagery extends over 30 years back. This last feature can be useful in future research, if the past morphological changes of the lagoon would be investigated using satellite imagery. The moderate spatial resolution of 30x30 meter [4] is good to obtain a good estimate of the surface areas of the different water bodies. The image selected, overpass at April 13 2018, is chosen for its nearly zero cloud cover and relatively recent collection time. As water bodies are to be found, band 3, band 4 and band 5 are used, corresponding to green, red and near-infra red (NIR) bands. Using the NIR band is beneficial, as classification is often more accurate and water bodies can be observed far easier using NIR. A comparison between the visible spectrum and NIR is shown in figure A.1. Training classes are made by hand, thus using the NIR band is crucial in accurately defining borders between land and water in the more murky waters. Jensen (1989) shows that in some cases using a NIR band instead of a blue band can be more beneficial than using both.
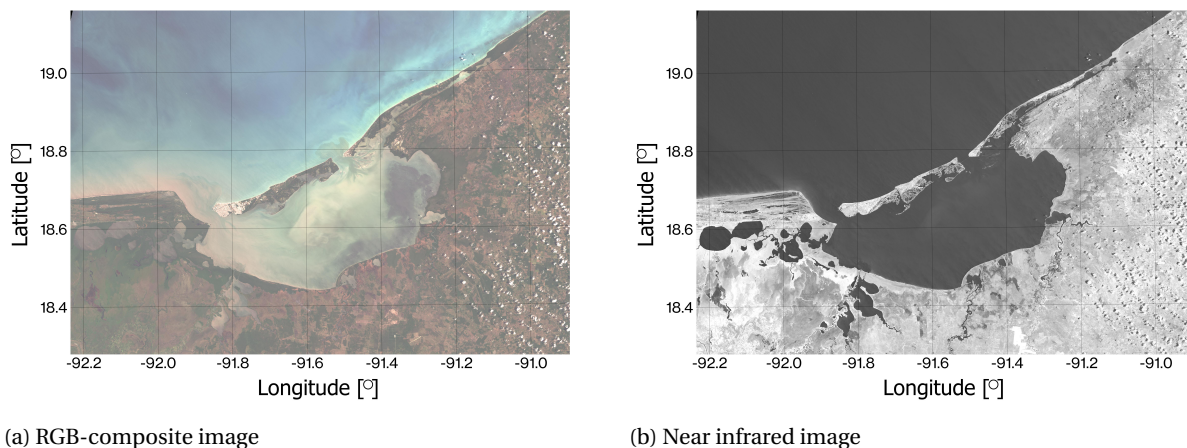

(a) RGB-composite image

(b) Near infrared image

Figure A.1: Visual and NIR spectrum in Terminos Lagoon, 13-04-2018

A.1. Classification

130 training camps are created using in-field experience on varying parts of the lagoon. The training camps contained 3 different classes: water, land and shallows. Water in mangroves are assumed to be of negligible impact on the total water volumes, hence the choice for no separation of land classes. The shallows class was deemed necessary as it was clear the algorithm classified shallow water as beach more often than not. For each training class spectral signatures are created, which in turn were used in a maximum-likelihood discriminant analysis classifier. The spectral signature of shallow water thus is more similar to that of land than that of water. For both creating the spectral signatures and the classifier, pre-built functions within GRASS are available. The result is depicted in A.2b. It can be seen that in the eastern part of the main body of the lagoon, some irregularities occur. This is due to the combination of clouds and shallows. Of the resulting classification only the water bodies are kept, shallows and water are merged. The Gulf of Mexico is cut off at the most narrow part of both major tidal inlets. To obtain the main basin only, also the smaller, surrounding lagoons are removed. To obtain the tidally influenced parts of the lagoon, the Delft3D modelled surface area is replicated. Resulting surface areas of the lagoon are 1690 km^2 and 1687 km^2, for the main lagoon water body and tidally influenced lagoon respectively. See also A.2c and A.2d. Note that these surface areas are almost the same size.
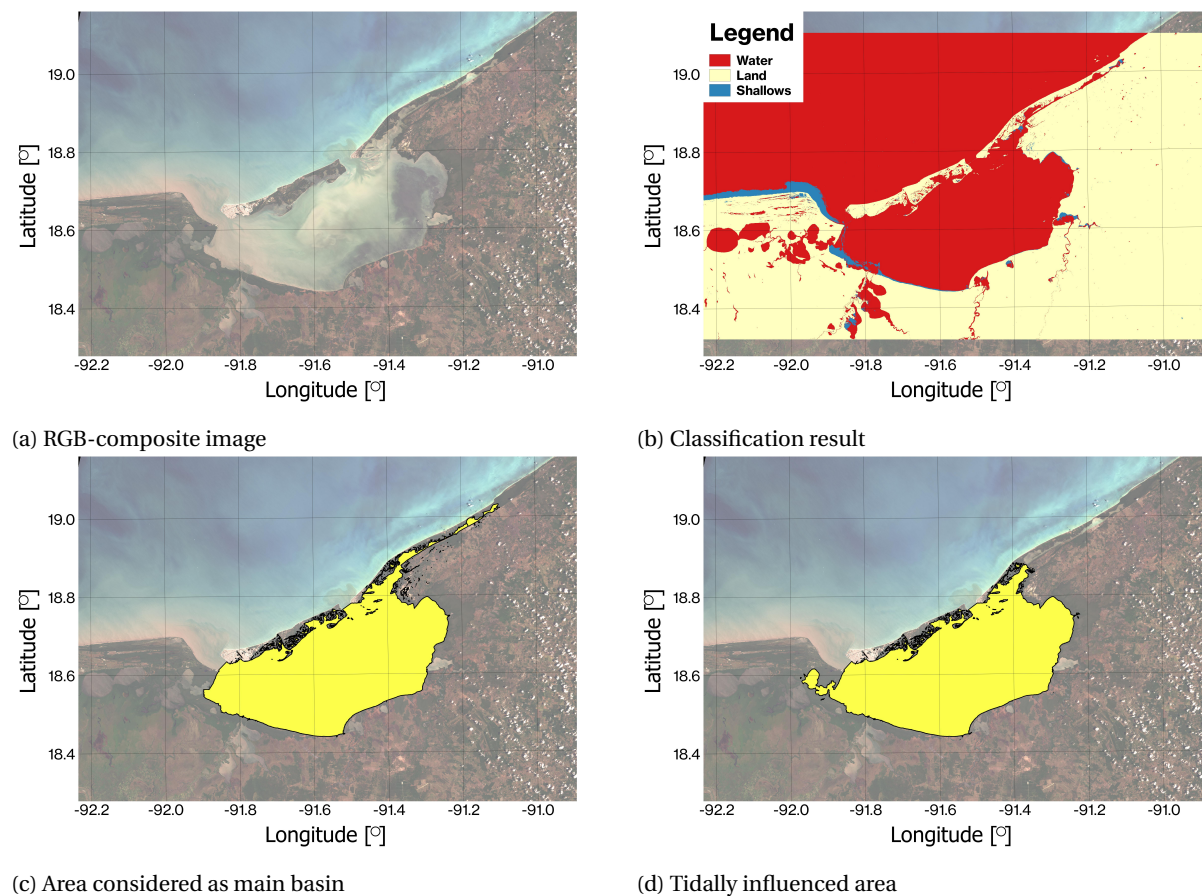

(a) RGB-composite image

(b) Classification result

(c) Area considered as main basin

(d) Tidally influenced area

Figure A.2: Land classification as performed for Terminos Lagoon

A.2. Quality assessment

Quality assessment of the resulting classification is done by a k-fold cross validation of 5. k-fold cross validation of 5 means the training camps are partitioned into 5 equal sizes, of which 4 parts will be used to train the classifier and 1 to validate the newly trained classifier. This process is done with random selection of partitioning 5 times [49]. Thus 5 times a random 20 % of the training camps are used to validate a classifier made using the remainder 80 % of the training camps. Validation of each iteration is done using confusion matrix

and κ index.[19] Accuracy and κ index should be comparable every time, the average gives an indication of accuracy and κ index of the actual classification, which used all of the training camps for training. There is no similar classification exercise done in documented history, hence the choice for this validation method. Advantage of the validation method is that most training camps are used as both for validation and training. The κ index is a measure of agreement or accuracy, which takes into account that truth and prediction can overlap based on chance. It takes on a value between 1 to in between 0 and -1. The higher the κ index, the better the result is compared with a random result. It is defined as follows [18].

$$\kappa = \frac{p_0 - p_e}{1 - p_e} \tag{A.1}$$

With:

p_o = the proportion of units in which the training camps and classification agreed [-]
p_e = the proportion of units for which agreement is expected by chance [-]

Average accuracy and κ index of all iterations are 0.996 and 0.981, respectively. This indicates that classification went well and the result is significantly better than a random result. Note that accuracy is suspiciously high. Reason is probably due to the low number classes and the fact that some training camps were significantly larger than others, while having quite homogeneous spectral signatures. This inflates accuracy and κ index. An individual confusion matrix and κ indices are shown in table A.1 and A.2 respectively. Confusion matrices read as follows: from top to down can be read which training camp is classified as what class. The aim is to determine water outlining, thus the "Water" and "Shallows" classes are taken together.

Table A.1: Confusion matrix of $\kappa 1$, besides accuracy, all numbers are in km^2

	Training Classes - "Truth"		
Classification - "Prediction"	Water	Land	Row totals
Water	33.151	0.300	33.451
Land	0.058	3.999	4.057
Column total	33.210	4.298	37.508
		Accuracy	0.990

Table A.2: Kappa indices per iteration

Iteration	**Accuracy**	**κ index**
1	0.990	0.952
2	1.000	0.992
3	0.996	0.992
4	1.000	0.983
5	1.000	0.987

So, as an example, κ calculation for table A.1 becomes:

$$p_0 = \frac{33.151 + 3.999}{37.508} = 0.990$$

$$p_e = \frac{33.210}{37.508} \cdot \frac{33.451}{37.508} + \frac{4.298}{37.508} \cdot \frac{4.057}{37.508} = 0.790 + 0.012 = 0.802$$

$$\kappa = \frac{0.990 - 0.802}{1 - 0.802} = 0.952$$

Thus in this case kappa index becomes 0.952, which means results are significantly better than a random result.

B

Surface geology

Soil	Qualifiers
Coastal environment	
AR	Calcaric, hypersodic, protic, and hypereutric
RG	Leptic, endogleyic, salic, stagnic, haplic, calcareous, humic, hyposalic, sodic, eutric, skeletal, and arenic.
Fluvio-paludal environment	
SC	Hipersalic, folic histic, vertic, gleyic, stagnic, mollic, calcic and haplic. Secondary qualifiers are: sodic, sandy, siltic, and limic.
GL	Humic, vertic and calcaric
HS	Eutruic, hypereutric, sodic, hypersodic, hyposalic, fibric, and folic
Tectono-karstic environment	
LP	Litic, rendzic and hypereskeletic
NT	Rodic and eutric
Karstic environment	
LP	Nudilitico, litic, rendzic, hyperskeletic, humic, calcaric, chromic and rodico
CM	Leptic, haplic, calcaric, skeletic, rodic and chromic.
LV	Leptic, vertic, haplic, humic, skeletic, rodic and chromic
VR	Endoleptic, salic, gleyic, mollic, gypsyc, calcic, haplic, gypsiric, calcaric and humico

Figure B.1: Surface soil types in Yucatan Peninsula

The soils in the area of Terminos Lagoon are briefly described. Leptosols are shallow soils on calcareous rocks. Cambisols are moderately developed soils, characterized by weathering of the parent material. Geysols are permanently wet and reduced at shallow depth. Solonchak is a salt-affected soil. Refosols are deep mineral soils derived from unconsolidated material and well drained and medium textured. The last present soil is arenosols, which are sandy soils with a slight to moderate profile developement. This description comes from "Major Soils of the World" of O. Spaargaren (2001) [60]. A more extensive description is written in this article.

C

Inlet widths

The change in width of the two major inlets, the Carmen and the Puerto Real inlet, is determined using satellite imagery. To this end, Landsat thematic mapper images are used, as it is the longest comparable time series available. The Landsat thematic mappers have a moderate spatial resolution, 30 meter, and overpasses at an interval of 15 days. [4] The selected images were selected based on quality, cloud cover and collection date. The inlets need both to be visible in the image and the time of year should be about the same every image, as seasonal changes then can be excluded from influencing channel width. There is approximately five years in between images, though this is not always the case due to aforementioned image requirements. The selected images are presented in C.1.

Table C.1: Landsat images used for inlet width determination

Mission	Image collection date
Landsat 4-5 TM	2 April 1988
Landsat 4-5 TM	8 April 1993
Landsat 7	19 April 2000
Landsat 7	11 March 2003
Landsat 7	9 April 2008
Landsat 8	1 March 2014
Landsat 8	28 March 2018

Width is determined by drawing polygons on either side of the channel. Then minimal distance between polygons is calculated using GRASS 7.4.0. Figure C.1 illustrates this method. Resulting inlet widths are presented in figure C.2.

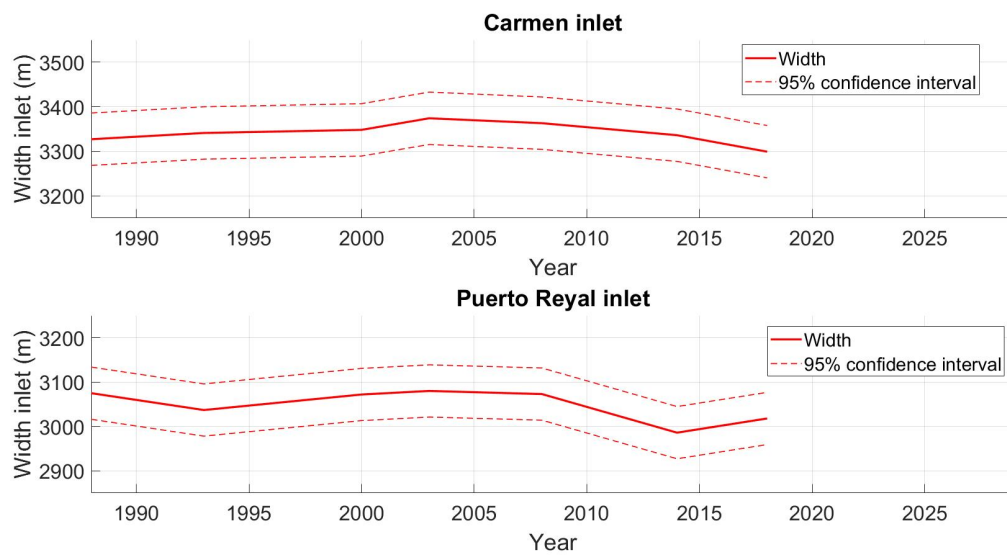Figure C.1: : Polygons on either shore and calculated shortest distance between them

Figure C.2: Major inlet widths over time

D

Temperature distribution

Temperature fluctuations in space and between seasons are looked at using satellite imagery. Landsat 8 has two distinct "thermal" bands in the infra-red spectrum, which can be used to easily obtain top of atmosphere brightness temperature [5, 34]. This temperature can then be used as reference material. It is, however, uncorrected for atmosphere. As in-situ measurements and temperatures as calculated using Landsat data differ, the temperature maps resulting from processing Landsat imagery will not be used as direct temperature measurements. They can, however, be used to look into the spatial patterns of temperature within and near Terminos Lagoon.

Extracting temperature from the Landsat imagery is done as follows.

The Digital Numbers (DN) of band 10 provided by in the raw data are first converted to at-sensor spectral radiance:

$$L = ML \cdot Q + AL \tag{D.1}$$

With:

L	= Spectral radiance	[W/(m$^2 \cdot$ sr $\cdot$ μm)]
ML	= Radiance multiplicative scaling factor for the band	[-]
AL	= Radiance additive scaling factor for the band	[-]
Q	= Pixel value	[DN]

Band 10 is used as thermal band. Now the top of atmosphere brightness temperature can be determined.

$$T = \frac{K_2}{Ln(\frac{K_1}{L_\lambda} + 1)} - 273.15 \tag{D.2}$$

With:

T	= Top of atmosphere brightness temperature	[°C]
L	= Spectral radiance	[W/(m$^2 \cdot$ sr $\cdot$ μm)]
K$_1$	= Thermal conversion constant for the band	[-]
K$_2$	= Thermal conversion constant for the band	[-]

All necessary constants are provided in the meta file, included with the data.
Table D.1 shows the selected acquisition dates for the thermal images shown in figures D.1 to D.15. All images are scaled to show the variation in the basin as good as possible, at maximum there is a difference of three degrees Celsius between white and red. Warmer regions are a deeper color red, colder regions are more white. Table D.1 also shows the standard deviation of the temperature for the main basin. Tides are also shown, to give an indication in what direction flow is expected. For example, At the seventh of January, 2018 the image was collected at "Flood" vertical tide and "Ebb" horizontal tide, indicating peak flood is just surpassed in

horizontal tide. The Semar site is used for tide determination, as it is in the Carmen inlet. As one would expect from expected precipitation patterns, dry season shows the lowest spatial fluctuation in temperature, while rainy season shows most. Influx of more water through rivers seems to cool water in the lagoon during Rainy season. Note that rainy season tends to be very cloudy more often than not, hence the images of rainy season 2016 to 2018 are visibly contaminated, explaining the large deviation in temperature. Rainy season images for 2014 and 2015 are more comparable to other images though, which show higher deviation in temperature as well. In some cases flow patterns can be observed. Most often water near land is the warmest water.

Landsat 8 acquisition date	Corresponding season	σ temperature main basin (°C)	Vertical tide Semar	Horizontal tide Semar
07-01-2018	Nortes	0.175	Flood	Ebb
20-01-2017	Nortes	0.215	Flood	Flood
01-12-2015	Nortes	0.183	Ebb	Ebb
14-12-2014	Nortes	0.019	Flood	Ebb
28-01-2014	Nortes	0.199	Ebb	Flood
13-04-2018	Dry	0.159	Ebb	Flood
10-04-2017	Dry	0.212	Ebb	Ebb
09-05-2016	Dry	0.171	Flood	Ebb
07-05-2015	Dry	0.210	Flood	Flood
01-03-2014	Dry	0.146	Ebb	Ebb
02-07-2018	Rainy	0.670	Flood	Flood
31-07-2017	Rainy	1.618	Flood	Flood
12-07-2016	Rainy	0.834	Flood	Flood
26-07-2015	Rainy	0.238	Flood	Flood
08-08-2014	Rainy	0.380	Flood	Flood

Table D.1: Acquisition dates and corresponding seasons Landsat 8 thermal imagery
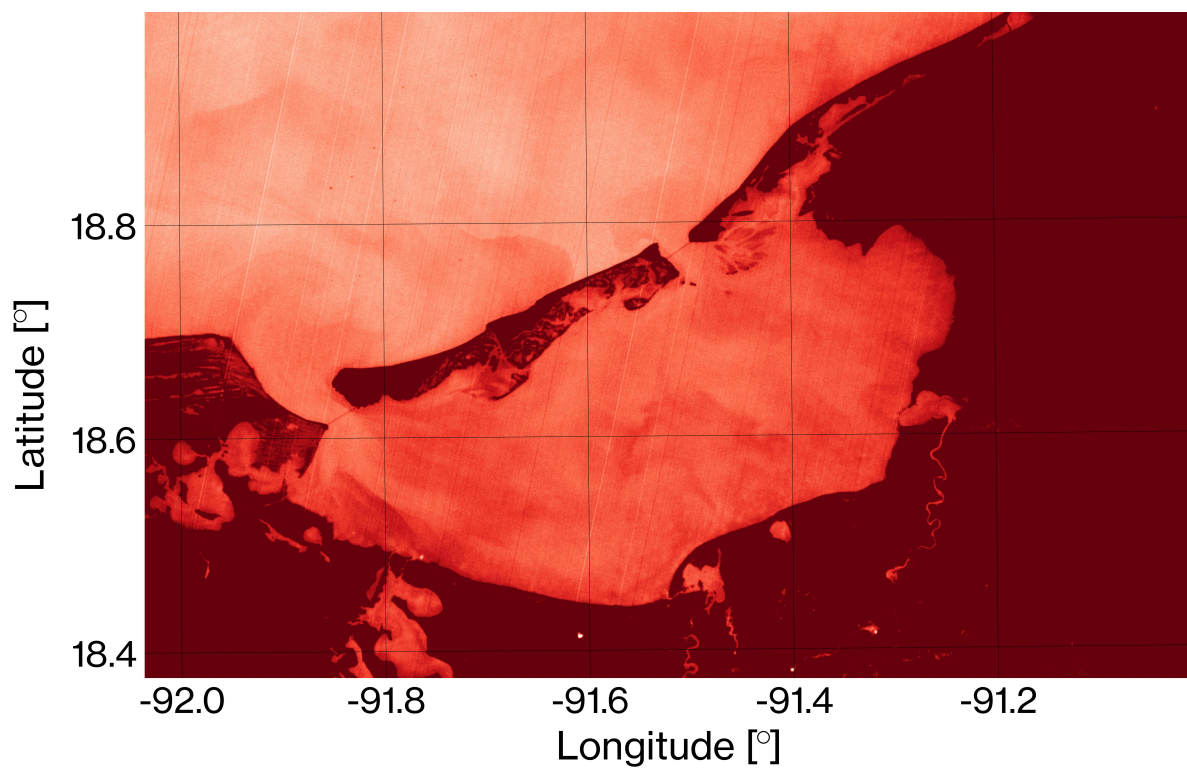
Figure D.1: Relative temperature in Terminos Lagoon, 01-03-2014 (Dry season)
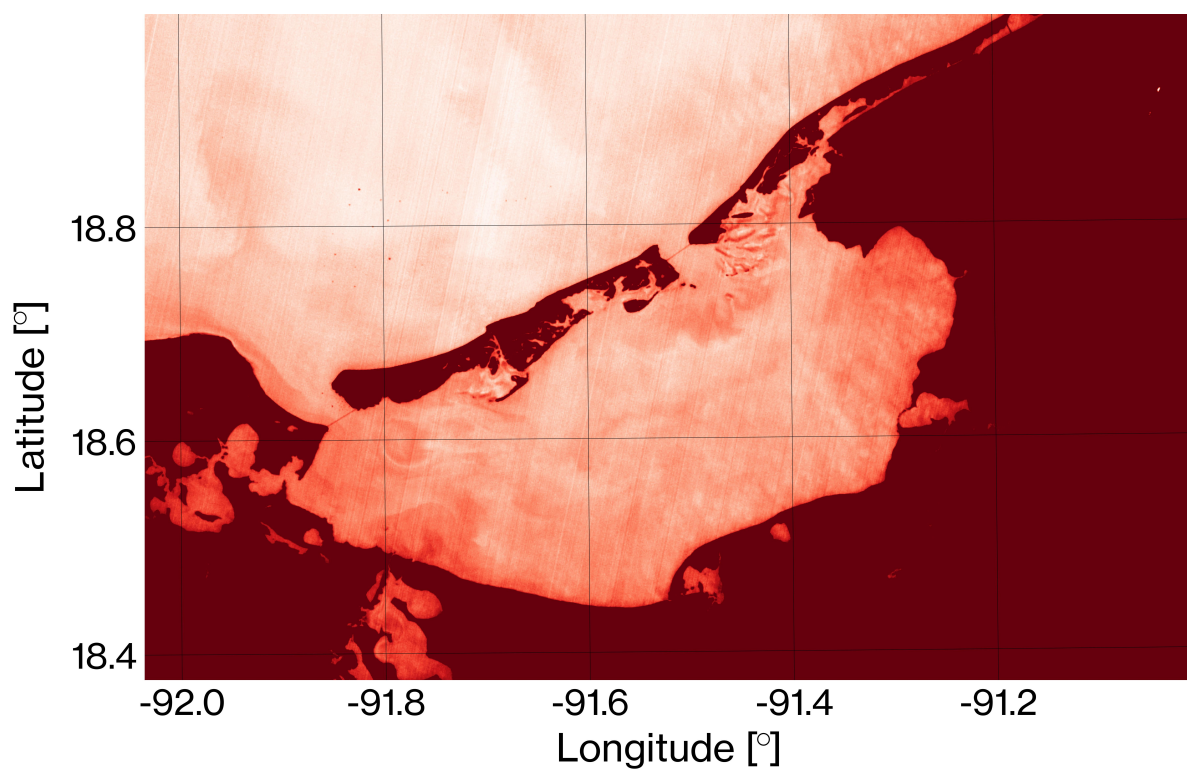
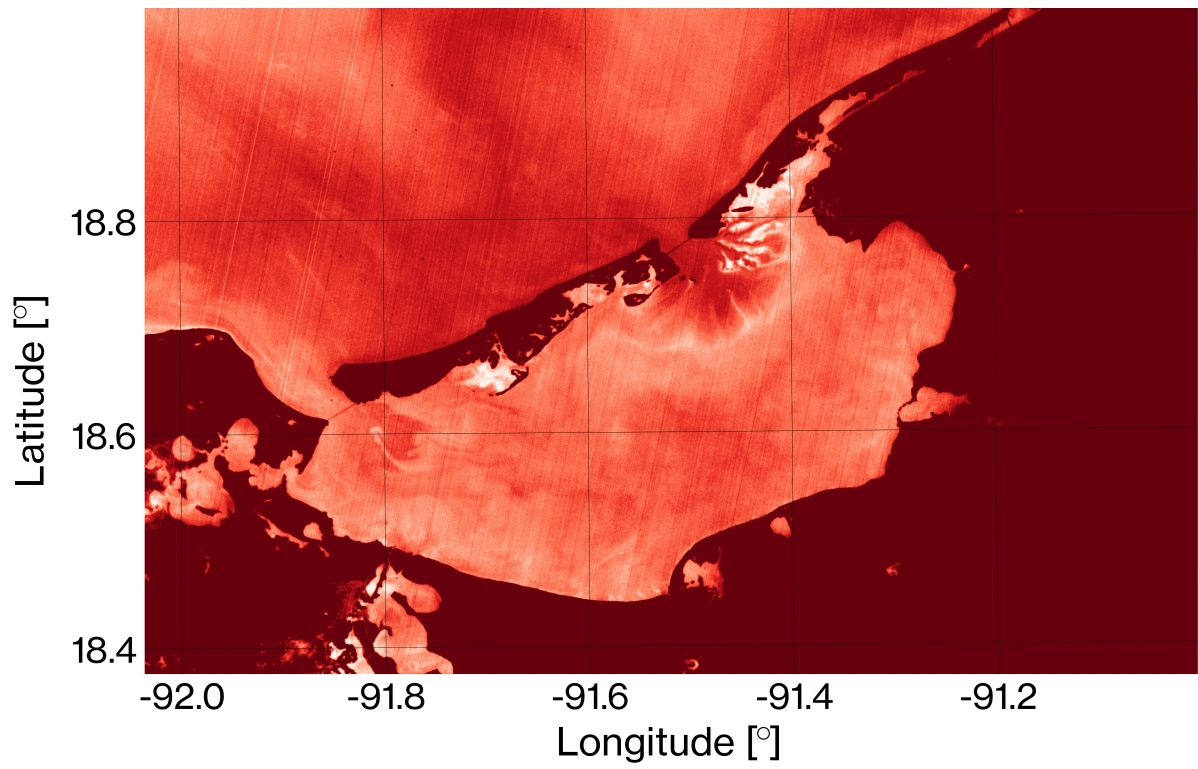Figure D.2: Relative temperature in Terminos Lagoon, 07-05-2015 (Dry season)

Figure D.3: Relative temperature in Terminos Lagoon, 09-05-2016 (Dry season)
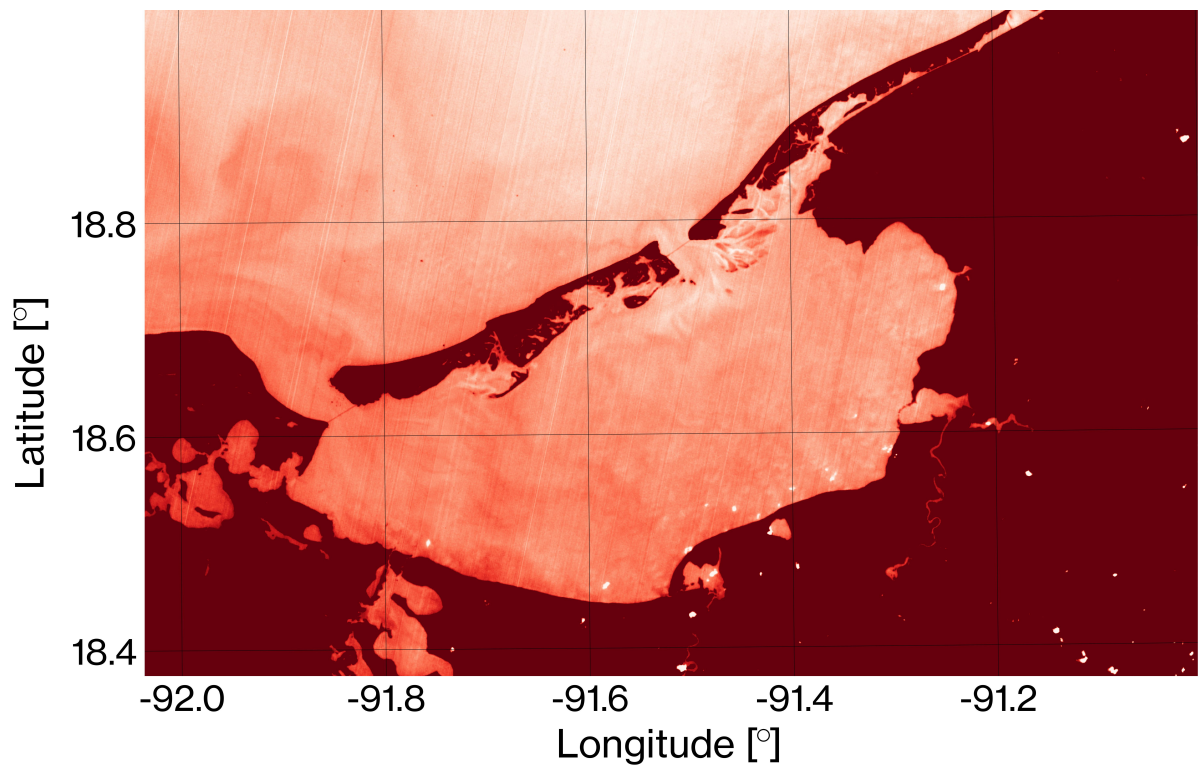

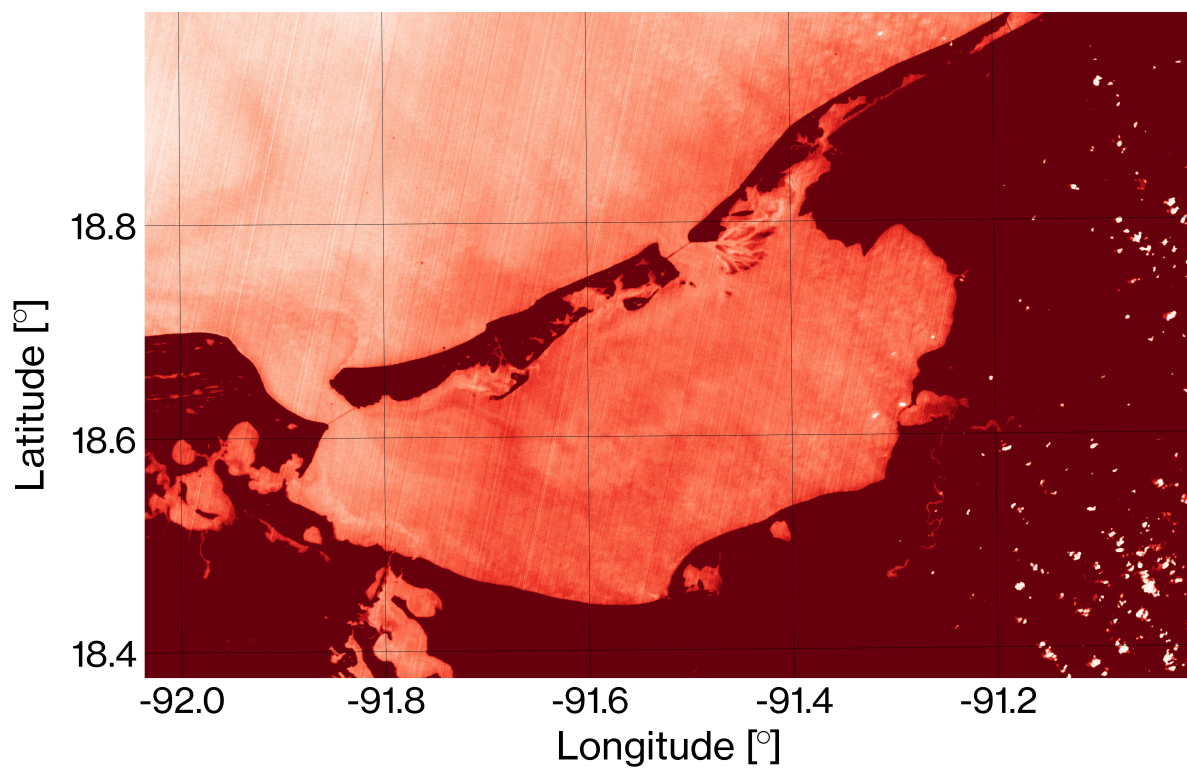Figure D.4: Relative temperature in Terminos Lagoon, 10-04-2017 (Dry season)

Figure D.5: Relative temperature in Terminos Lagoon, 13-04-2018 (Dry season)
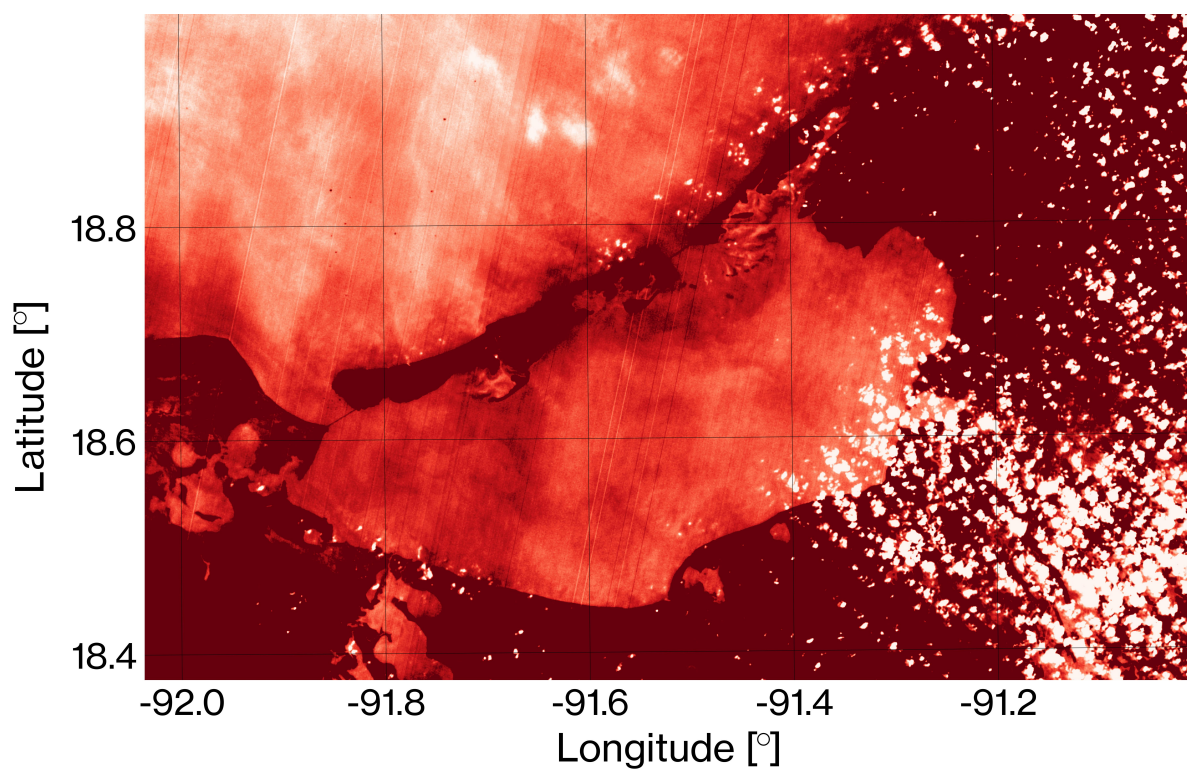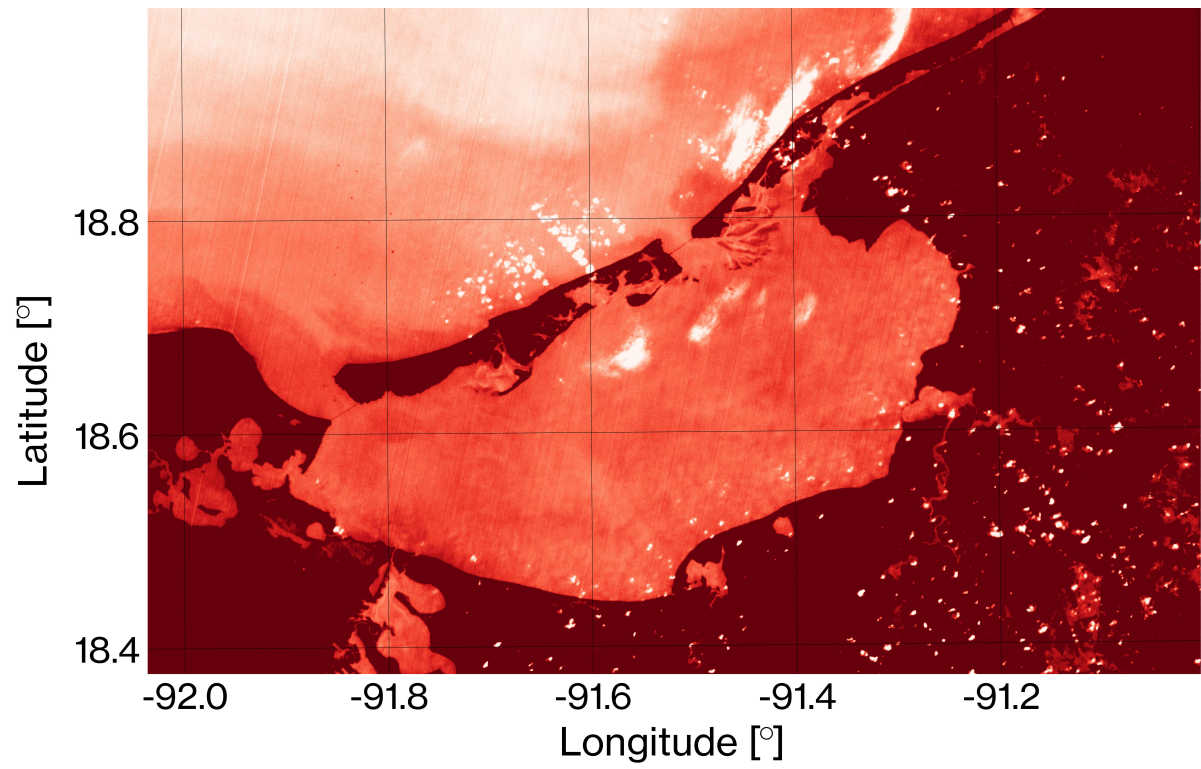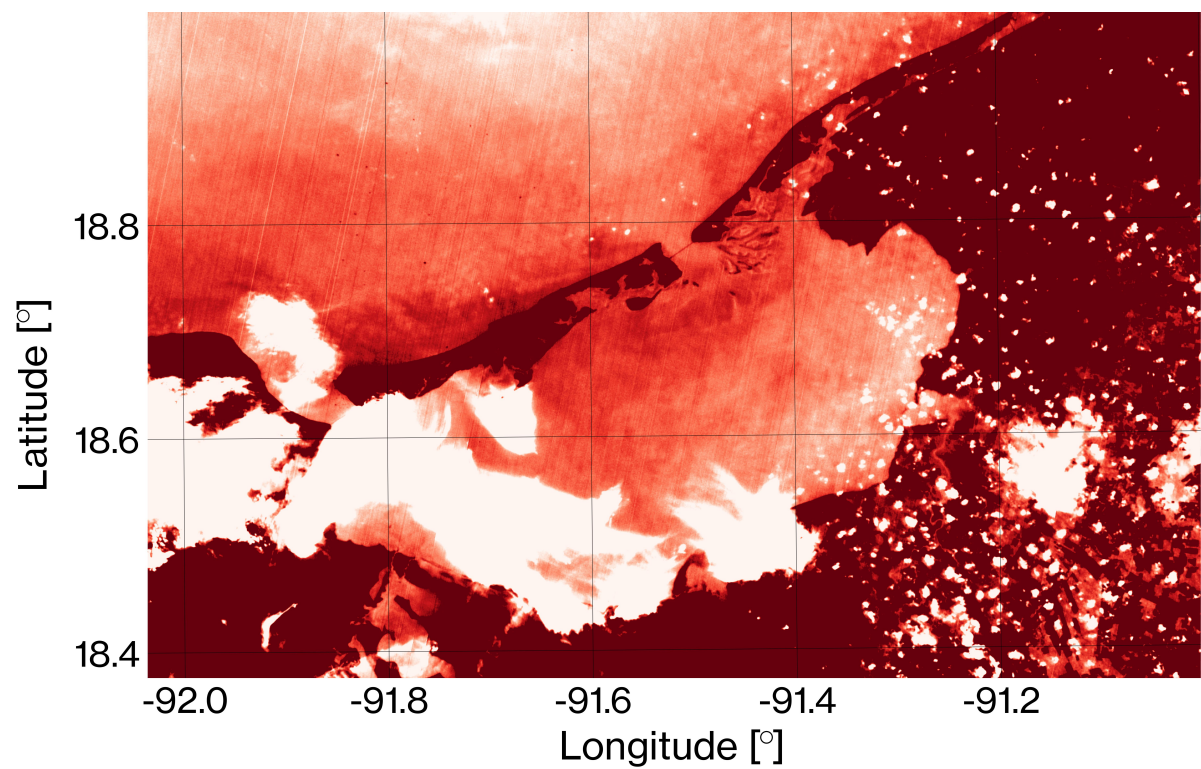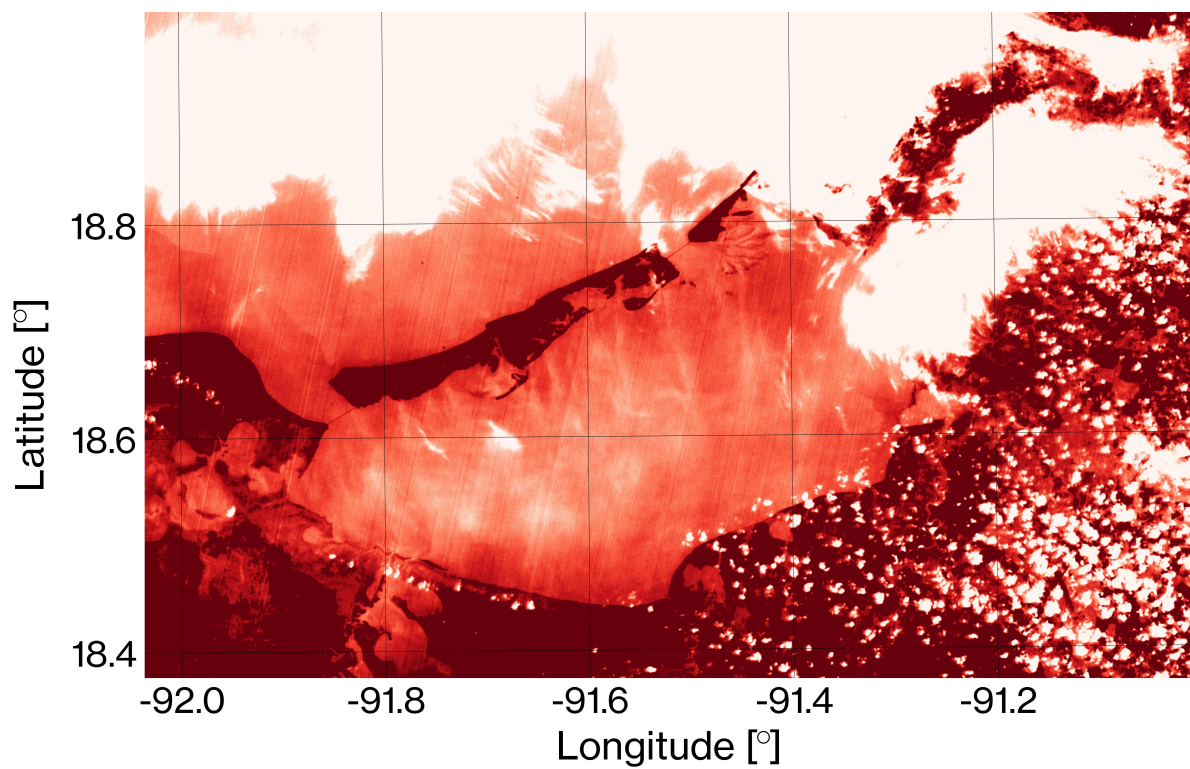

Figure D.6: Relative temperature in Terminos Lagoon, 08-08-2014 (Rainy season)

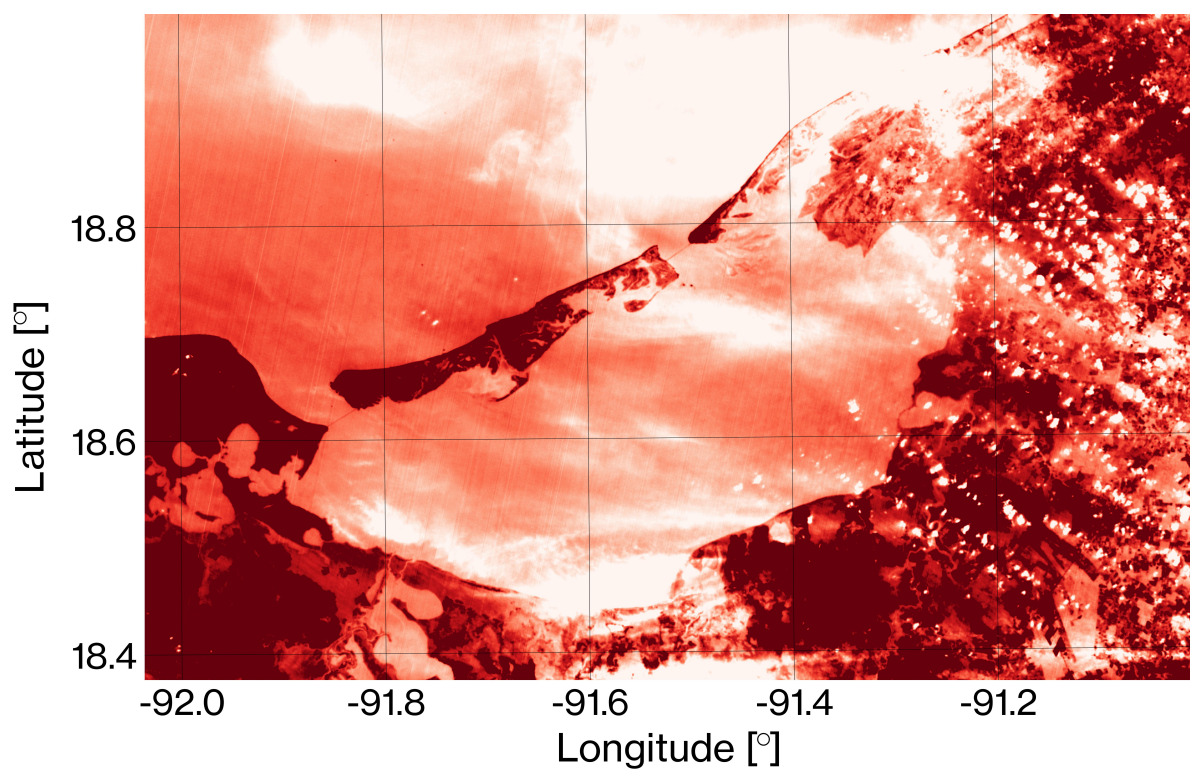Figure D.7: Relative temperature in Terminos Lagoon, 26-07-2015 (Rainy season)

Figure D.8: Relative temperature in Terminos Lagoon, 12-07-2016 (Rainy season)

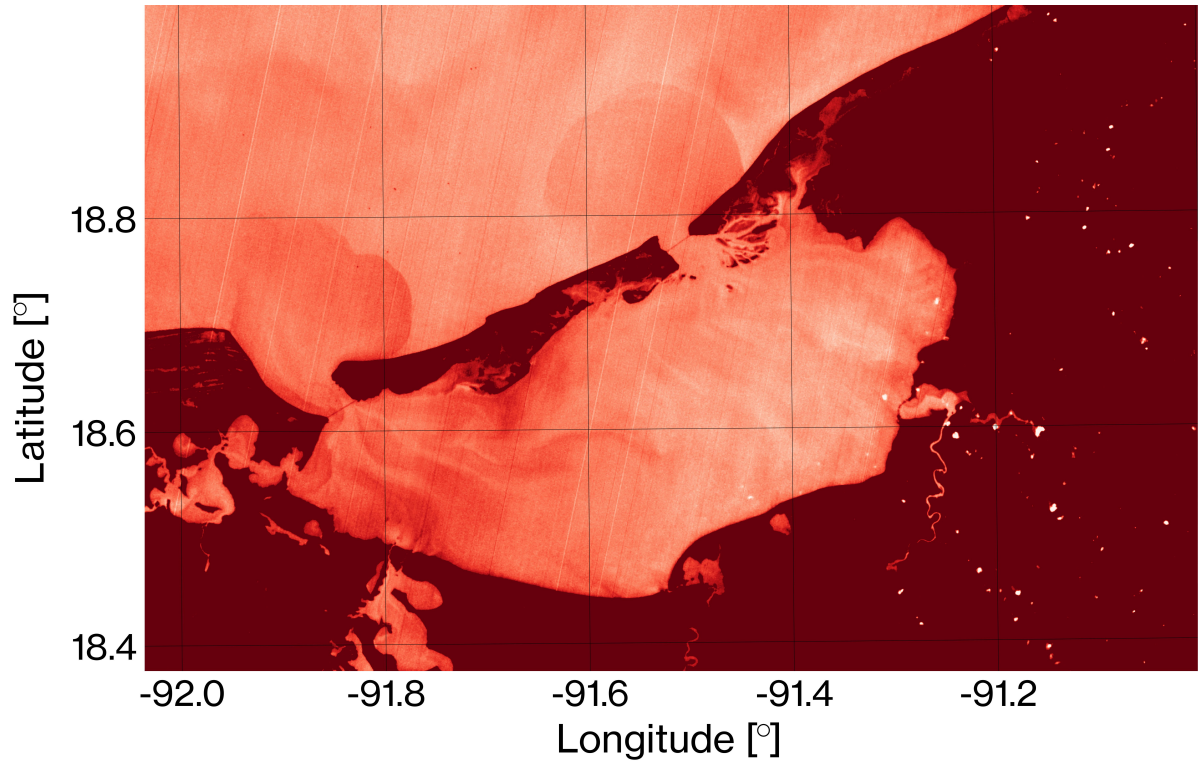Figure D.9: Relative temperature in Terminos Lagoon, 31-07-2017 (Rainy season)

Figure D.10: Relative temperature in Terminos Lagoon, 02-07-2018 (Rainy season)

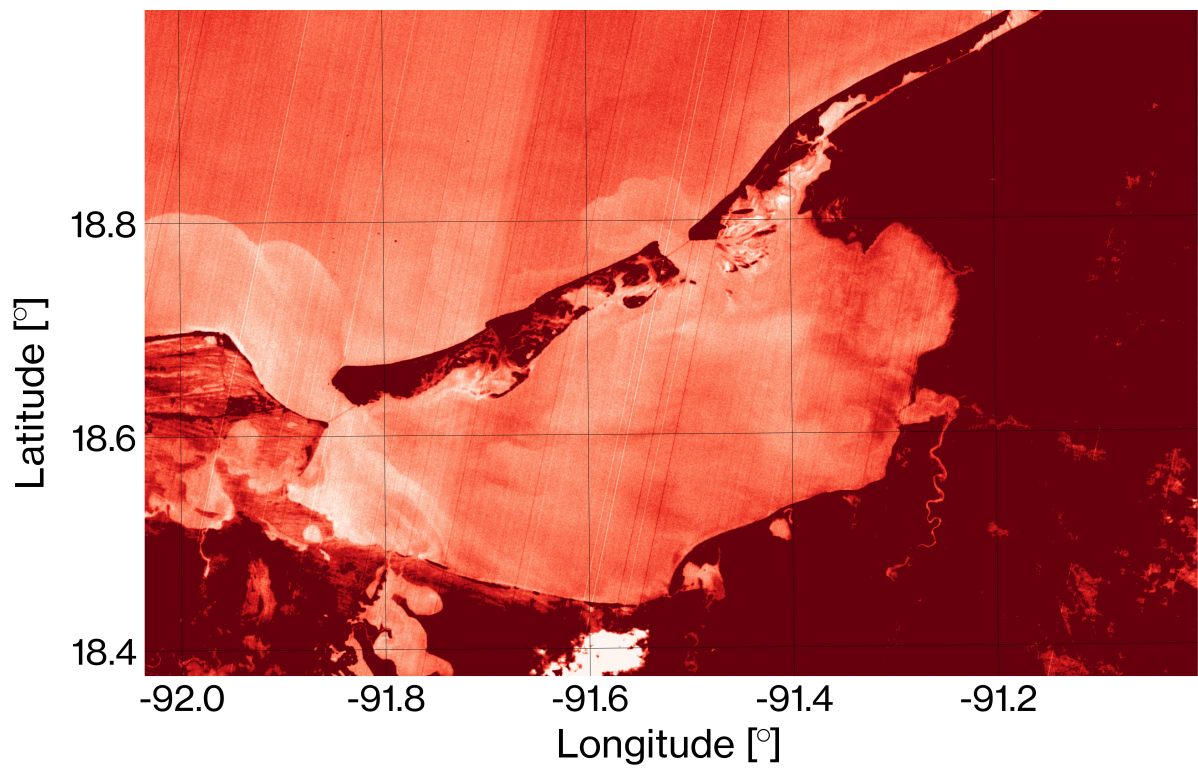Figure D.11: Relative temperature in Terminos Lagoon, 28-01-2014 (Nortes season)

Figure D.12: Relative temperature in Terminos Lagoon, 14-12-2014 (Nortes season)
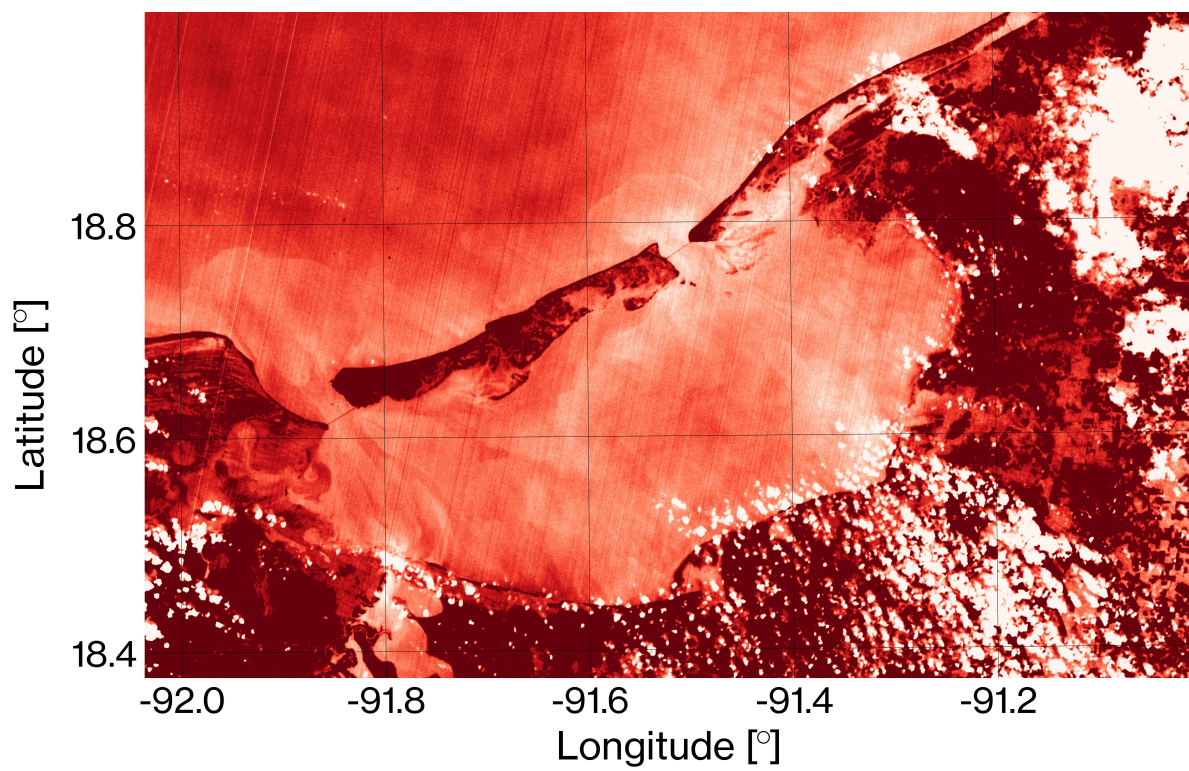
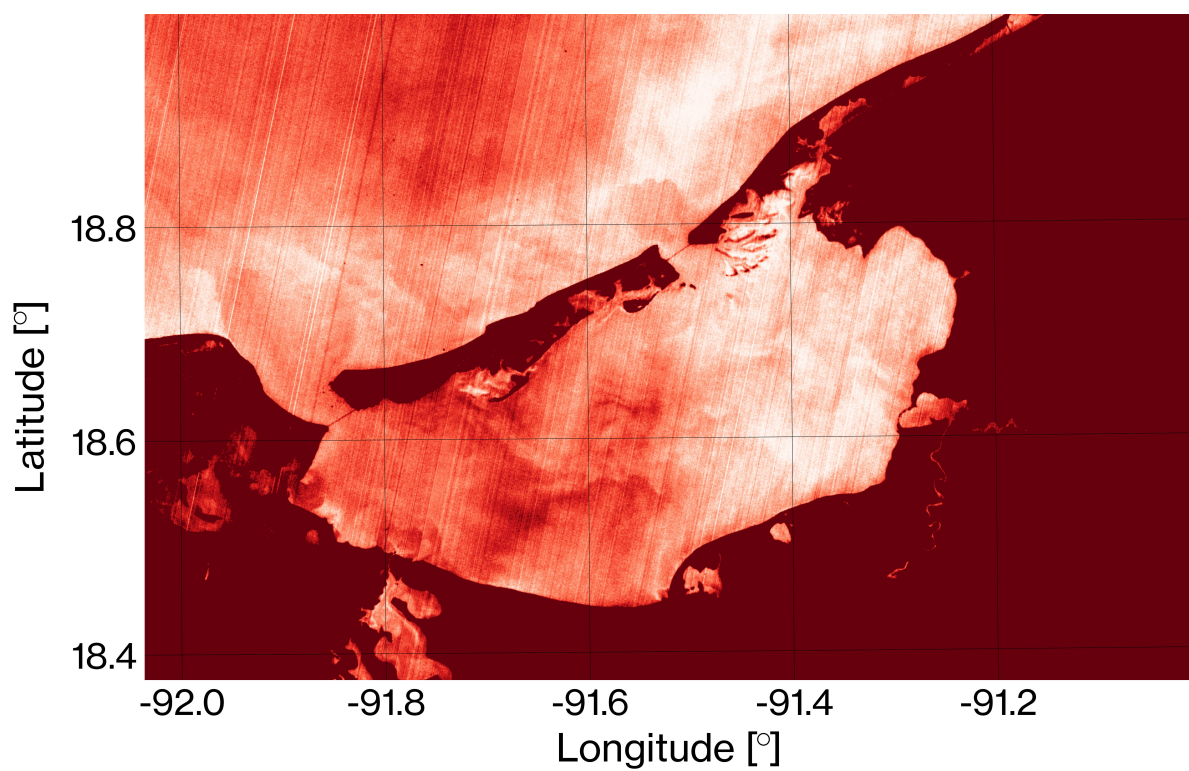Figure D.13: Relative temperature in Terminos Lagoon, 01-12-2015 (Nortes season)

Figure D.14: Relative temperature in Terminos Lagoon, 20-01-2017 (Nortes season)
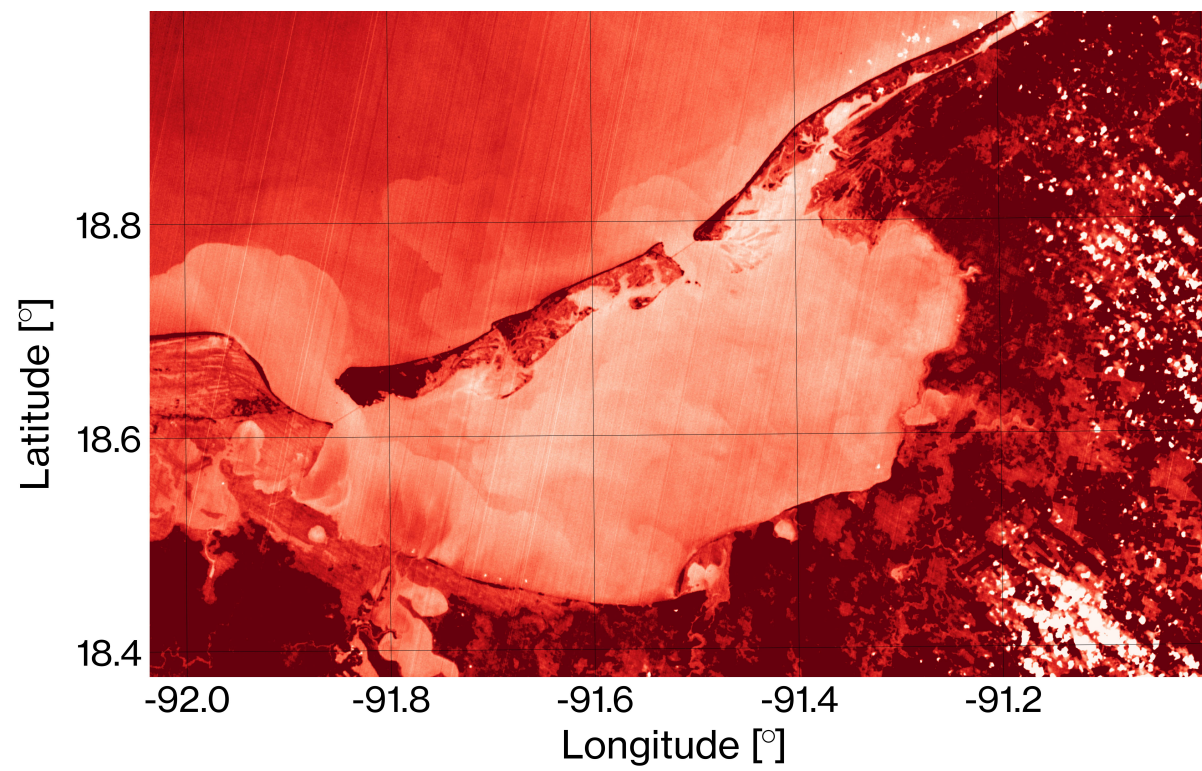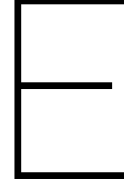
Figure D.15: Relative temperature in Terminos Lagoon, 07-01-2018 (Nortes season)

E

Secchi depth from satellite imagery

The Secchi depth is recorded during the field measurement campaigns. Remote sensing imagery is used to look into the spatial distribution of Secchi depth. To this end, a semi-analytical scheme [36] and Landsat 8 imagery is used to determine the Secchi depth. This methodology is chosen as it links remote-sensed measurements directly to Secchi depth. Another considered option is to create a turbidity index, an index with a strong correlation with Secchi depth, as described by Güttler [27]. A downside of this other method is the need for two control points: one with high and one with low turbidity. These could not be identified with confidence near Terminos Lagoon. Remote-sensed Secchi depth is compared to field measurements for quality assessment.

What follows is a brief description of the applied semi-analytical scheme. All steps are more elaborated on by Lee [36]. Secchi depth (Z_{sd}) can be expressed as:

$$Z_{sd} = \frac{1}{2.5 Min(K_d^{tr})} ln(\frac{|0.14 - R_{rs}^{tr}|}{0.013}) \tag{E.1}$$

With:

K_d^{tr}	= diffuse attenuation coefficient at the transparent window of the water body	
	within the visible domain (410-665 nm wavelength)	[m^{-1}]
R_{rs}^{tr}	= remote-sensing surface reflectance corresponding to this wavelength	[sr^{-1}]

$R_{rs}{}^{tr}$ and $K_d{}^{tr}$ are both from Landsat 8 measurements. While top of atmosphere reflectance is directly obtained from Landsat 8 data products [5], $R_{rs}{}^{tr}$ is the reflectance at surface level. Therefore an atmospheric correction should be applied. Following the example of Lee (2016), $R_{rs}{}^{tr}$ is obtained using the Acolite algorithm detailed in Vanhellemont and Ruddick (2014) [66], version Python 20180925.0. K_d is a function of sun zenith angle, as well as absorption a and backscattering b$_b$ coefficients of the upper water column, which can be derived from Landsat 8 data. To obtain these coefficients, first R_{rs} needs to be converted to its subsurface counterpart, r$_{rs}$ (sr^{-1}).

$$r_{rs}(\lambda) = \frac{R_{rs}(\lambda)}{0.52 + 1.7 R_{rs}(\lambda)} \tag{E.2}$$

Which is a function of the ratio b$_b$/(a+b$_b$) and can be expressed as:

$$r_{rs}(\lambda) = (g_0 + g_1 \frac{b_b(\lambda)}{a(\lambda) + b_b(\lambda)}) \frac{b_b(\lambda)}{a(\lambda) + b_b(\lambda)} \tag{E.3}$$

With model constants:

g_o	= 0.089	[sr^{-1}]
g_1	= 0.125	[sr^{-1}]

Then from this quadratic function there is by substituting $u = b_b/(a+b_b)$.

$$u(\lambda) = \frac{-g_0 + \sqrt{(g_0)^2 + 4g_1 \cdot r_{rs}(\lambda)}}{2g_1} \tag{E.4}$$

Hence, for any wavelength where there is a measurement of r_{rs}, and one knows either a or b_b, the other can be analytically determined. Through this logic, a is first estimated at a reference wavelength (λ_0):

$$a(\lambda_0) = a_w(\lambda_0) + \Delta a(\lambda_0) \tag{E.5}$$

With:

$a_w(\lambda_0)$= absorption coefficient of pure water at reference wavelength
$\Delta a(\lambda_0)$= contributions of non-water constituents

a_w is assumed constant, for all wavelengths. Δ a(λ_0) is estimated empirically from the r_{rs} spectrum, following QAA version 6 [31, 35]. Now $b_b(\lambda_0)$ can be determined with equation E.3, which gives

$$b_{bp}(\lambda_0) = \frac{u(\lambda_0) \cdot a(\lambda_0)}{1 - u(\lambda_0)} - b_{bw}(\lambda_0) \tag{E.6}$$

With:

$b_w(\lambda_0)$= backscattering coefficient of pure water at reference wavelength
b_{bp} = backscattering coefficient of particles

$b_w(\lambda)$ values are provided in literature. Here the values provided by Lee (2016) are used [36]. Other b_{bp} values can be estimated following a power-law function:

$$b_{bp}(\lambda) = b_{bp}(\lambda_0)(\frac{\lambda_0}{\lambda})^\eta \tag{E.7}$$

With:

η = exponent estimated empirically from r_{rs} spectrum [31]   [-]
λ = wavelength evaluated   [nm]

η is estimated as:

$$\eta = 2.0(1 - 1.2exp(-0.9\frac{r_{rs}(443)}{r_{rs}(561)})) \tag{E.8}$$

With:

$r_{rs}(443)$ = Subsurface equivalent remote-sensing surface reflectance for λ = 443 (band 1)   [sr^{-1}]
$r_{rs}(561)$ = Subsurface equivalent remote-sensing surface reflectance for λ = 561 (band 3)   [sr^{-1}]

Now a(λ) is easily derived using $b_{bp}(\lambda)$ and u(λ).

$$a(\lambda) = (1 - u(\lambda))(b_{bw}(\lambda) + b_{bp}(\lambda))/u(\lambda) \tag{E.9}$$

Finally, $K_d{}^{tr}$ can be modeled as:

$$K_d^{tr}(\lambda) = (1 + m_0 \cdot \theta_s)a(\lambda) + (1 - \gamma\frac{b_{bw}(\lambda)}{b_b(\lambda)}) \cdot m_1 \cdot (1 - m_2) \cdot e^{-m_3 \cdot a(\lambda)}b_b(\lambda) \tag{E.10}$$

With model parameters:

m_0 = 0.005
m_1 = 4.26
m_2 = 0.52
m_3 = 10.8
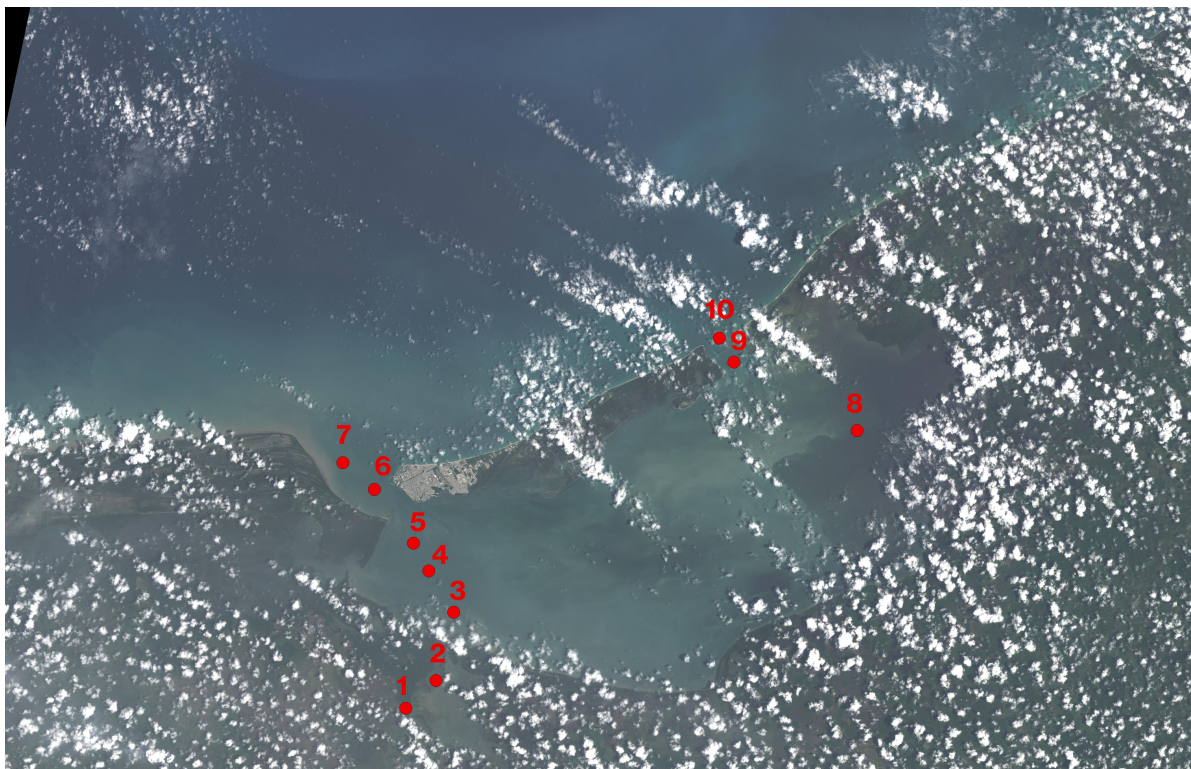γ = 0.265

Figure E.1: Terminos Lagoon and cloudless measurement locations, 04-09-2018

θ_s is the solar zenith angle in air in degrees, determined with 90- (solar elevation angle), which is provided in the Landsat 8 data metafile. Min(K_d^{tr}) in equation E.1 then is the K_d^{tr} from the band with lowest K_d^{tr}, band 3 in this case. This corresponds to green light.

First image to be treated is the overpass at 4 September 2018. It is chosen for the small temporal gap between image retrieval and field measurement campaigns: there is an temporal offset of 1 day for the Candelaria campaign and 3 days for the Palizada campaign. A color image and the remote-sensed Secchi depth are provided in figures E.1 and E.2, respectively. Clouds over the lagoon are present in the image, having a negative influence on the quality of the resulting Secchi depth chart. A comparison between field measurements and Secchi depth chart still is possible, by using the cloud free parts of the Secchi depth chart. To this end, figure E.2 also contains the field measurement locations which have been found to be uninfluenced by clouds. The field measurements are performed between 10.00 h and 14.00 h, whereas the image overpass is collected around 11.30 h. The overpass corresponds to peak flood horizontal tide. The field measurements correspond to rising horizontal tide, thus the measurement sets are assumed comparable. The relatively small differences between field- and remote-sensed measurement acquisition are therefore assumed negligible. The comparison between field- and remote-sensed measurements are given in figure E.3 and table E.1. This comparison shows that, taking field measurement uncertainty into account, 6 out of 10 measurement locations have remote-sensed Secchi depth within 10 cm of the field measurements, 2 are within 20 cm and 2 have a larger discrepancy. Take note that the larger differences are observed near the tidal inlets. These regions show large change in visibility over small distances, as seen near the Carmen inlet in figure E.2. Moreover, the three biggest discrepancies are found for the Candelaria campaign. R^2 is defined to be 0.576. There are just ten control points, so based on this comparison the chosen method cannot be validated definitively. The empirical parts of the chosen semi-analytical method showed in other work, however, to be improvable [48]. The same study noticed the method can be applied universally. It is thus decided Secchi depth will be investigated spatially at different moments using the earlier described semi-analytical method, which is necessary to find seasonal and spatial differences in Secchi depth.

The selection of images has similar requirements to those used for thermal imagery. Landsat 8 imagery with lowest cloud cover available, one image representing a season per year. The same images are used as the ones used to create thermal maps of the region. The images are given in table E.2. Resulting images are shown in
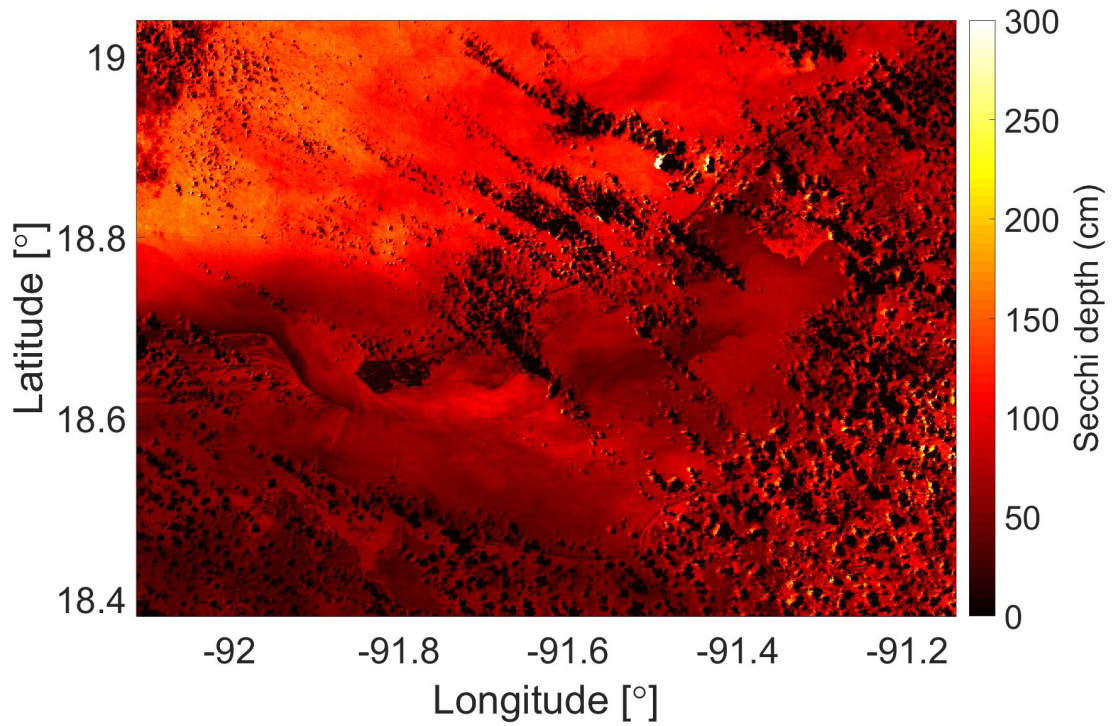
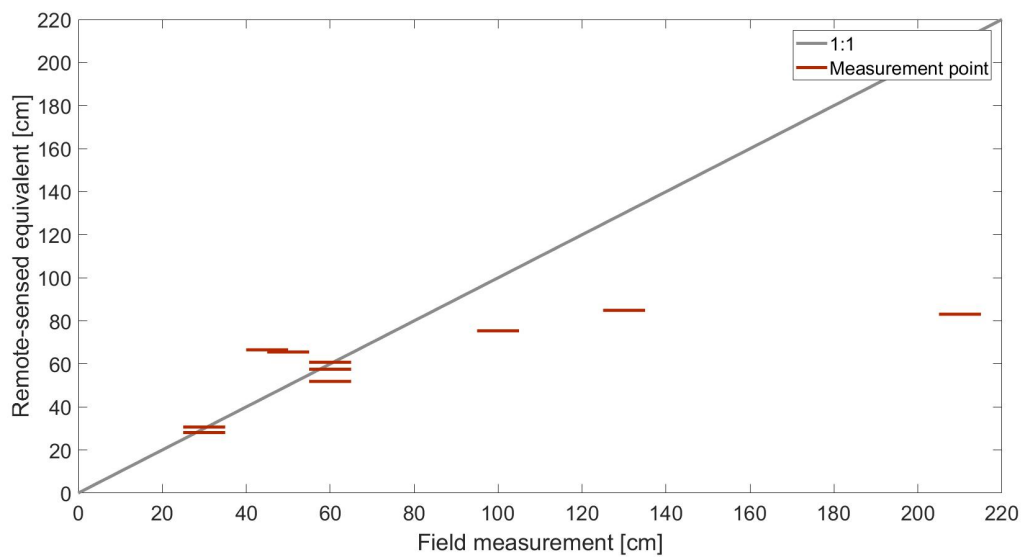Figure E.2: Secchi depth map Terminos Lagoon 04-09-2018

Figure E.3: Secchi depth measurement method comparison. Width of the bars is the measurement uncertainty in the field measurements: 5 cm

Table E.1: Comparison field measurement and remote-sensed measurements of Secchi depth

Measurement location	Fieldwork campaign	Field measurement [cm]	Remote-sensed measurement [cm]
1	Palizada	30	28.11
2	Palizada	30	30.68
3	Palizada	60	51.86
4	Palizada	60	57.53
5	Palizada	60	60.77
6	Palizada	45	66.55
7	Palizada	50	65.53
8	Candelaria	100	75.35
9	Candelaria	130	84.89
10	Candelaria	210	83.06

figure E.4 to E.18.

Table E.2: Acquisition dates and corresponding seasons Landsat 8 Secchi depth imagery

| Landsat 8 acquisition date	Corresponding season	Vertical tide Semar	Horizontal tide Semar
07-01-2018	Nortes	Flood	Ebb
20-01-2017	Nortes	Flood	Flood
01-12-2015	Nortes	Ebb	Ebb
14-12-2014	Nortes	Flood	Ebb
28-01-2014	Nortes	Ebb	Flood
13-04-2018	Dry	Ebb	Flood
10-04-2017	Dry	Ebb	Ebb
09-05-2016	Dry	Flood	Ebb
07-05-2015	Dry	Flood	Flood
01-03-2014	Dry	Ebb	Ebb
04-09-2018	Rainy	Flood	Flood
02-07-2018	Rainy	Flood	Flood
31-07-2017	Rainy	Flood	Flood
12-07-2016	Rainy	Flood	Flood
26-07-2015	Rainy	Flood	Flood
08-08-2014	Rainy	Flood	Flood
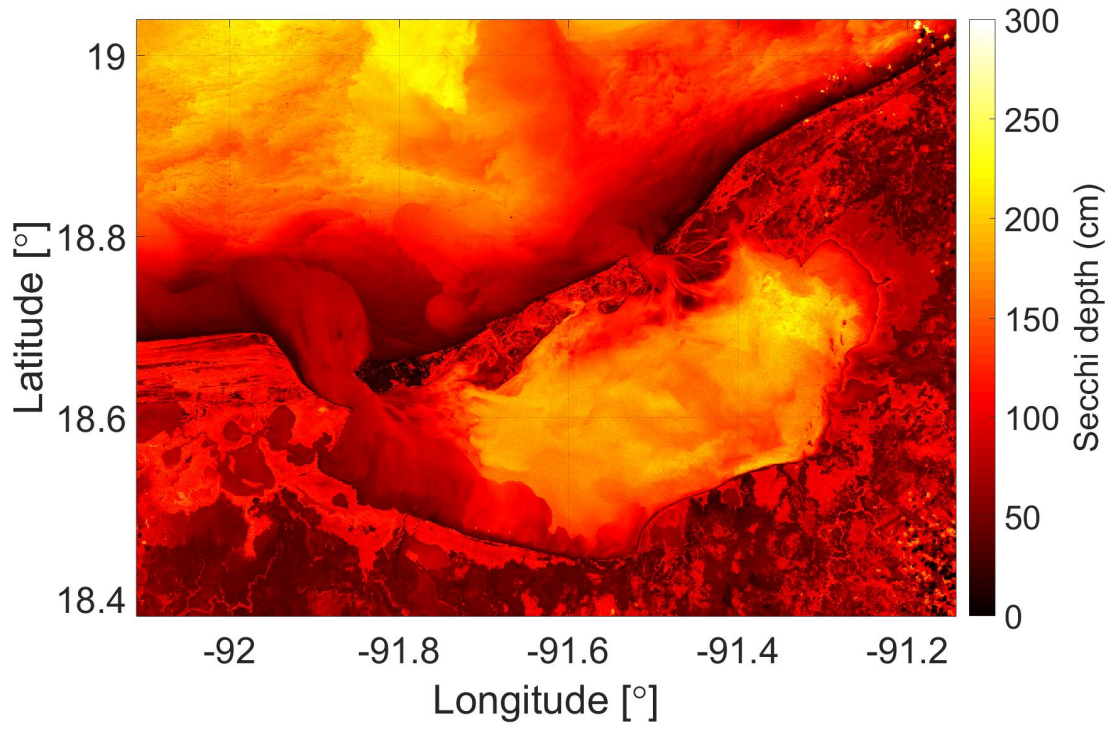
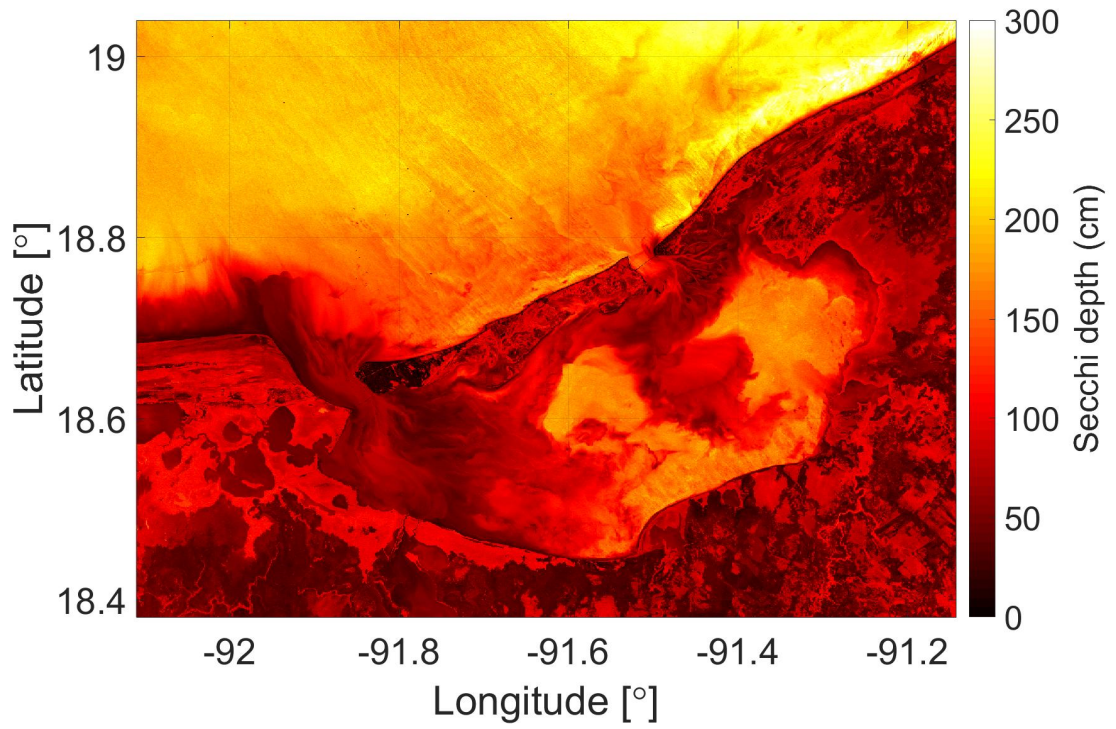Figure E.4: Secchi depth in Terminos Lagoon 07-01-2018

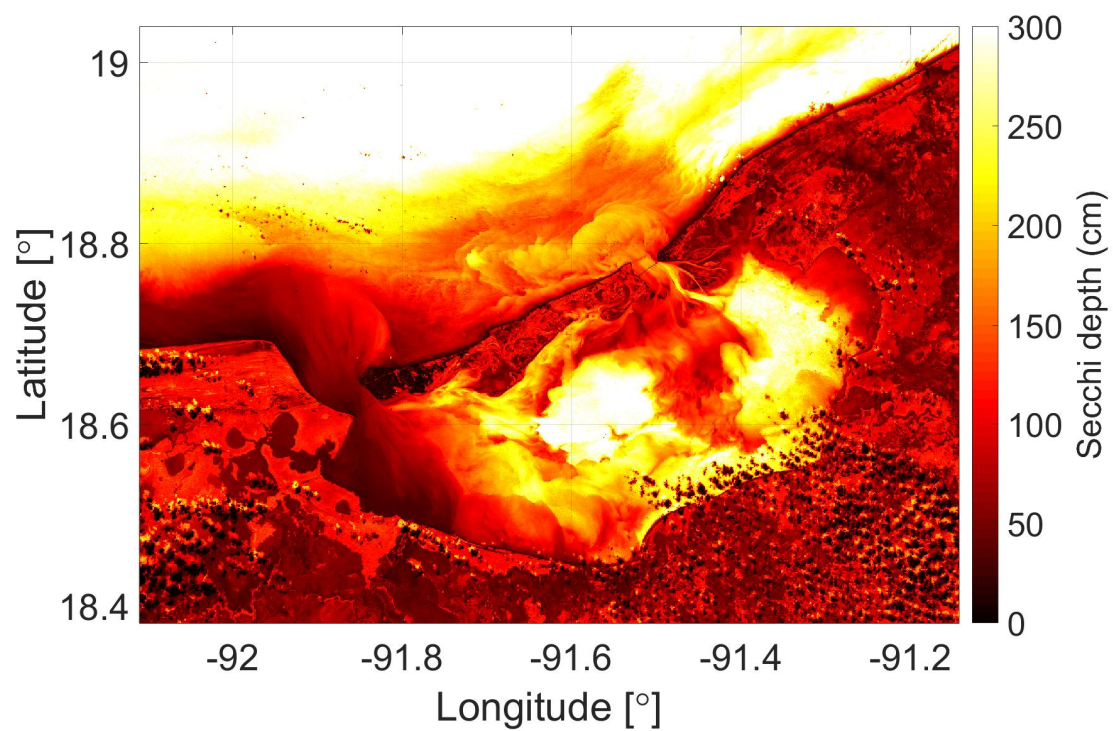Figure E.5: Secchi depth in Terminos Lagoon 20-01-2017

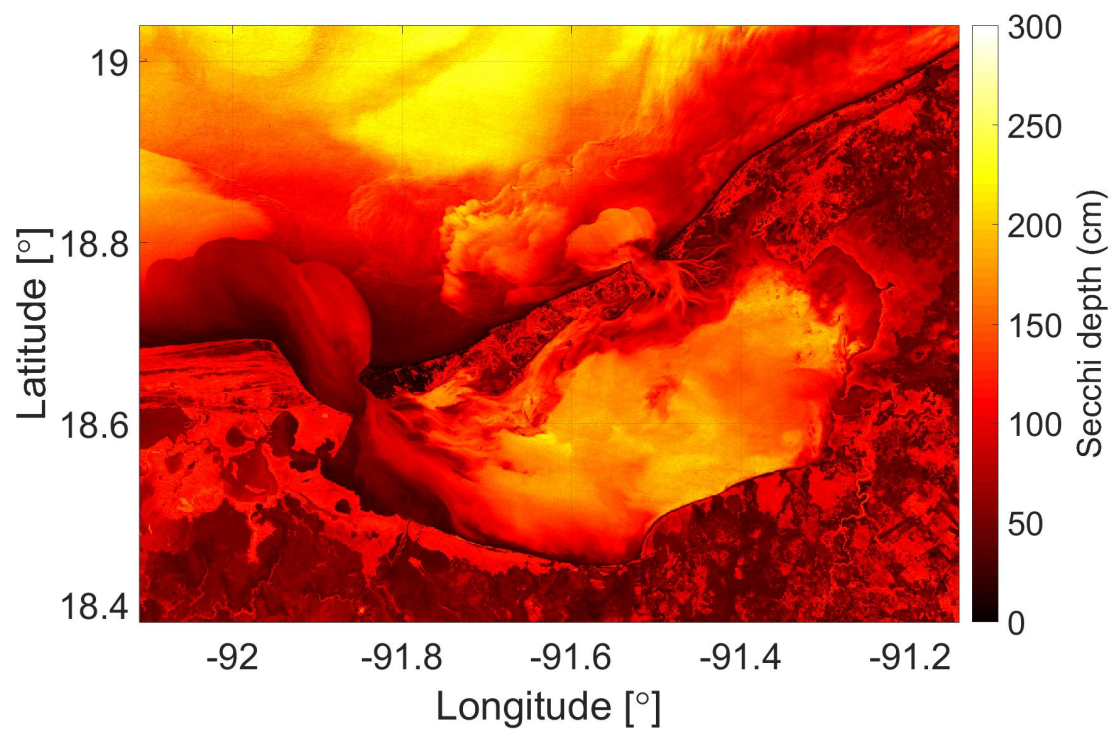Figure E.6: Secchi depth in Terminos Lagoon 01-12-2015

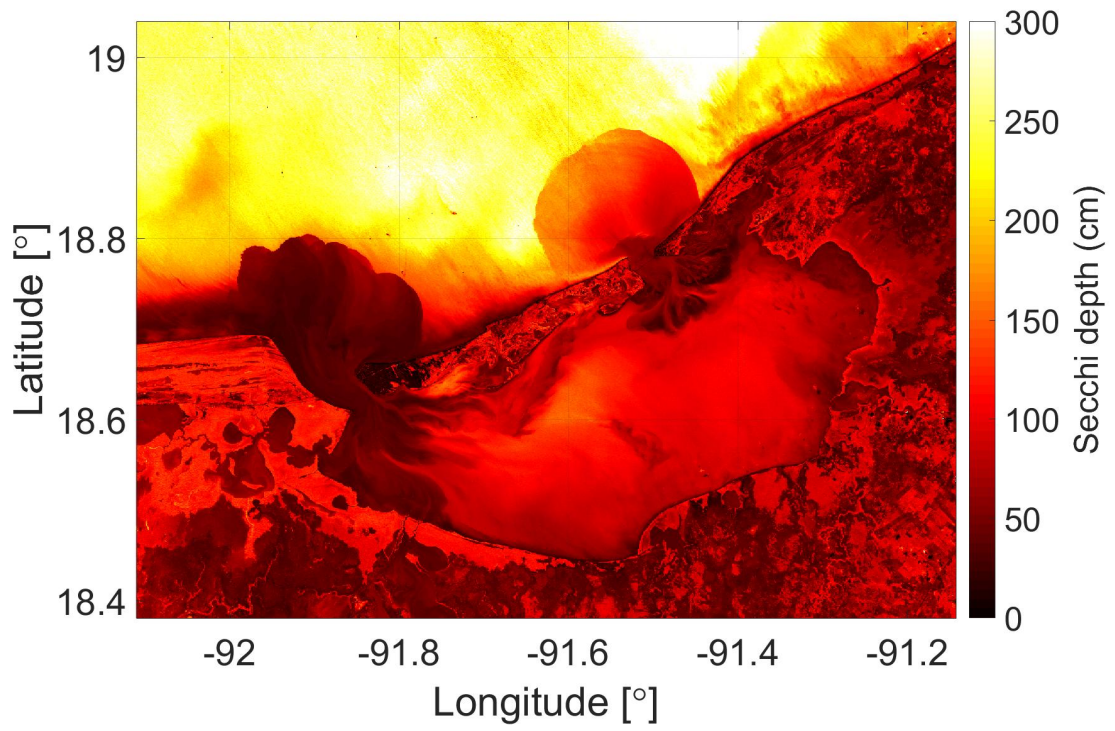Figure E.7: Secchi depth in Terminos Lagoon 14-12-2014

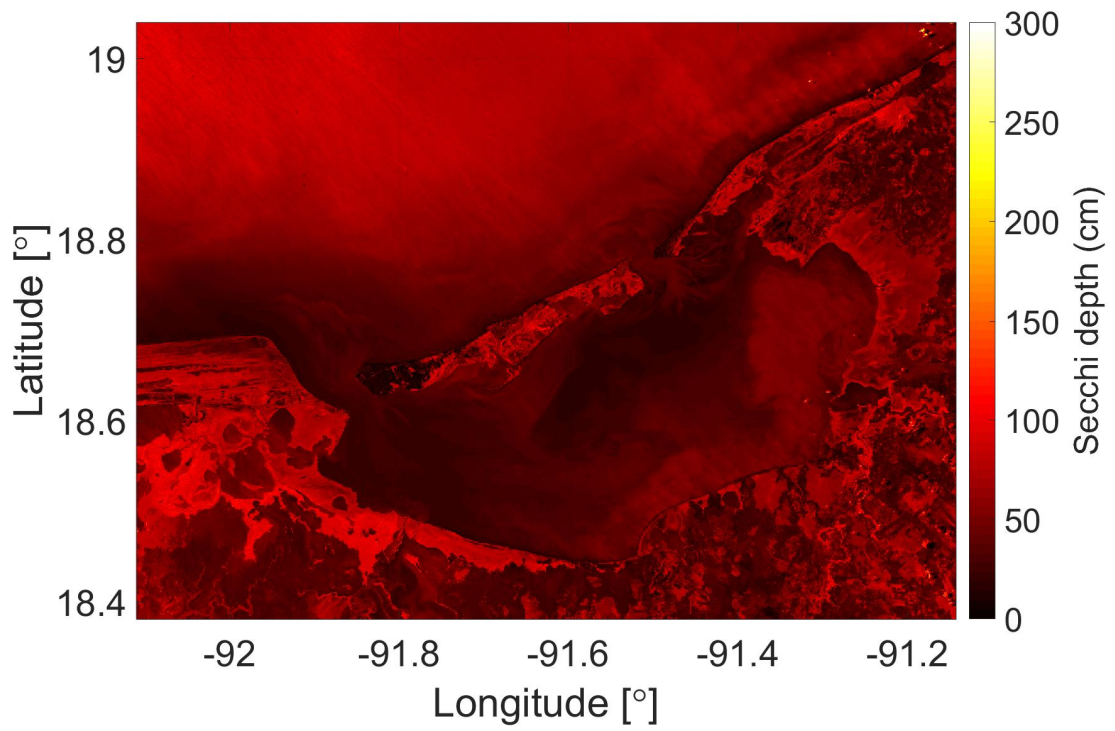Figure E.8: Secchi depth in Terminos Lagoon 28-01-2014

Figure E.9: Secchi depth in Terminos Lagoon 13-04-2018

Figure E.10: Secchi depth in Terminos Lagoon 10-04-2017

Figure E.11: Secchi depth in Terminos Lagoon 09-05-2016

Figure E.12: Secchi depth in Terminos Lagoon 07-05-2015

Figure E.13: Secchi depth in Terminos Lagoon 01-03-2014

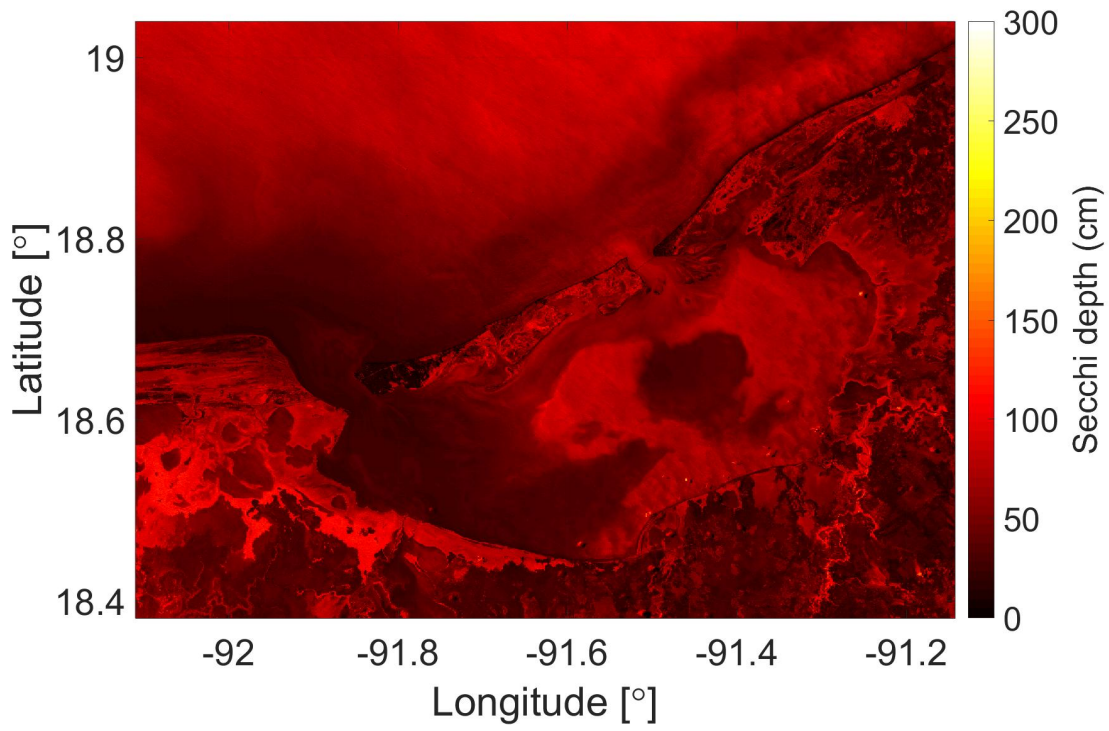Figure E.14: Secchi depth in Terminos Lagoon 02-07-2018

Figure E.15: Secchi depth in Terminos Lagoon 31-07-2017
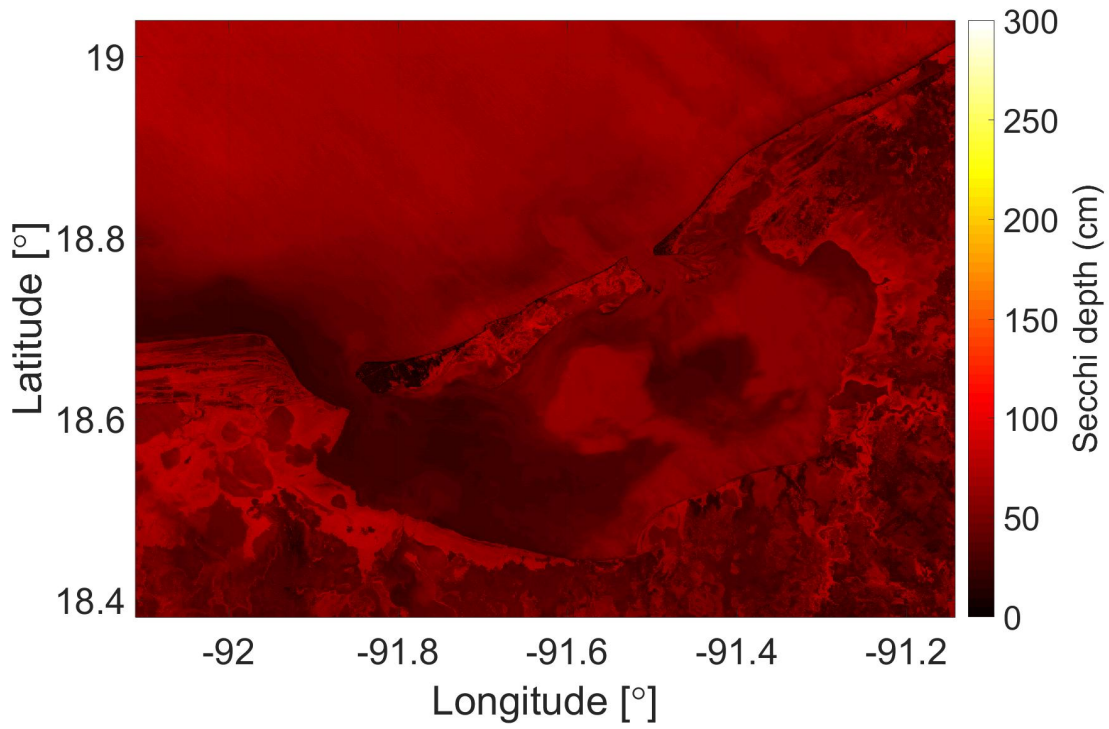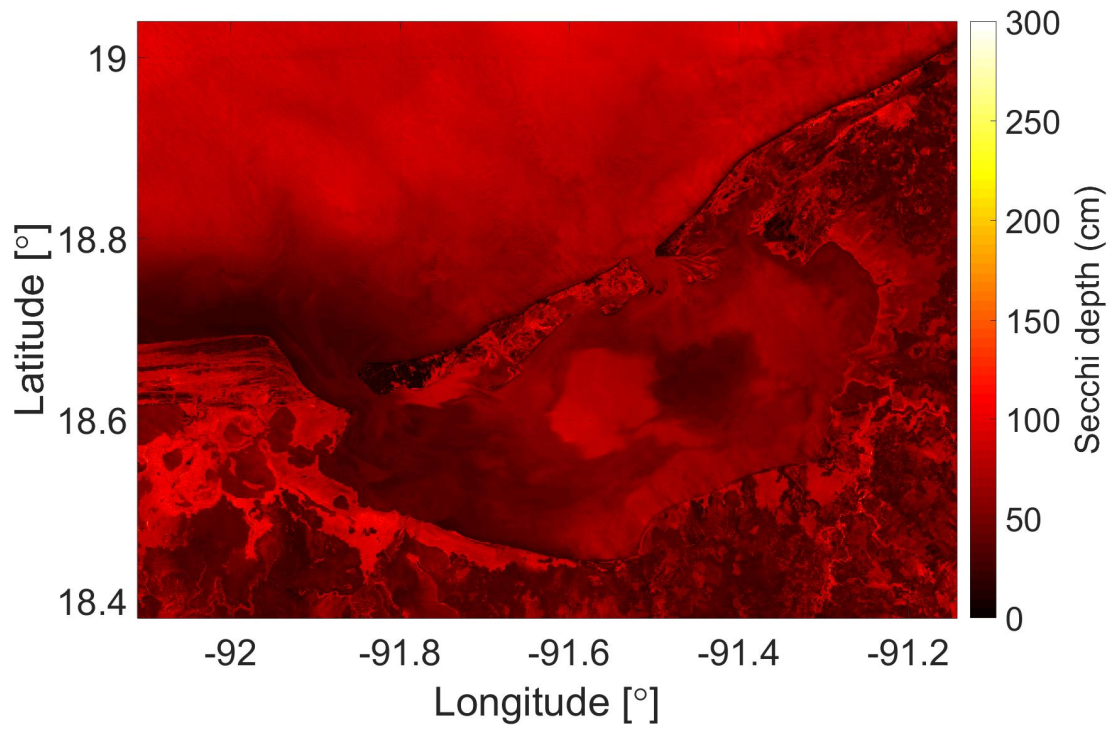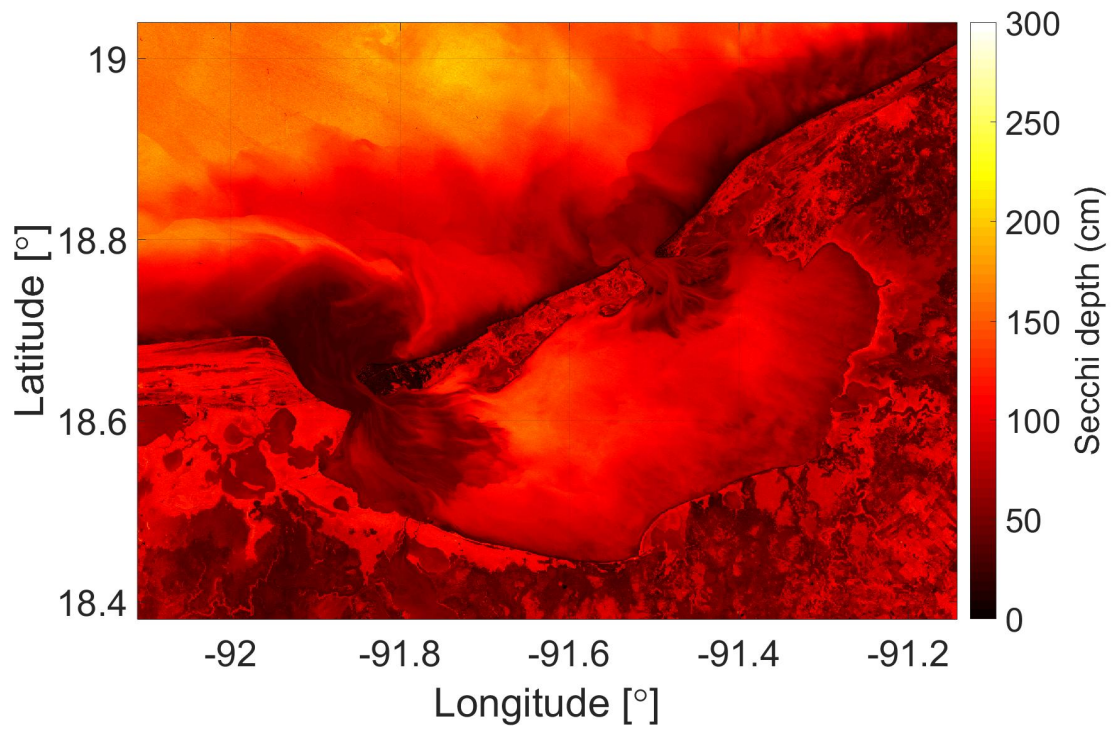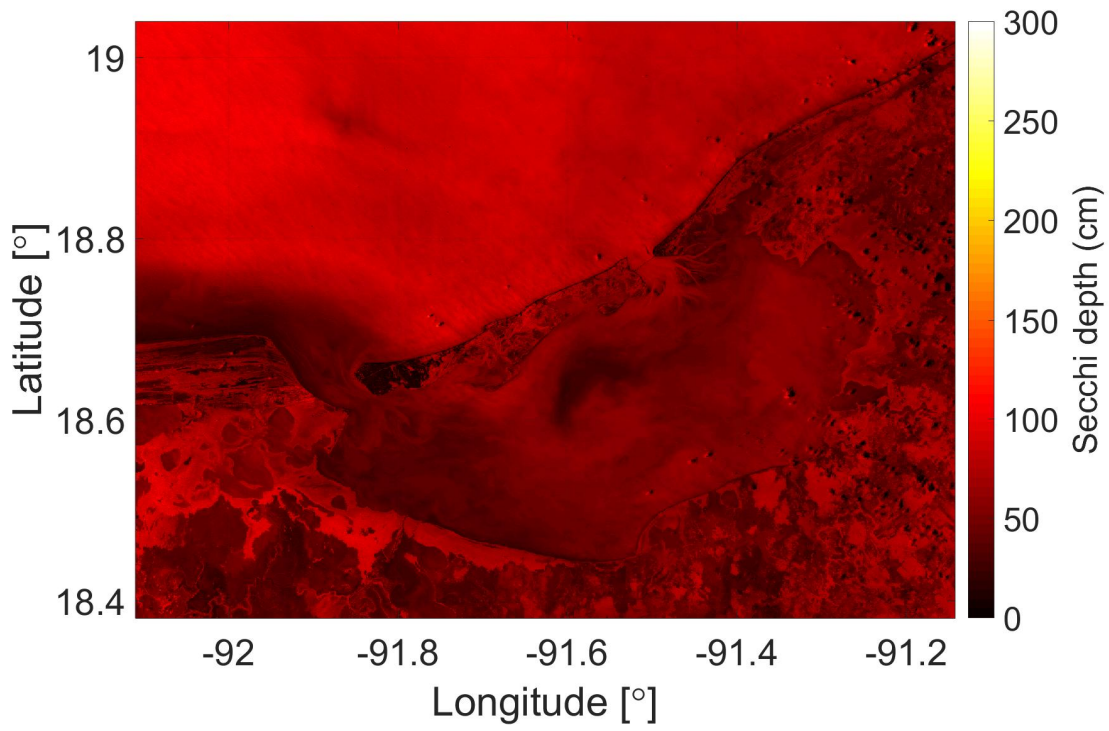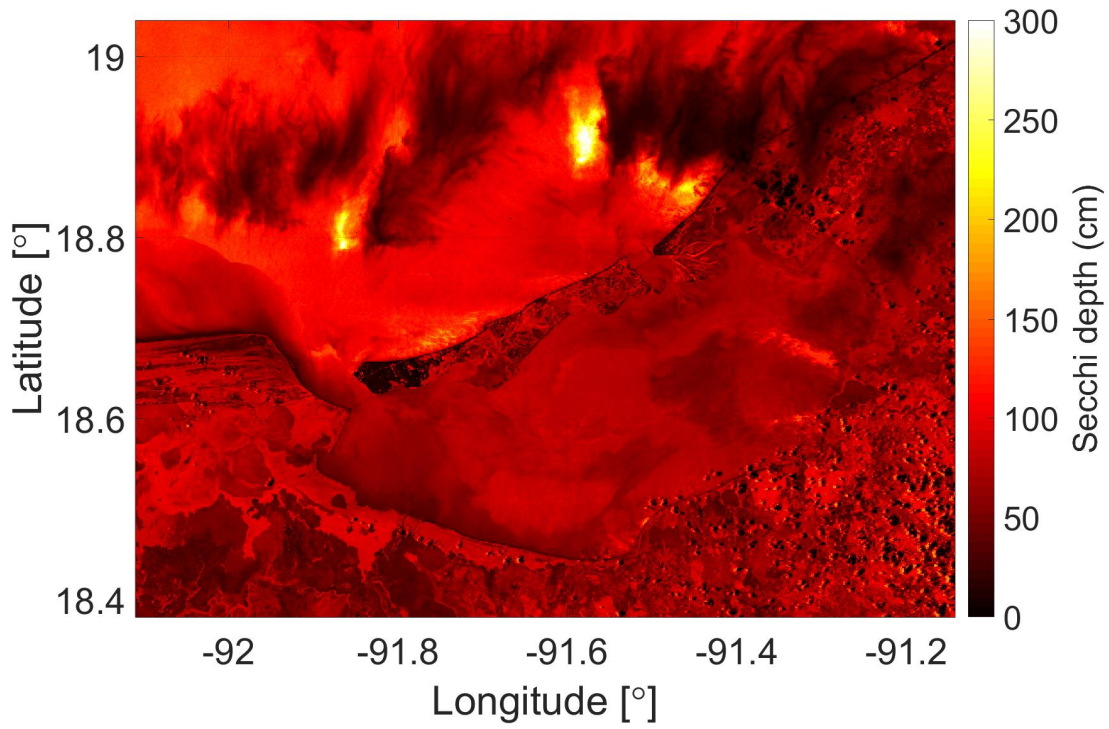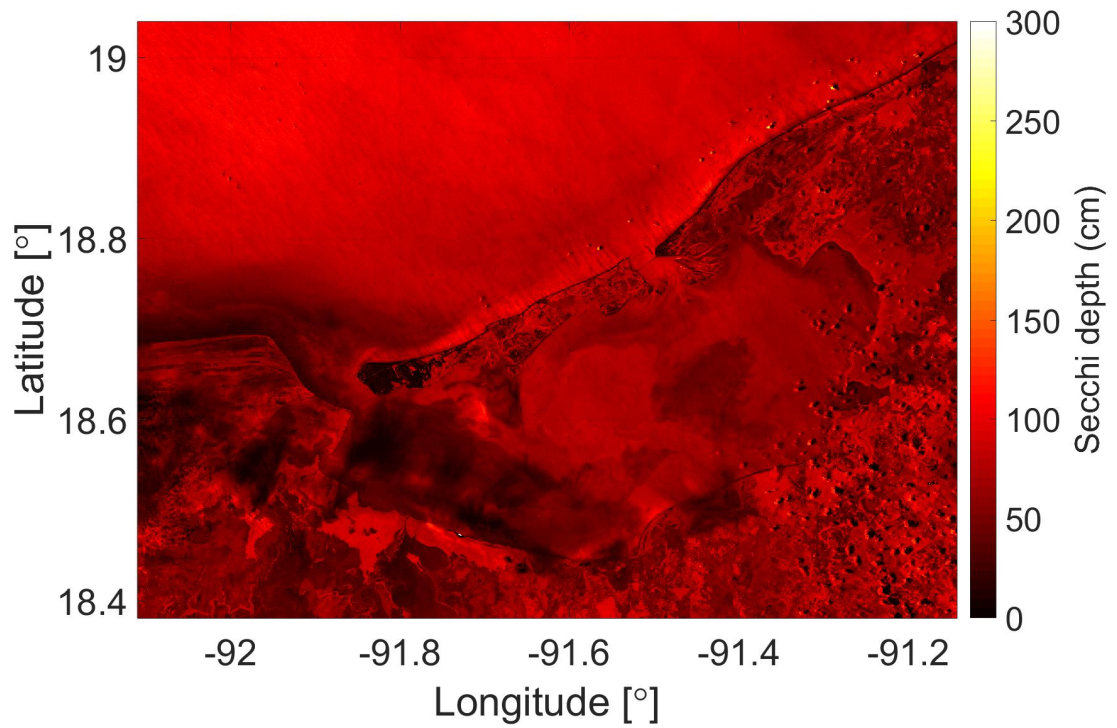
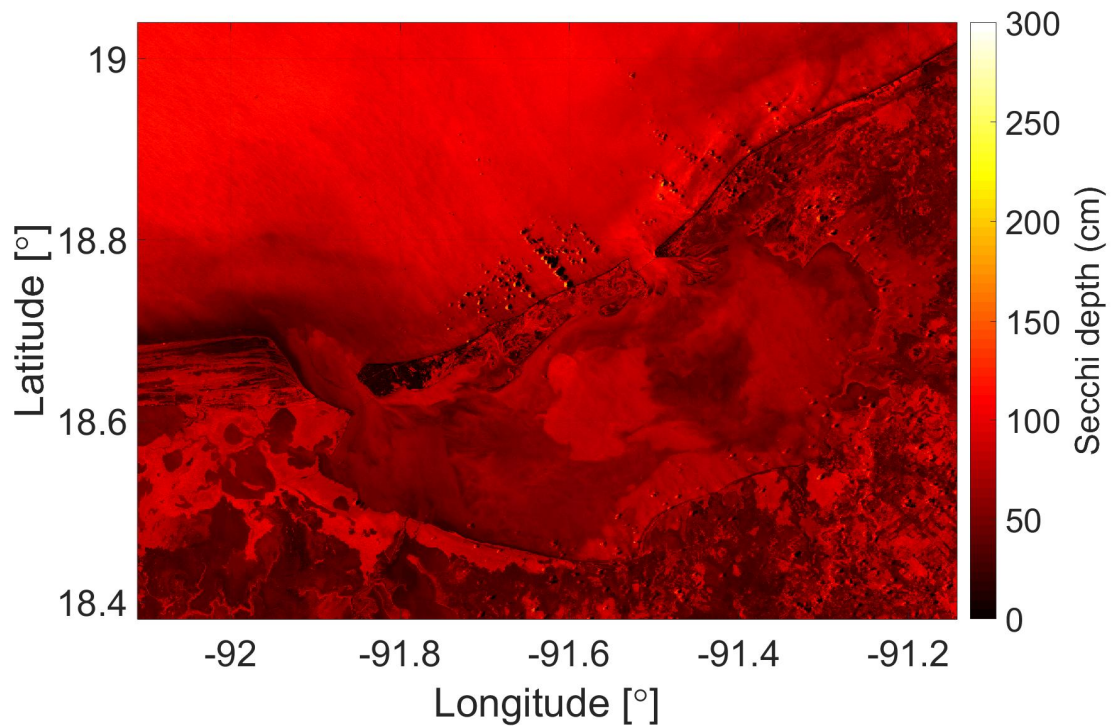Figure E.16: Secchi depth in Terminos Lagoon 12-07-2016

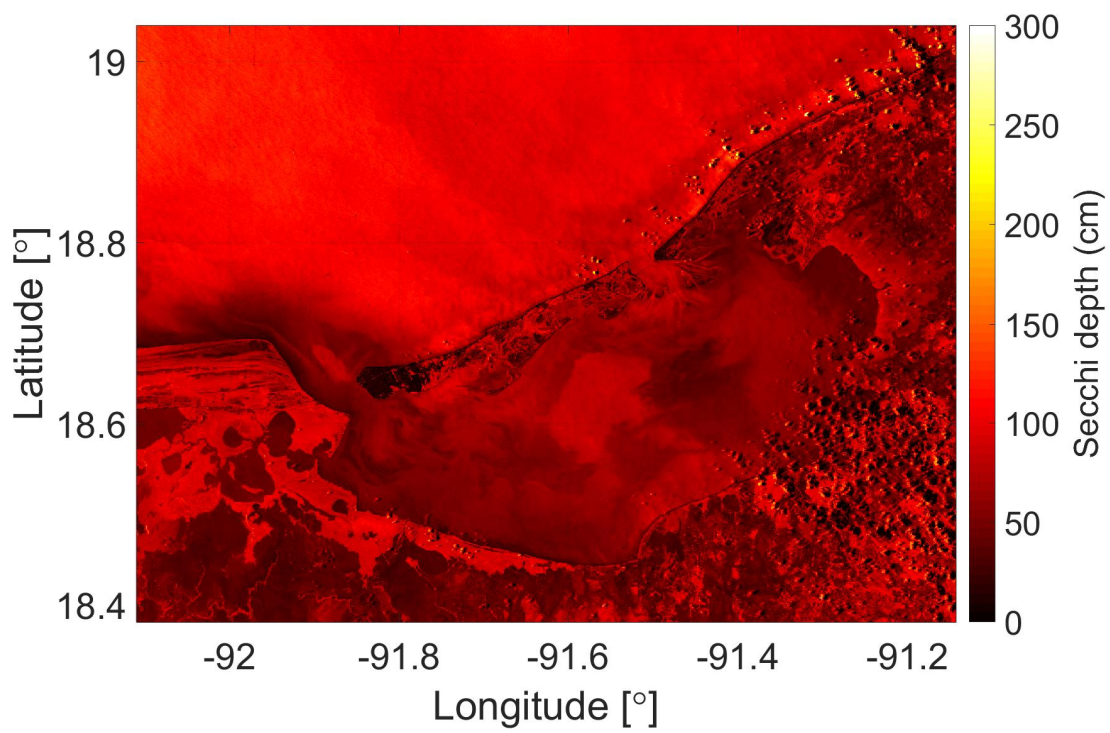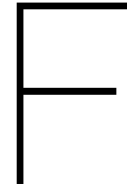Figure E.17: Secchi depth in Terminos Lagoon 26-07-2015

Figure E.18: Secchi depth in Terminos Lagoon 08-08-2014

F

Delft3D-FLOW Model

Some Delft3D-FLOW models are readily available. Due to long run times, often multiple days, there are also different models that do not take all the parameters into account to improve the run time. The models that are available are:

- comprehensive model (wind, tides and river discharge);
- comprehensive model without Palizada river (wind, tides);
- tidal model (tides).

Which model will be used in what circumstance, depends on the purpose at hand. The comprehensive model is described below. The other models have the same settings, except the driving forces.

F.1. Data input

Delft3D-FLOW requires different kinds of data input. First the domain is defined, which consists of a horizontal grid, vertical grid and the bathymetry. The particular model used also includes wind, so input of the wind is needed. To include the tides the tidal constituents at the boundaries need to be known.

F.1.1. Domain

This model makes use of a Cartesian coordinate system. The horizontal grid is a curvilinear grid. The system has 159 cells in M-direction and 137 cells in N-direction. In this grid, also a large part (approximately 185 km x 45 km) of the sea is included. This part of the sea is import for the simulation of the tides entering the lagoon. A visualization of the grid is shown in figure F.1a. The vertical grid is divided in 9 layers of different thickness. The model uses a σ-layer. This means that thickness of the layer is a constant percentage of the water depth. So these layers have a different thickness in space. The reason to choose a σ-layer is because layers with a smaller thickness have a higher accuracy. So the most interesting parts, bottom and surface, of the water column have the smallest layer thickness. Table F.1 shows how the water column is divided in layers.

Table F.1: Delft3D-FLOW layer thicknesses

Layer	Thickness [%]
1	3
2	6
3	11
4	17
5	26
6	17
7	11
8	6
9	3

The bathymetry that is used, is a non-uniform bathymetry.The bathymetry of the Terminos Lagoon is shown in figure F.1

(a) Grid

(b) Bathymetry
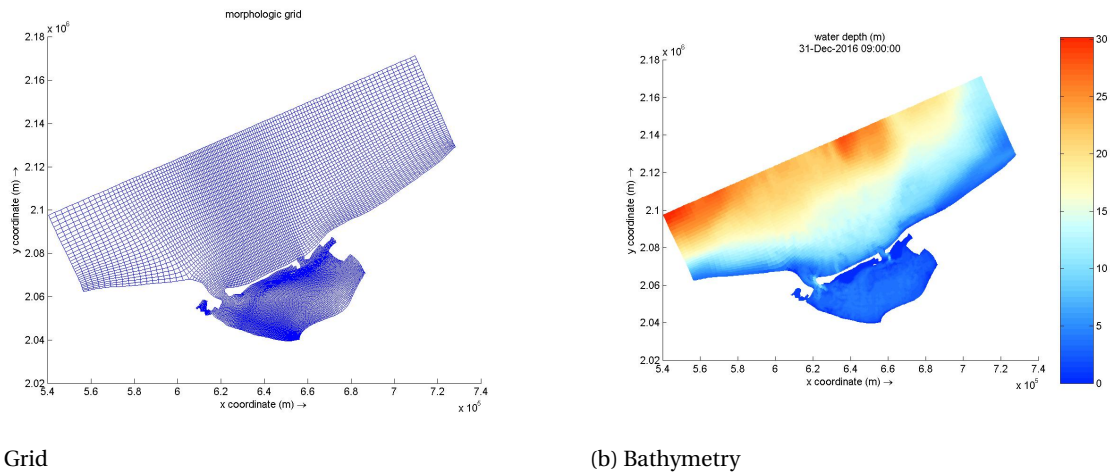
Figure F.1: Domain Terminos Lagoon Delft3D-FLOW

F.1.2. Processes

In Delft3D-FLOW different kinds of processes can be taken into account. In this model the temperature and salinity are selected, also the wind is selected. These processes are important, because they can vary a lot over the different seasons. Salinity varies in time and space, because input water is both fresh and salt: fresh water from the rivers and salt water from the sea. Both the wind direction and speed varies over the different seasons.

F.2. Boundary conditions

The boundaries are formed by Este01 till Este05 and Norte01 till Norte13, these boundaries are shown in figure F.2. The flow condition has an open boundary, which is the water level and is forced by astronomic components. The astronomic forcing is formed by tidal constituents. The amplitude and phase of the tidal constituents differs a bit for every location in the grid.

F.3. Parameters

The physical parameters and numerical parameters are described.
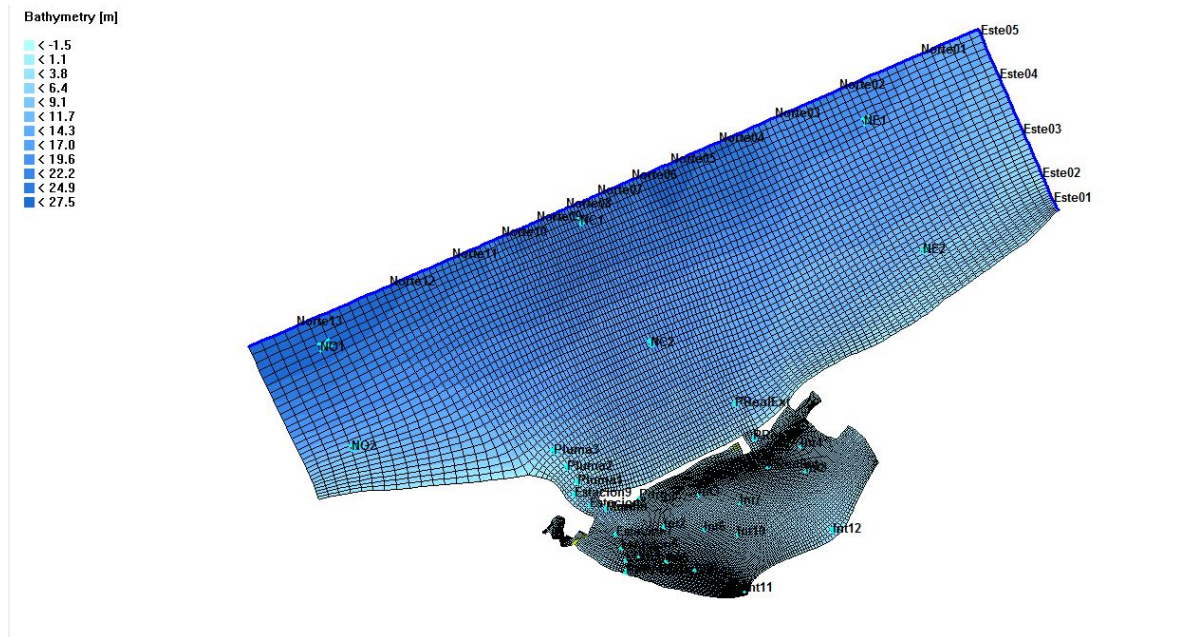
Figure F.2: Boundaries Terminos lagoon Delft3D-FLOW

F.3.1. Physical parameters

Table F.2: Physical parameters Delft3D-FLOW

Parameter	Value	Unit
Hydrodynamic constants		
Gravity	9.81	$[m/s^2]$
Water density	1000	$[kg/m^3]$
Air density	1	$[kg/m^3]$
Bottom roughness Chézy		
U	65	$[m^{1/2}/s]$
V	65	$[m^{1/2}/s]$
Background horizontal		
Horizontal eddy viscosity	100	$[m^2/s]$
Horizontal eddy diffusivity	100	$[m^2/s]$
Heat flux model (Ocean)		
Water surface area	0	$[m^2]$
Sky cloudiness	0	[%]
Secchi depth	2	[m]
Dalton number for evaporative heat flux	0.0013	[-]
Stanton number for heat convection	0.0013	[-]
Interpolation	linear	[-]

Numerical parameters

Table F.3: Numerical parameters Delft3D-FLOW

Parameter	Value	Unit
Drying and flooding check at	Grid cell centres and faces	
Depth specified at	Grid cell corners	
Depth at grid cell centres:	Maximum	
Threshold depth	0.1	[m]
Marginal depth	-999	[m]
Smoothing time	60	[min]
Advection scheme for momentum	Cyclic	
Advection scheme for transport	Cyclic	
Forester filter (horizontal)	Included	
Forester filter (vertical)	Included	

F.4. Output

The output storage contains 1 year of data, with a timestep of 1 minute. The map results are stored every 240 minutes and the history interval is 120 minutes. The output returns a map which covers the entire grid. The history interval can be seen at all the points shown in figure F.2.

G

Boxplot description
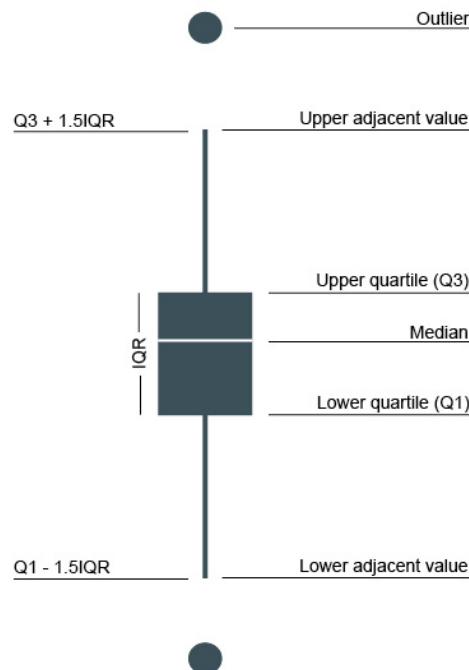
Figure G.1: Example of boxplot with description of its features [6]

A box plot is a graphically presentation of the distribution of data, an example is shown in figure G.1. The plot consists of one rectangular, two whiskers and outliers. 50 Percent of the data falls into the rectangular, which is called interquartile range (IQR). The top border of the rectangular is the upper quartile, or third quartile (Q3), with 75 % of the data below this quartile. The bottom border of the rectangular is the lower quartile, or first quartile (Q1), with 25 % of the data below this border. The median lays within the rectangular and is the mid point of the dataset. One half of the data points has a value higher than the median and the other half has lower values. The median is not equal to the mean, but the median could have the same value as the mean. The top of the above whisker is the upper adjacent value, or maximum value, which is equal to $Q3 + 1.5IQR$. The bottom of the lower whisker is the lower adjacent value, or minimum value, which is equal to $Q1 - 1.5IQR$. All the data points that are outside the $Q1 - 1.5IQR$ - $Q3 + 1.5IQR$ range are outliers.
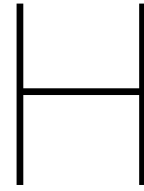
Penman calculation

The method of Penman is used to determine evaporation from an open water body. It is given in equation H.1 [52]:

$$E_0 = \frac{\left\{ \dfrac{sR_N}{\rho\lambda} + \dfrac{c_p\rho_a}{\rho\lambda} \dfrac{(e_s - e_a)}{r_a} \right\}}{s + \gamma} \tag{H.1}$$

With:

R_N	= Earth's net radiation	[J day^{-1}m^{-2}]
λ	= heat of evaporation (λ= 2.45 MJ/kg)	[J/kg]
s	= inclination evaporation curve	[kPa K^{-1}]
c_p	= specific heat of air with constant pressure (c$_p$ = 1004 J kg^{-1}K^{-1})	[J kg^{-1}K^{-1}]
ρ_a	= density of air (ρ_a = 1205 kg/m^3)	[kg/m^3]
ρ	= density of water (ρ= 1020 kg/m^3)	[kg m^3]
e_a	= actual vapour pressure of the air at 2 m height	[kPa]
e_s	= saturation vapour pressure	[kPa]
γ	= psychrometric constant (γ= 0.066 kPa/°C)	[kPa K^{-1}]
r_a	= aerodynamic resistance	[day m^{-1}]

The saturation vapor pressure (e_s) and the inclination of the evaporation curve (s) are given by:

$$e_s(T_a) = 0.61 \exp\left(\frac{19.9 T_a}{273 + T_a}\right) \tag{H.2}$$

$$s = \frac{d e_s}{d T_a} = \frac{5430 e_s}{(273 + T_a)^2} \tag{H.3}$$

With:

T_a	= atmospheric temperature	[°C]

The actual vapor pressure can be calculated with:

$$e_a(T_a) = RH \cdot e_s(T_a) \tag{H.4}$$

With:

RH	= relative humidity	[-]

The aerodynamic resistance is:

$$r_a = \frac{245}{(0.54 u_2 + 0.5)} \cdot \frac{1}{86400} \tag{H.5}$$

With:

u_2 = wind speed at 2m height   [m/s]

The Earth's net radiation (R_N) can be calculated with the reflected long wave (R_B) and the reflected short wave (1-r)R_C.

$$R_N = (1 - r)R_C - R_B \tag{H.6}$$

The reflected short wave is $(1 - r)R_C$. R_C is calculated with an empirical relationship for the New Delhi case [52].

$$R_C = (0.21 + 0.48 \cdot n/N)R_A \tag{H.7}$$

With:

R_A = the short wave radiation expressed in evaporation intensity   [kgm^{-2}day^{-1}]
N = maximum amount of sun hours   [day^{-1}]
n = sunshine duration   [day^{-1}]

The R_A is given in table H.1 at 20°latitude of northern hemisphere.

Table H.1: R_A/λ in J day^{-1}m^{-2}, maximum amount of sun hours (N) and sunshine duration (n) per day per month

Lat 20°	Jan	Feb	Mar	Apr	May	Jun	Jul	Aug	Sept	Oct	Nov	Dec
R_A/λ	10.8	12.4	14.0	15.2	15.7	15.8	15.8	15.4	14.4	12.9	11.3	10.4
N	11.0	11.5	12.0	12.6	13.1	13.3	13.2	12.8	12.3	12.0	11.2	10.9
n	5.4	6.5	8.1	7.2	9.0	7.2	8.1	7.9	5.6	4.8	5.7	4.6

The net reflected long wave can be determined with the following empirical relation:

$$R_B = \sigma(273 + T_a)^4(0.47 - 0.21\sqrt{e_a})\left(0.2 + 0.8 \cdot \frac{n}{N}\right) \tag{H.8}$$

With:

σ = Stefan-Boltzmann constant ($\sigma = 4.9 \cdot 10^- 3$J day^{-1}m^{-2}K^{-4})   [J day^{-1}m^{-2}K^{-4}]

The evaporation can now be calculated, using formula H.1. Results are given in table H.2 for yearly average and each season.

Table H.2: Annually and seasonally averaged Pennman parameter results

Parameter	Annual	Dry	Rain	Nortes	Unit
T_a	27.737	27.806	29.202	26.222	°C
e_s	3.886	3.902	4.241	3.546	kPa
s	0.233	0.234	0.252	0.215	kPa°C
RH	70.8	67.8	70.8	72.4	%
e_a	2.749	2.647	3.004	2.567	kPa
u_s	5.001	5.519	4.878	4.877	m/s
r_a	8.860	8.148	9.048	9.049	$\cdot 10^{-7}$ day/mm
$R_C/(\lambda\rho)$	5.986	6.788	8.054	5.667	mm/day
$R_B/(\lambda\rho)$	1.161	1.351	1.286	1.375	mm/day
$R_N/(\lambda\rho)$	4.466	5.030	6.284	3.952	mm/day
E$_0$	**5.556**	**6.409**	**7.061**	**4.888**	**mm/day**

Tidal prism

The tidal prism is described as the wet volume in a basin between high water and low water. For a two-inlet tidal basin the tidal prism can be calculated by the following equations [68].

$$A_{b1} + A_{b2} = A_b \tag{I.1}$$

If the tidal range of the two inlets is constant the following equation may be used.

$$H_1 + H_2 = H \tag{I.2}$$

The following equation expresses the ratio between the areas of the basin split by the tidal watershed.

$$0 \leq \beta = \frac{A_{b1}}{A_b} \geq 1 \tag{I.3}$$

$$\alpha_{fe} = 0.41 - 0.24 \cdot 10^{-9} A_b \tag{I.4}$$

Finally the tidal prism can be calculated based on the results of all these results with the following formula.

$$P = \beta(1 - \alpha_{fe1} + 2.5 \cdot 10^{-9} \cdot \alpha_{fe1} \sqrt{\beta} \sqrt{A_b}) A_b \cdot H \tag{I.5}$$

$$P = (1 - \beta)(1 - \alpha_{fe1} + 2.5 \times 10^{-9} \cdot \alpha_{fe1} \sqrt{\beta} \sqrt{A_b}) A_b \cdot H \tag{I.6}$$

With:

A_b	= basin area	[m^2]
H	= tidal range	[m]
β	= ratio of basin area	[-]
α_{fe1}	= parameter for a basin	[-]
P	= tidal prism	[m^3]

J

Delft3D-FLOW results on fieldwork locations

In the figures below the salinity profile over depth of different measurement points is showed. The exact location of the different stations can be seen in figure F.2. On the y-axis is the depth shown as percentage. The x-axis shows the salinity in PSU. The red horizontal lines show the 20 % and 80 % depth. These lines are added, so the fieldwork measurements can be divided into similar depth percentages.
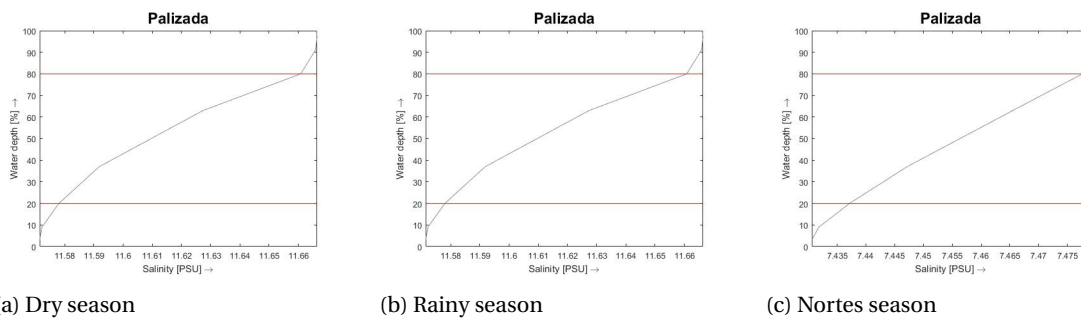

(a) Dry season   (b) Rainy season   (c) Nortes season

Figure J.1: Salinity profile of the entrance of the Palizada river over depth for different seasons

(a) Dry season   (b) Rainy season   (c) Nortes season
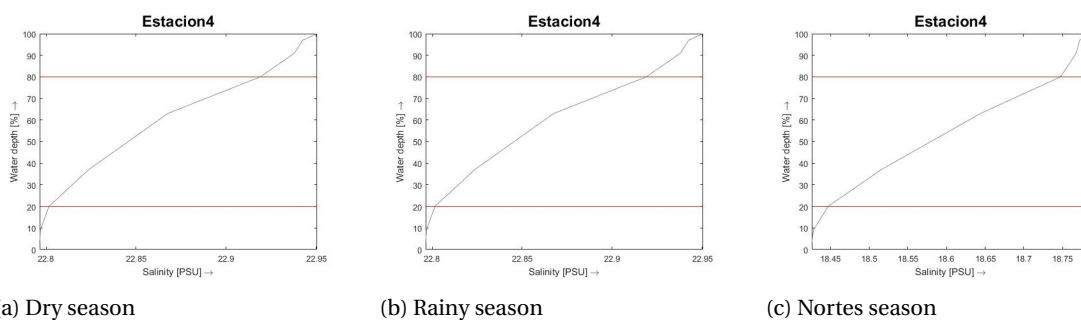
Figure J.2: Salinity profile over depth of Estacion 4 for different seasons

(a) Dry season   (b) Rainy season   (c) Nortes season
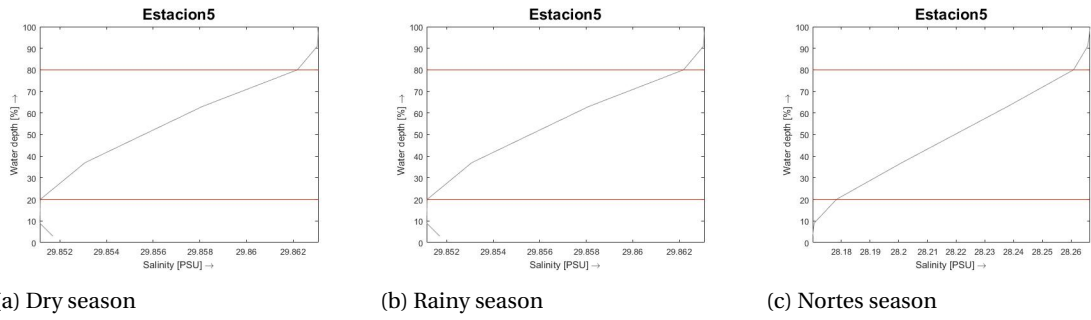
Figure J.3: Salinity profile over depth of Estacion 5 for different seasons

(a) Dry season   (b) Rainy season   (c) Nortes season
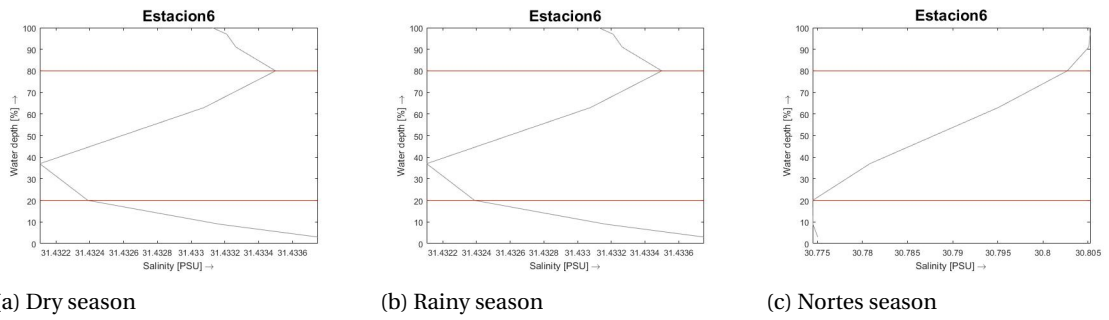
Figure J.4: Salinity profile over depth of Estacion 6 for different seasons

(a) Dry season   (b) Rainy season   (c) Nortes season
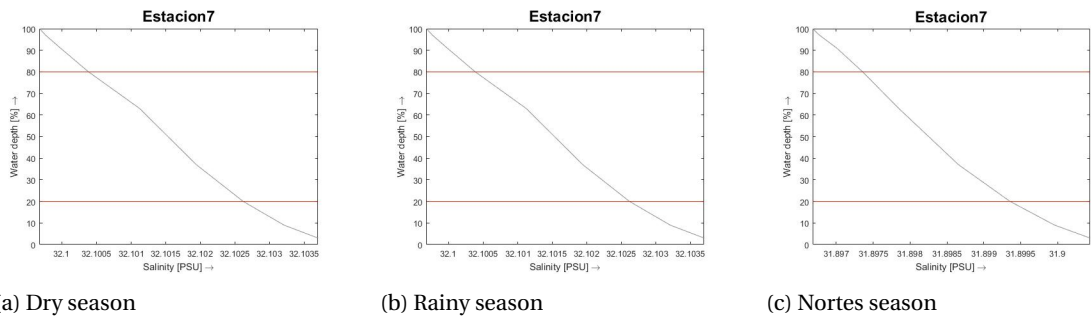
Figure J.5: Salinity profile over depth of Estacion 7 for different seasons

(a) Dry season   (b) Rainy season   (c) Nortes season
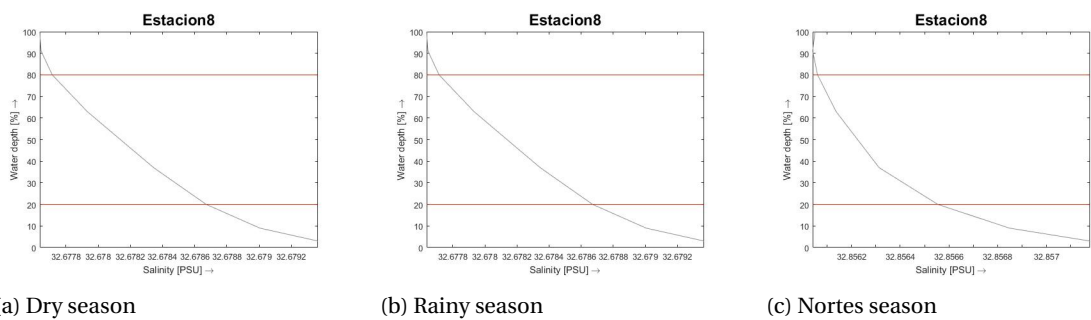
Figure J.6: Salinity profile over depth of Estacion 8 for different seasons

(a) Dry season

(b) Rainy season

(c) Nortes season

Figure J.7: Salinity profile over depth of Estacion 9 for different seasons

K

Conductivity ratio to salinity conversion
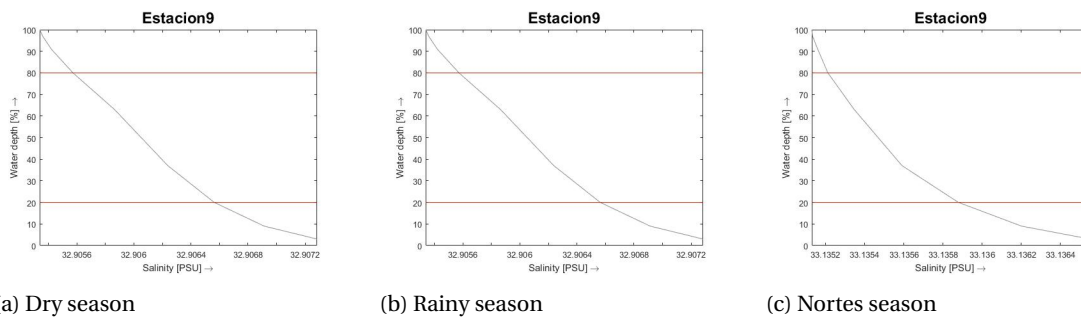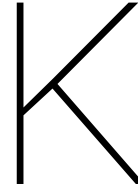
Measurements of conductivity and temperature are converted to practical salinity using the calculations in the paper of Foffenhof and Millard [24]. These calculations are elaborated below.

Table K.1: Constants of salinity conversion

	a	b	c	d	e	k
0	0.008	0.0005	0.6766097	3.426e-2	2.070e-5	0.0162
1	-0.1692	-0.0056	2.00564e-2	4.464e-4	-6.370e-10	
2	25.3851	-0.0066	1.104259e-4	4.215e-1	3.989e-15	
3	14.0941	-0.0375	-6.9698e-7	-3.107e-3		
4	-7.0261	0.0636	1.0031e-9			
5	2.7081	-0.0144				

Firstly, the conductivity data are transformed into the conductivity ratio, which is the ratio between the measured conductivity and the conductivity of standard seawater (S=35, t=15, p=0):

$$R = \frac{C(S, t, p)}{C(35, 15, 0)} \tag{K.1}$$

With:

R	= conductivity ratio	[-]
C	= conductivity	[μs cm^{-1}]
S	= salinity	[PSU]
t	= water temperature	[°C]
p	= atmospheric pressure	[decibar]

This ratio can be divided into three parts:

$$R = R_p \cdot R_t \cdot r_t \tag{K.2}$$

With:

$$R_p(S, t, p) = \frac{C(S, t, p)}{C(S, t, 0)} = 1 + \frac{p(e_1 + e_2 p + e_3 p^2)}{1 + d_1 t + d_2 t^2 + (d_3 + d_4 t)R} \tag{K.3}$$

$$R_t(S, t) = \frac{C(S, t, 0)}{C(35, t, 0)} \tag{K.4}$$

$$r_t(t) = \frac{C(35, t, 0)}{C(35, 15, 0)} = c_0 + c_1 t + c_2 t^2 + c_3 t^3 + c_4 t^4 \tag{K.5}$$

A standard atmospheric pressure at sea level is used which is defined as 101.325 decibar. Accordingly, the conductivity ratio R_t is derived using equation K.2:

$$R_t = \frac{R}{R_p \cdot r_t} \tag{K.6}$$

The last step in the calculation is calculating the practical salinity:

$$S = a_0 + a_1 R_t^{1/2} + a_2 R_t + a_3 R_t^{3/2} + a_4 R_t^2 + a_5 R_t^{5/2} + \Delta S \tag{K.7}$$

With:

$$\Delta S = \frac{t - 15}{1 + k(t - 15)} \cdot (b_0 + b_1 R_t^{1/2} + b_2 R_t + b_3 R_t^{3/2} + b_4 R_t^2 + b_5 R_t^{5/2}) \tag{K.8}$$

Flushing time

The flushing time is defined as the time needed for the water of the lagoon to be exchanged. Equation L.1 shows the expression of the flushing time.

$$T_\text{f} = \frac{V}{Q} \tag{L.1}$$

With:

T_f	= flushing time	[s]
V	= volume of the lagoon	[m^3]
Q	= volumetric flow rate through the system	[m^3/s]

Considering that the flushing time can be influenced by the tidal and river flow, the following formula can be distinguished [40]:

$$T_\text{f} = \frac{V}{(1 - b)Q_\text{T} + Q_\text{R}} \tag{L.2}$$

With:

T_f	= flushing time	[s]
V	= Volume in the lagoon	[m^3]
Q_T	= volume of the tidal flow	[m^3/s]
Q_R	= volume of the river flow	[m^3/s]
b	= fraction of water that returns at flood tide	[-]

The ratio b varies between 0 and 1, respectively the ratio where the entire tidal prism volume contributes to the water exchange and the ratio where the tidal flow does not renew the water in the lagoon. As this factor is unknown for the inlets of Terminos Lagoon, a sensitivity analyses is performed where factor b varies between 0 and 1. Furthermore, within this calculation different river flow rates are employed for the different seasons (dry, wet Nortes) and for the annual average. The assumption is made that the lagoon is well mixed, to ensure an equal resulting flushing time encompasses the whole lagoon.

The volume of the reservoir is determined using the average depth from the bathymetry, see section 2.4, where values above MSL are not taken into account. The area of the lagoon is determined at 1687 km^2, see appendix A, and the corresponding average depth is 2.572 m. This gives a volume of:

$$V = 1687 \cdot 10^6 \cdot 2.572 = 4339 \cdot 10^6 \, m^3 \tag{L.3}$$

The discharge of the rivers is calculated in section 4.1.4, see table 4.4. The flow of the tidal discharge can be calculated using the time between ebb and flood and the volume of water flowing trough the inlets. The tidal period is determined at 24 hours and 35 min, see 6.2. The tidal prism of both the Puerto Real and Carmen inlet

is 534.9 million m^3, see chapter 4.2.2. The total contribution of the tidal flow can be calculated by multiplying the tidal prism with the tidal period.

Finally, the flushing time can be calculated, using the values mentioned above.

M
Tidal constituents

M.1. Matlab toolbox for tidal constituents

To obtain the tidal constituents, the Matlab toolbox for tidal consituents is used. The toolbox detrends the data. After that it uses the least squares method to fit tidal components to the data. This toolbox makes a distinction between 38 different tidal constituents. The amplitude of some of the tidal constituents is so small they return NAN values. These tidal constituents are not taken into account and removed from the figures.

Besides calculating the tidal constituents and plotting the measured values, it is also possible to make a prediction about the tidal signal in the past and of the future, based on the calculated tidal constituents.

M.2. Tidal constituents by Fast Fourier Transformation

The Fast Fourier Transformation is a method to distinguish different frequency components. The components are sinusoidal oscillations with different amplitudes and phases. In the graphs, the height of the peak shows the importance of the frequency. The most important tidal constituents are showed in table 4.5.
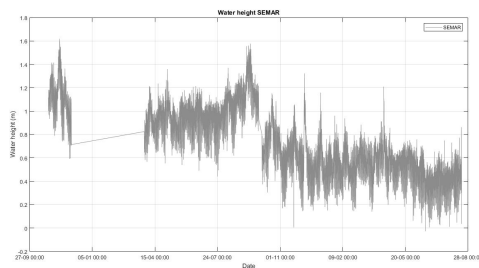
(a) Water height measurements SEMAR
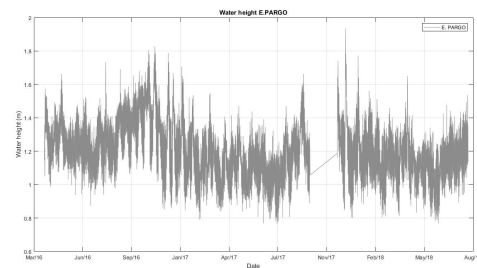
(b) Water height measurements E.Pargo

Figure M.1: Water height measurements of both locations

name	speed	period	amp	phase
'O1'	13.9430	1.0758	0.0986	-2.7493
'K1'	15.0411	0.9973	0.0949	0.9466
'M2'	28.9841	0.5175	0.0726	1.0055
'P1'	14.9589	1.0027	0.0326	0.9241
'Q1'	13.3987	1.1195	0.0224	2.2616
'N2'	28.4397	0.5274	0.0185	-0.4171
'S1'	15	1	0.0176	1.0903
'MSF'	1.0159	14.7653	0.0130	-2.7855
'S2'	30	0.5000	0.0080	-2.9508
'MM'	0.5444	27.5546	0.0074	-0.2633
'MF'	1.0980	13.6608	0.0073	-1.1373
'J1'	15.5854	0.9624	0.0054	2.4409
'M4'	57.9682	0.2588	0.0050	1.5702
'OO1'	16.1391	0.9294	0.0049	1.8376
'MK3'	44.0252	0.3407	0.0042	-0.6848
'2N2'	27.8954	0.5377	0.0040	-2.0245
'RHO'	13.4715	1.1135	0.0037	0.0256
'MU2'	27.9682	0.5363	0.0033	2.6184
'R2'	30.0411	0.4993	0.0031	2.8078
'K2'	30.0821	0.4986	0.0029	2.7224
'S4'	60	0.2500	0.0028	2.3788
'LAM2'	29.4556	0.5092	0.0023	0.6903
'2SM2'	31.0159	0.4836	0.0023	0.1132
'MN4'	57.4238	0.2612	0.0023	0.0727
'NU2'	28.5126	0.5261	0.0021	-1.3297
'L2'	29.5285	0.5080	0.0020	-1.3489
'M1'	14.4967	1.0347	0.0018	-1.9572
'2MK3'	42.9271	0.3494	0.0017	2.0851
'T2'	29.9589	0.5007	0.0016	3.0725
'MS4'	58.9841	0.2543	0.0015	0.5752
'2Q1'	12.8543	1.1669	0.0014	2.9716
'M6'	86.9523	0.1725	6.7037e-04	-0.0418
'M8'	115.9364	0.1294	5.5618e-04	-2.0914
'M3'	43.4762	0.3450	5.4939e-04	-2.3812

Figure M.2: Tidal constituents SEMAR by toolbox

name	speed	period	amp	phase
'K1'	15.0411	0.9973	0.0841	1.4167
'O1'	13.9430	1.0758	0.0834	-2.2190
'S1'	15	1	0.0399	1.5772
'M2'	28.9841	0.5175	0.0380	1.8806
'P1'	14.9589	1.0027	0.0335	1.5745
'SSA'	0.0821	182.6211	0.0292	-3.0222
'Q1'	13.3987	1.1195	0.0174	2.7159
'MM'	0.5444	27.5546	0.0168	1.0698
'MSF'	1.0159	14.7653	0.0150	3.1329
'MF'	1.0980	13.6608	0.0110	0.2475
'N2'	28.4397	0.5274	0.0109	0.5090
'S2'	30	0.5000	0.0109	1.3494
'K2'	30.0821	0.4986	0.0062	2.9600
'OO1'	16.1391	0.9294	0.0052	1.8868
'M4'	57.9682	0.2588	0.0044	2.0589
'M1'	14.4967	1.0347	0.0036	2.1089
'L2'	29.5285	0.5080	0.0031	0.5093
'RHO'	13.4715	1.1135	0.0031	1.5160
'J1'	15.5854	0.9624	0.0028	2.8120
'MN4'	57.4238	0.2612	0.0027	0.6252
'R2'	30.0411	0.4993	0.0022	2.5245
'NU2'	28.5126	0.5261	0.0022	-0.5454
'MK3'	44.0252	0.3407	0.0019	0.2677
'S4'	60	0.2500	0.0019	3.0878
'MU2'	27.9682	0.5363	0.0017	2.9819
'MS4'	58.9841	0.2543	0.0016	-0.2363
'2Q1'	12.8543	1.1669	0.0014	2.1916
'T2'	29.9589	0.5007	9.3969e-04	2.2861
'M3'	43.4762	0.3450	9.2078e-04	-0.0562
'2N2'	27.8954	0.5377	8.5061e-04	1.9477
'LAM2'	29.4556	0.5092	5.6582e-04	0.6962
'M6'	86.9523	0.1725	4.9617e-04	1.7339
'2SM2'	31.0159	0.4836	4.7802e-04	1.5123
'2MK3'	42.9271	0.3494	4.6156e-04	-1.9934
'S6'	90	0.1667	4.1081e-04	0.6047

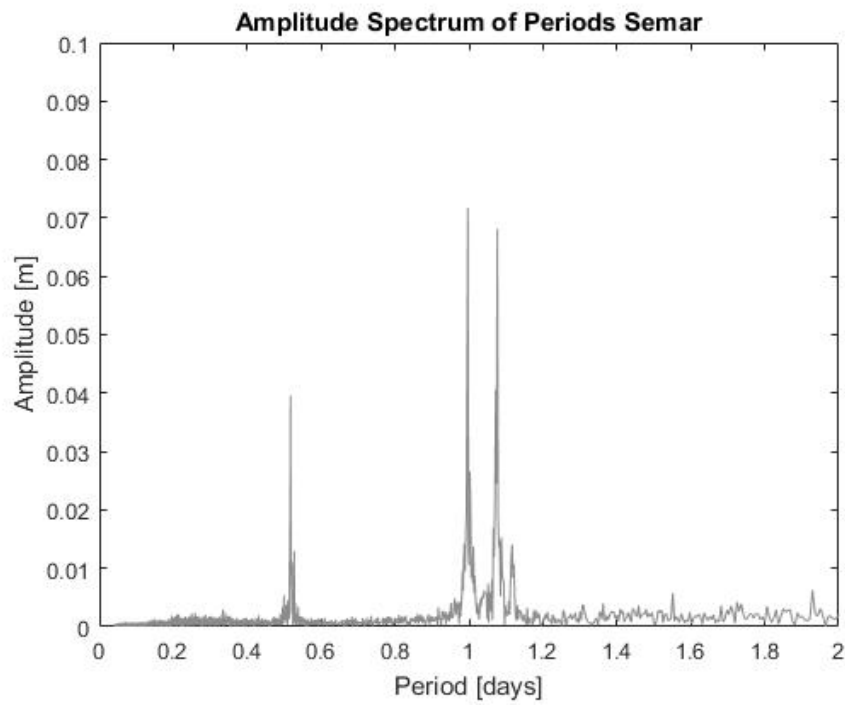Figure M.3: Tidal constituents E.Pargo by toolbox
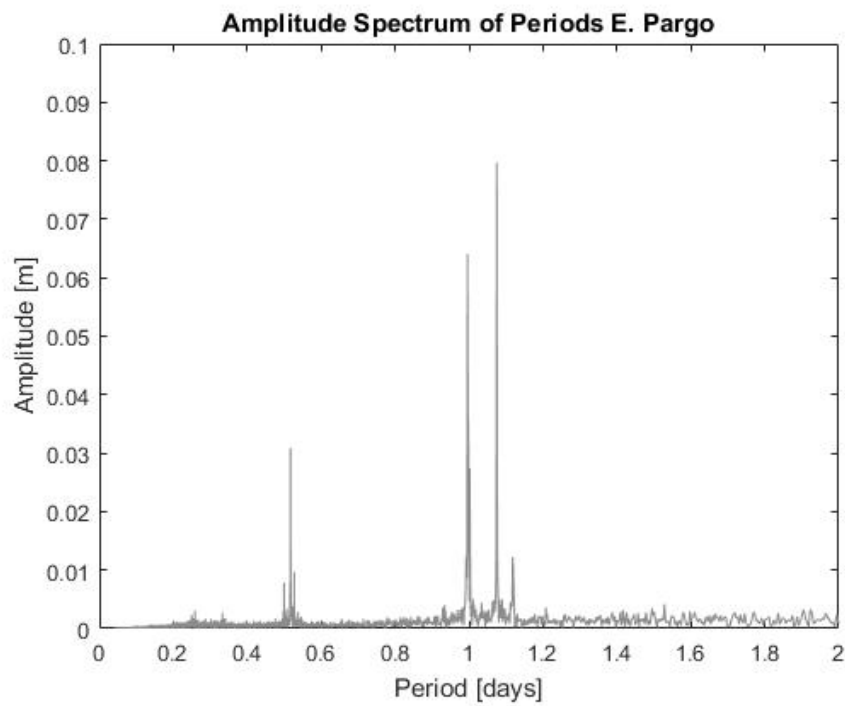
Figure M.4: Tidal constituents SEMAR FFT

Figure M.5: Tidal constituents E.Pargo FFT

Semi-correlations

In section 4.4.3 the correlation between water temperature and atmospheric temperature is investigated by the application of semi-correlations. For this purpose the data is transformed to standard normal and plotted in figure N.1. Accordingly the bivariate distribution is compared to the Gaussian-, Gumbel-, Clayton-, Frank- and T-copula to find out which copula describes the pairs of variables the best. These copulas are shown in figures N.2 to N.6 and are based on the correlation between the water temperature and atmospheric temperature of the empirical data. The amount of samples of the fitted copulas are equal to the amount of data points of the empirical copula.
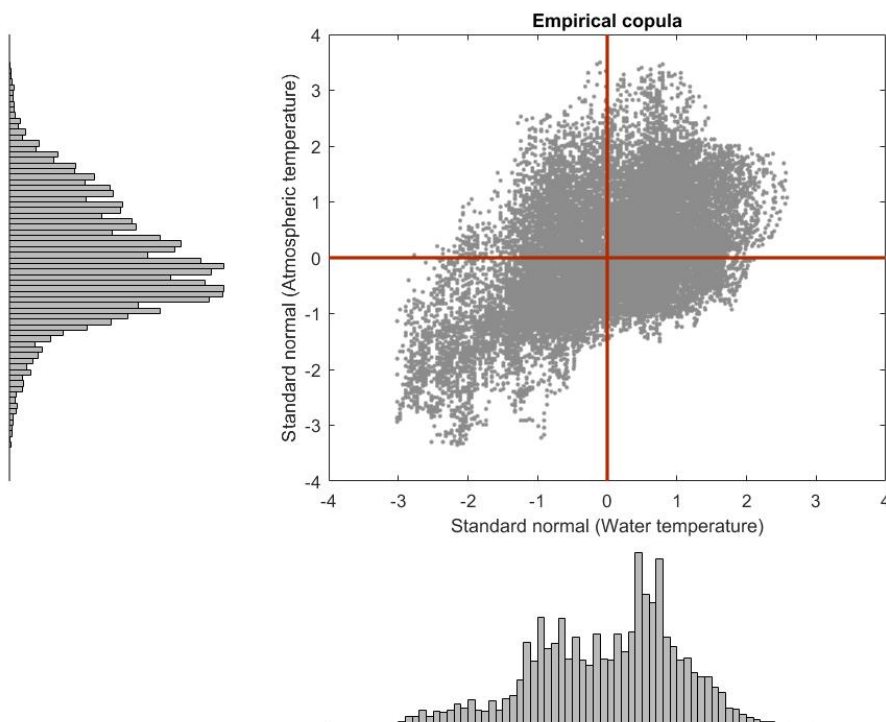
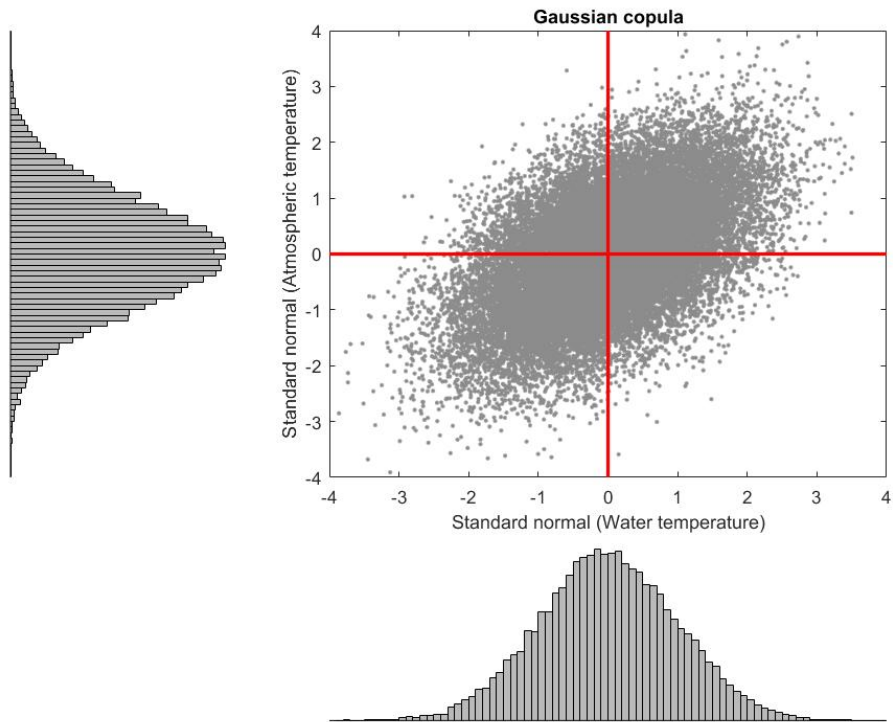Figure N.1: Empirical copula transformed to standard normal

Figure N.2: Samples of Gaussian copula transformed to standard normal
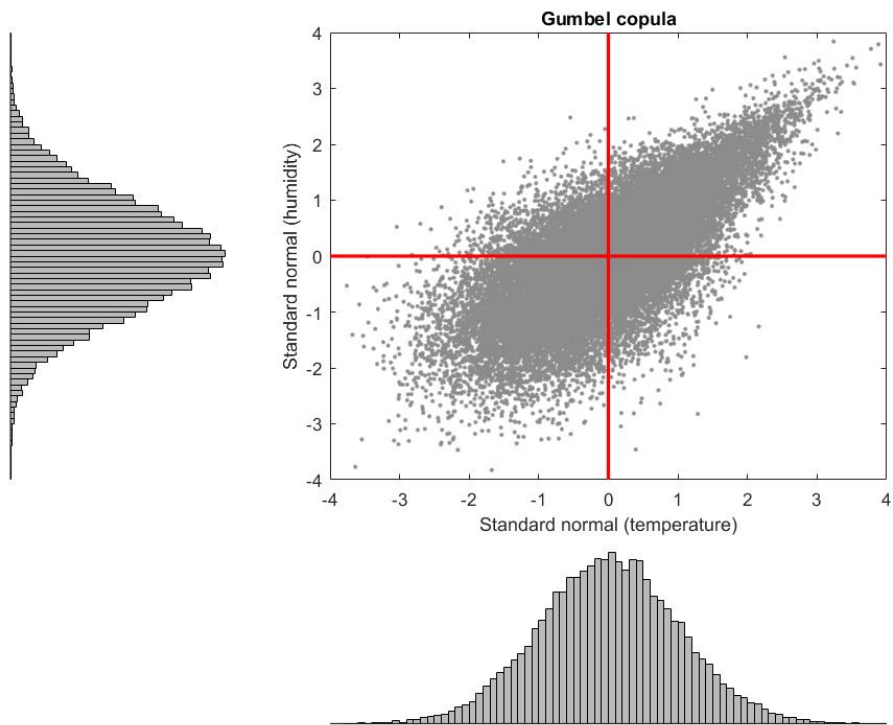

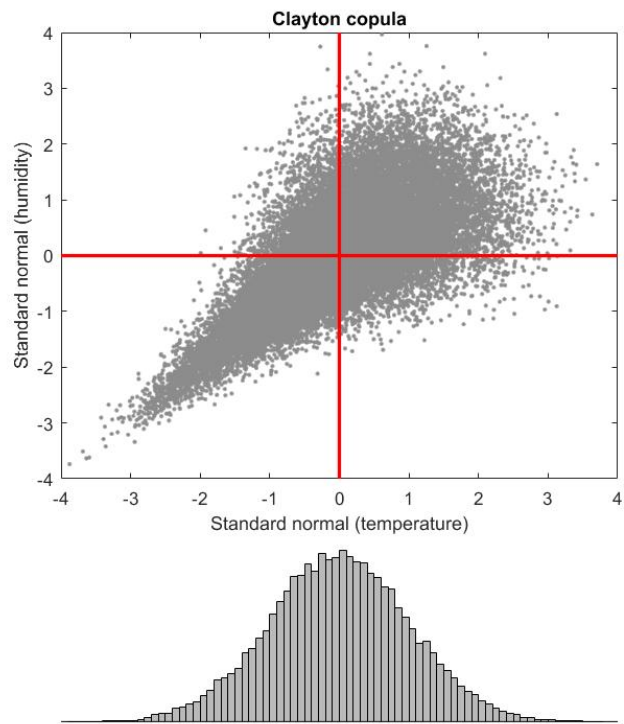Figure N.3: Samples of Gumbel copula transformed to standard normal

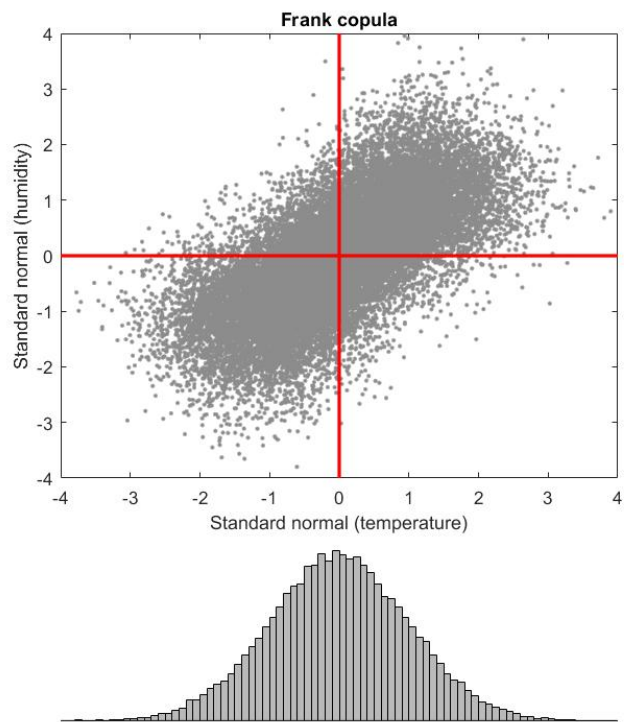Figure N.4: Samples of Clayton copula transformed to standard normal

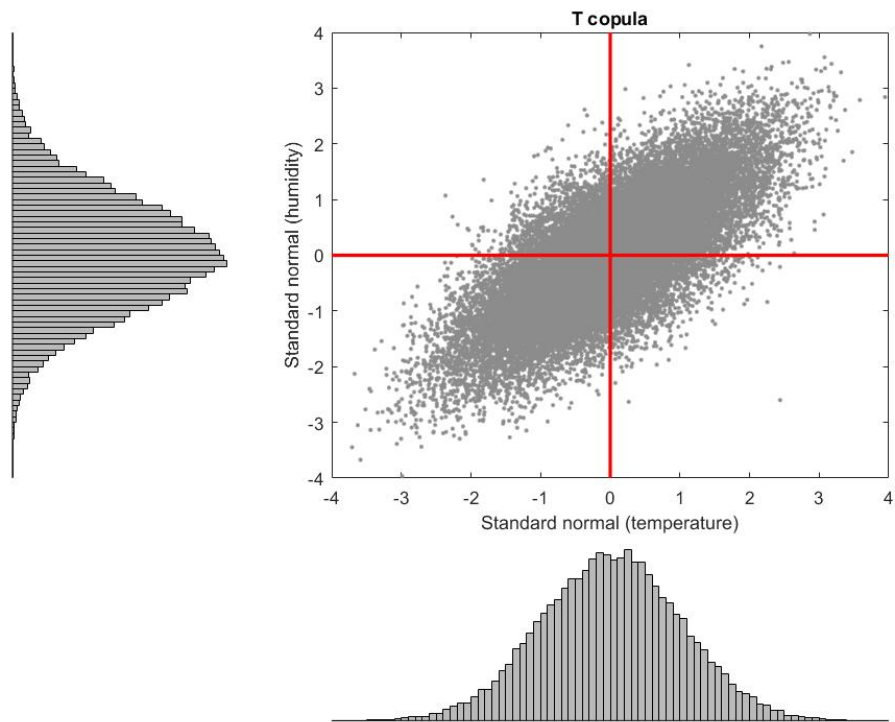Figure N.5: Samples of Frank copula transformed to standard normal

Figure N.6: Samples of T copula transformed to standard normal

In each quadrant the correlation is calculated in order to compare the goodness of fit of the copulas with respect to the empirical copula. These results are given in table 4.13 in section 4.4.3.